ABSTRACT

STOUTE, NICHOLAS AARON. Properties of Closed-Shell Titanium Silicate and Gallium-Containing Semiconductor Systems. (Under the direction of Dr. David Aspnes.)

We demonstrate that an atomic-scale approach may be appropriate for the analysis of the compositional and bonding properties of titanium silicate alloys and shallow d-core level reflectance spectra of gallium-compound semiconductors.

Ti silicate analysis was conducted using X-Ray Absorption Spectroscopy (XAS), X-Ray Photoemission Spectroscopy (XPS), and Spectroscopic Ellipsometry (SE) data taken on a range of Ti-silicate alloys. XAS data were obtained by the Lucovsky group at Stanford Synchrotron Radiation Laboratories (SSRL) at the Stanford Linear Accelerator Center (SLAC), and were used as the primary source of information. To bolster conclusions we solicited XPS data from the Opila Laboratory at the University of Delaware, which were provided by Les Fleming. We also took SE data on Ti silicate alloys annealed at different temperatures using two ellipsometers, one of which was built by the author specifically to probe energies in the vacuum uv range. Reflectance data from 20 to 25 eV, which contain spectral features due to transitions from Ga3d core levels, were obtained on GaP, GaAs, GaSb, GaSe, and GaP_xAs_{1-x} at the storage ring Tantalus 1 at the Stoughton Synchrotron Radiation Center by Aspnes and co-workers from about 1980 to 1982.

Ti $L_{2,3}$ XAS data were fitted with reference spectra to obtain 4-fold coordination concentrations (in differing symmetries) and 6-fold coordination concentrations with respect to alloy composition and annealing. Analyzing the

concentrations allowed us to draw conclusions on coordination with respect to alloy composition and annealing. We were able to model the 4-fold “in solution” to 6-fold phase-segregated conversion as a stochastic process, and we found a complete conversion to 6-fold phase-segregated TiO_2 through annealing with at least 36% Ti and above. We attributed this phase segregation to a striation effect previously reported in the literature. XAS OK_1 spectra corroborate these results. Investigation of the XPS Ti $L_{2,3}$ data verified the formal Ti valence in the Ti silicate alloys as +4. Through atomic-multiplet calculations, we show that because of Coulombic and spin orbit effects the final states of the Ti $L_{2,3}$ spectra do not maintain any significant degeneracy, even in the absence of a crystal field. Dielectric functions from 1.5 to 9.0 eV, extracted from the SE data obtained on annealed Ti silicate alloys, verified that significant coordination change occurred between the annealing temperature of 500 and 700 ºC.

A local atomic multiplet theory was applied to investigate the Ga3d shallow core-level spectra of GaP, GaAs, GaSb, GaSe, and $GaAs_{1-x}P_x$. This is a novel application of an existing theory that is typically used for higher-energy transitions. We modeled these spectra quantitatively as a Ga^{+3} closed-shell ion affected by perturbations on 3d hole-4p electron final states, specifically spin-orbit effects on the hole and electron, and a crystal-field effect on the hole. The crystal-field perturbation arises from the surrounding bond charges and positive ligand anions. Radial-strength parameters were obtained through a least-squares process, and general trends identified with respect to anion electronegativity. Primary conclusion

drawn is that the crystal-field effect, in addition to the spin-orbit interaction, plays a significant role in breaking d-level degeneracy, and consequently is necessary to understand shallow 3d core level spectra.

Properties of Closed-Shell Titanium Silicate and Gallium-Containing Semiconductor Systems

by
Nicholas Aaron Stoute

A dissertation submitted to the Graduate Faculty of
North Carolina State University
in partial fulfillment of the
requirements for the degree of
Doctor of Philosophy

Physics

Raleigh, North Carolina

2011

APPROVED BY:

David E. Aspnes Committee Chair	Hans Hallen
Gerald Lucovsky	Jerry L. Whitten

DEDICATION

Dedicated to my family

BIOGRAPHY

Nicholas Aaron Stoute was born at Camp Lejeune, North Carolina, on May 15, 1979 to Mickey J. Stoute and Kathy A. Ellison Stoute. He has one sister, Michelle R. Stoute. He spent his childhood growing up in a Marine family, living in North Carolina until middle school and subsequently moving to Allentown, Pennsylvania, where he played football and learned to deal with the unfamiliar cold weather for a couple of years. After next spending some time in Guantanamo Bay, Cuba, which has always been an interesting conversation starter, he and his family eventually moved back to his home state of North Carolina where he graduated high school from The North Carolina School of Science and Math in Durham, North Carolina in 1997. Attending North Carolina State University, next door in Raleigh, he subsequently earned Bachelor's Degrees in both Mathematics and Physics in 2001, a Master's Degree in Physics in 2004, and then completed the requirements for the Doctor of Philosophy Degree in Physics at North Carolina State University in the Fall of 2011 under the direction of Dr. David Aspnes.

ACKNOWLEDGMENTS

I singularly and gratefully acknowledge and sincerely thank Dr. David Aspnes for whom it has been a true privilege and honor for me to have the experience of a lifetime under his guidance and direction. No graduate student could have asked for a more understanding and brilliant advisor. I would also like to take the opportunity to thank my committee members Dr. Hans Hallen, Dr. Gerald Lucovsky, and Dr. Jerry Whitten for their assistance and consideration. It's been a pleasure to work with all the members of Dr. Aspnes' and Dr. Lucovsky's Groups, past and present, as well as the numerous colleagues I've had the pleasure to meet and work alongside. I would like to thank, specifically, Jih-Fu, Eric, Muharrem, Jon, Kenan, Bilal and his wife Emine, Bill, J.P., Les, Mark, Dr. Rowe, Dr. Dietz, Vincent, Haijiang, Hyungtak, In Kyo, Xiang, Sungjin, Klaus, Dave, Jinwoo, and Judith. I would like to thank my Mom, Dad, and Sister, as well as the rest of my extended family, for all their continued love and support. I would like to thank Ryan, and his wife and my best friend, Rachel for how much they've been there for me. It's a pleasure to know them and a joy to see their kids, Rebekah, Leah, Benjamin and Eli grow up. I would like to thank the rest of their family, Amanda, David, Barbara, Eric, Linda, Barry, Mandi, her husband Adam, and all their cousins and distant relations for making me feel at home. I would like to thank Thomas and Doug for all the Bojangles dinners, Jessica for the late night studying at the library and help on outlining, John for the appropriate levels of drinking and pool there at the end and Alton for all the sighing.

TABLE OF CONTENTS

LIST OF TABLES viii

LIST OF FIGURES ix

CHAPTER 1 INTRODUCTION 1

1.1 Summary of purpose, results, and conclusions 1

1.2 Motivation 2

1.3 Detailed results and conclusions 5

1.3a Spectroscopic Ellipsometer 5

1.3b Local Ti coordination 6

1.3c Shallow-d-core-level spectra in Ga-containing Semiconductors 7

1.4 Why Ti silicates: Importance and summary of previous work 8

1.5 Theoretical Overview 17

1.6 Experimental Overview 18

1.7 Thesis Overview 20

1.8 References 20

CHAPTER 2 THEORY 22

2.1 Argument for atomic-like calculations 22

2.2 Calculation of atomic muliplet effects for closed shell initial states to electron-hole final states 24

2.3 Differences in Final State Configurations: Effects on XAS and XPS 33

2.4 Typical coordination structures of titanium silicate alloys 33

2.5 Modeling of Coordination-complex Modifications as a Stochastic Process.... 35
2.6 References..... 35
CHAPTER 3 EXPERIMENTAL METHODS 36
3.1 Thin film preparation by remote-plasma-enhanced metal-organic chemical vapor deposition (RPE-MOCVD) and thermal annealing 36
3.2 X-Ray Absorption Spectroscopy (XAS)..... 36
3.3 X-Ray Photoemission Spectroscopy (XPS) 38
3.4 VIS-VUV Spectroscopic Ellipsometry (SE)..... 39
3.5 Ga3d Core-level Reflectance Data 43
3.6 References..... 44
CHAPTER 4 TITANIUM SILICATE ALLOYS 45
4.1 XPS Ti $L_{2,3}$, Si $L_{2,3}$, O K_1 Data Presentation 45
4.2 XPS Ti $L_{2,3}$, Si $L_{2,3}$, O K_1 Discussion..... 47
4.3 XAS Ti $L_{2,3}$ (0-100% TiO_2) data..... 51
4.4 XAS O K_1 (0-100% TiO_2) data 54
4.5 XAS Ti $L_{2,3}$ (2-14% TiO_2) data..... 55
4.6 XAS O K_1 (2-14% TiO_2) data 55
4.7 Comments..... 56
4.8 XAS Ti L_3 spectra: discussion 58
4.9 Compositional Analysis of XAS Spectra 60
4.10 Coordination Structures from XAS Spectra..... 63
4.11 Nearest-neighbor Effects on Ti Coordination 65

4.12 Correlation of annealing-induced conversion of Ti coordination from 4- to 6-fold with the stochastic model 66
4.13 Phase Segregation and Striation in medium- to high-Ti-percentage Alloys ... 67
4.14 Lineshape changes in XAS Ti $L_{2,3}$ spectra of low-percentage TiO_2 alloys with annealing 71
4.15 Verification of annealing-induced distortions of 4-fold Ti coordinations..... 73
4.16 XAS Ti $L_{2,3}$ multiplet calculations 75
4.17 Analysis of XAS O K_1 Spectra..... 82
4.18 SE data and comments..... 84
4.19 References..... 88
CHAPTER 5 SHALLOW Ga3d CORE-LEVEL TRANSITIONS..... 89
5.1 Calculation Introduction 89
5.2 General Effects of the Individual Terms in the Hamiltonian 94
5.3 Removing the contributions of the GaP and GaAs centers in $GaAs_{1-x}P_x$ alloys..... 97
5.4 Results..... 101
5.5 Discussion..... 104
5.6 References..... 110
CHAPTER 6 SUMMARY AND FUTURE WORK 111
6.1 Summary..... 111
6.2 Future Work 113

LIST OF TABLES

Table 4.1 Ti $L_{2,3}$ XPS Binding Energies 47

Table 4.2 Si $L_{2,3}$ XPS Binding Energies 49

Table 4.3 O K_1 edge XPS Binding Energies 50

Table 4.4 Coordination Fractions for As-deposited and Annealed 0-100% Compositions 63

Table 4.5 3-Phase Extracted Overlayer Thickness (Bench 1.5 - 6 eV) 85

Table 4.6 3-Phase Extracted Overlayer Thickness (VUV 4 - 9 eV) 85

Table 5.1 Ga Compound Fitting Summary Part 1 103

Table 5.2 Ga Compound Fitting Summary Part 2 104

LIST OF FIGURES

Figure 1.1 Effect of TiO_2 content on selected physical properties of unannealed TiO_2-SiO_2 glasses. (from Shultz 1972) 11

Figure 1.2 Compositions/Descriptions of binary TiO_2-SiO_2 glasses (from Schultz 1976)..... 12

Figure 1.3 Electron micrographs of 13.8 wt% TiO_2 A) unannealed and B) annealed at 960˚C for 1 hour 12

Figure 1.4 Transmission electron micrographs of ion-thinned 13.8 wt% TiO_2 annealed at 960˚C for 1 hour. A) Bright-field image and B) and C) dark-field images at different angles 13

Figure 1.5 Table of EXAFS results for Ti in SiO_2 glasses (from Sandstrom 1980)..... 14

Figure 1.6 Summary of estimates of Ti coordination fraction versus composition (from Greggor 1983) 14

Figure 2.1 Rutile unit cell 34

Figure 2.2 Anatase unit cell 34

Figure 3.1 VUV Spectroscopic Ellipsometer Schematic..... 39

Figure 4.1 Ti $L_{2,3}$ XPS 45

Figure 4.2 Si $L_{2,3}$ XPS 46

Figure 4.3 O K_1 edge XPS 46

Figure 4.4 Ti $2p_{3/2}$ Binding Energy versus x 47

Figure 4.5 Si $L_{2,3}$ Binding Energy versus x 48

Figure 4.6 Comparison of Ti $2p_{3/2}$ binding energy with average binding energy of the $SiL_{2,3}$ states 50

Figure 4.7 Ti $L_{2,3}$ XAS (0-100% TiO_2) as deposited 51

Figure 4.8 Ti $L_{2,3}$ XAS (0-100% TiO_2) annealed 51

Figure 4.9 Ti $L_{2,3}$ spectrum of a TiO_2 as-deposited thin film with 6-fold coordinated Ti sites 52

Figure 4.10 XAS Ti L_3 spectra 4.2% to 100% TiO_2 53

Figure 4.11 OK_1 XAS spectra for the as-deposited samples 54

Figure 4.12 OK_1 XAS spectra for the annealed samples 54

Figure 4.13 XAS Ti $L_{2,3}$ 2%-14% Ti (as-deposited and annealed 900˚C) 55

Figure 4.14 OK_1 as-deposited XAS 2-14% TiO_2 55

Figure 4.15 OK_1 Annealed XAS 2-14% TiO_2 56

Figure 4.16 Ti $L_{2,3}$ edge spectra for 6-fold, 5-fold, and 4-fold materials (Hoche 2005) 56

Figure 4.17 Ti $L_{2,3}$ edge spectra for 6-fold, 5-fold, and 4-fold materials (Henderson 2002) 57

Figure 4.18 ELNES Ti $L_{2,3}$ spectra on isoelectronic 4-fold coordinated closed-shell first row transition metal systems. (from Brydson 1993) 57

Figure 4.19 -2^{nd} derivative spectra XAS $TiL_{2,3}$ highlighting prominent 4-fold and 6-fold feature 58

Figure 4.20 (-2^{nd} derivative) Ti $L_{2,3}$ data at low concentrations of TiO_2 60

Figure 4.21 EELS spectra of $TiCl_4$ $CpTiCl_3$ and Cp_2TiCl_2 60

Figure 4.22 Titanium $L_{2,3}$-edge XANES specta of rutile, anatase used for reference as well as amporhpous TiO2 and titania aerogel 61

Figure 4.23 TiO_2 Reference spectra for fitting 61

Figure 4.24 Coordination fraction versus fraction TiO_2 64

Figure 4.25 Comparison between 6-fold Extraction and Stochastic Model 65

Figure 4.26 Ti $L_{2,3}$ As-deposited and annealed 36% to 100% TiO_2 68

Figure 4.27 Comparison between as-deposited 23.6% and 36% TiO_2 68

Figure 4.28 OK_1 As-deposited and annealed 23.6% to 100% TiO_2 69

Figure 4.29 TiO_2-SiO_2 striations (Hodroj 2008) 70

Figure 4.30 Aligned comparisons of Ti $L_{2,3}$ spectra taken on annealed and as-deposited 4.2%, 4.8%, and 5.1% Ti silicate alloys 71

Figure 4.31 Comparison of 4-fold and 6-fold reference amplitudes 74

Figure 4.32 Comparison of 6-fold fraction in as-dep and annealed 75

Figure 4.33 Ti^{4+} spherically symmetry, full 2p 3d splitting, Slater integral 60% of normal 77

Figure 4.34 Ti^{4+} octahedral symmetry with a crystal field splitting of 1.8 eV, full 2p3d splitting, Slater integral 60% of normal 77

Figure 4.35 Ti^{4+} Oh symmetry with a crystal field splitting of -1.8 eV full 2p 3d splitting, Slater integral 60% of normal 78

Figure 4.36 Crystal Field Calculations 78

Figure 4.37 Multiplet calculations for Ti $L_{2,3}$ XAS spectra 79

Figure 4.38 XAS $TiL_{2,3}$ spectrum of $SrTiO_3$ 79
Figure 4.39 Ti Formal Valence Comparison 80
Figure 4.40 ELENS of 4-fold coordinated compounds 80
Figure 4.41 Multiplet spectra calculated with a crystal field potential 81
Figure 4.42 Staggered multiplet calculations for crystal-field potentials from -0.5 to -1.5eV 81
Figure 4.43 Numerically calculated second derivatives of the OK_1 edge XAS data 82
Figure 4.44 -2^{nd} derivatives of the OK_1 edge XAS data 83
Figure 4.45 ε_1 and ε_2 for bulk anatase and rutile (from Jellison 2003)..... 84
Figure 4.46 SE spectra for the 6%, 11%,16%, and 24% samples as-deposited and annealed at 500 °C 700 °C and 900 °C..... 86
Figure 4.47 SE spectra for the samples as-deposited and annealed at 900 °C 87
Figure 5.1 2EDR spectra for several $GaAs_{1-x}P_x$ alloys 89
Figure 5.2 Dependences on electron spin-orbit splitting with crystal field splitting..... 95
Figure 5.3 Hole Spin Orbit Splitting Series (Crystal Field Splitting)..... 96
Figure 5.4 Crystal Field Splitting Series 96
Figure 5.5 Statistical weighting for the different $GaAs_{1-x}P_x$ alloy centers 97
Figure 5.6 Normalized GaAs second-derivative reflectance spectrum..... 99
Figure 5.7 Normalized $GaAs_{.90}P_{.10}$ second-derivative reflectance Spectrum 99
Figure 5.8 Normalized $GaAs_{.80}P_{.20}$ second-derivative reflectance spectrum..... 99

Figure 5.9 Normalized $GaAs_{.71}P_{.29}$ second-derivative reflectance spectrum 99

Figure 5.10 Normalized $GaAs_{.60}P_{.40}$ second-derivative reflectance spectrum.... 100

Figure 5.11 Normalized $GaAs_{.51}P_{.49}$ second-derivative reflectance spectrum.... 100

Figure 5.12 Normalized GaP second-derivative reflectance spectrum 100

Figure 5.13 $GaAs_{1-x}P_x$ spectra after the GaP and GaAs contributions removed . 101

Figure 5.14 GaP fitting 102

Figure 5.15 $GaAs_{.51}P_{.49}$ fitting 102

Figure 5.16 $GaAs_{.60}P_{.40}$ fitting 102

Figure 5.17 $GaAs_{.71}P_{.29}$ fitting 102

Figure 5.18 $GaAs_{.80}P_{.20}$ fitting 102

Figure 5.19 $GaAs_{.90}P_{.10}$ fitting 102

Figure 5.20 GaAs fitting 103

Figure 5.21 GaSe fitting 103

Figure 5.22 GaSb fitting 103

Figure 5.23 GaP GaAs GaSe GaSb comparison 105

Figure 5.24 $GaAs_{x-1}P_x$ alloy series comparison 106

1. INTRODUCTION

1.1 Summary of purpose, results, and conclusions

While this thesis may seem to be relatively broad, the focus is consistently on understanding some properties of semiconductor material systems through a local approach centered about ligand effects on the cation. In addition, we do ellipsometric studies on one set of the material systems to confirm and further elucidate conclusions drawn from analysis of spectra involving deep core-level transitions. Overall, we summarize the purpose of this study as primarily threefold. First, we investigate XAS and XPS spectroscopic data of the Ti silicate system and perform crystal-field calculations to develop an understanding of spectroscopic progressions. In particular, our goal is to establish Ti valence and coordination types, their concentrations in Ti silicates, and how these concentrations depend on Ti composition. We do this by analyzing XPS data and fitting model reference data sets to Ti $L_{2,3}$ XAS spectra, using theoretical calculations to estimate locations and strengths of structure in these data. To provide additional substantiation, we take advantage of literature data obtained on Ti-containing molecules for which the configurations are known in detail.

Second, we study the vacuum-UV dielectric response of these materials as well as others outside of the thesis. To do this I constructed and operated a spectroscopic ellipsometer (SE) that covered the spectral range 4 to 9 eV. This range is more appropriate for studying wide-bandgap materials than usual configurations, which are restricted to the quartz-optics range below 6 eV. Using

this system I determine dielectric functions of a set of Ti silicate films and analyze changes in spectroscopic signatures with annealing temperatures between 500 and 700º C. These data are particularly sensitive to phase segregation.

Third, we determine whether this approach can also be used to understand reflectance spectra of shallow core-level transitions, specifically those involving the 3d core levels of Ga-containing semiconductors. This is an interesting intermediate test case for multiplet theory, because the Ga3d core levels are not deep enough to be essentially independent of their local environment, yet are too localized to be treated by band theory. As a result of this work we find that the local atomic-like calculations appear to model reasonably well the spectral features associated with transitions orlginating with these shallow Ga3d core levels. One interesting result is that the splitting that we see for the 3d levels is found to be due not only to the spin-orbit effect but is also influenced significantly by crystal-field effects on said 3d levels due to charges associated with the adjacent anions.

1.2 Motivation

Titanium silicates are important materials that are used for a wide variety of purposes. To identify spectroscopically and understand theoretically the various coordination states of Ti in these alloys requires knowledge of the crystal structure, the chemical bonding geometry, and the electronic configurations of these materials, and how X-Ray Absorption Spectroscopy (XAS), X-Ray Photoemission Spectroscopy (XPS), and Spectroscopic Ellipsometry (SE) can provide different insights. It is particularly important to understand how these physical properties

directly affect the coordination of the Ti site over extended composition and annealing ranges.

One motivation for considering the TiO_2-SiO_2 pseudobinary alloys is the relatively low-energy onset of optical absorption in TiO_2, which occurs near 3.1 eV. As a result, the dynamics of the Ti-ion valence and conduction orbitals can be investigated by tabletop laboratory techniques in the visible to vacuum-ultraviolet spectral ranges, making it a highly accessible system for study. By coordinating SE data with XAS and XPS data, it is possible to obtain a more thorough understanding of the coordination chemistry of the TiO_2-SiO_2 system over the full compositional and annealing temperature range, and in particular to demonstrate the particular stability of the Ti-O-Ti group.

As an example of the type of questions to be addressed, natural TiO_2 typically exists in one of three polymorphic crystalline forms: rutile, anatase, and brookite. In all three polymorphs, the Ti ion exists in an oxidation state of +4 and is 6-fold coordinated, surrounded by 3-fold coordinated oxygen anions in a distorted octahedral structure. It is well known that Ti silicates can exist as amorphous glassy solids. In these Ti silicates, when the percentage of Ti is sufficiently low, it enters a 4-fold site ordinarily occupied by Si. In these Si sites, the Ti cations adopt a 4-fold coordinated tetrahedral structure surrounded by 2-fold coordinated O anions. For each of these coordination systems, and other valences that are not investigated in this thesis, different spectroscopic signatures occur due to the specific crystal field produced by the different ligand environments. We are interested in the coordination

of Ti in these alloys as a function of Ti composition, and in particular, obtaining information about what drives the 4- to 6-fold transformation and under what conditions it occurs.

The motivation for the second part of the thesis, that involving shallow-d-core-level reflectance data, is to establish whether a multiplet picture has anything to offer by way of understanding these measurements. These data, some of which were never published, were obtained some 30 years ago and were interpreted at that time by one-electron band theory. The recent successes of Prof. Lucovsky regarding the application of multiplet theory to the core-level spectroscopy of transition-metal oxides raise the question of whether one-electron, i.e., band, theory can be applied usefully to understand the shallow-d-core-level spectra. The question is also relevant because the one-electron approach did not succeed in explaining higher-lying features in reflectance spectra. Therefore, it appeared worthwhile to re-examine the shallow-core-level reflectance data using the multiplet approach. One notable result of the work, which is described more fully below, is that it shows that the interpretation of the observed splitting of the structures in the reflectance data as a universal spin-orbit splitting of the Ga3d core hole cannot be supported. Crystal-field effects are a major factor.

1.3 Detailed results and conclusions.

In this section I outline the intellectual accomplishments that resulted from this work. In particular, I am excited to present novel modeling considerations on the relatively well studied Ti silicate alloy system and core-level data forthe less well studied Ga-containing semiconductor systems.

1.3a Spectroscopic ellipsometer.

Spectroscopic ellipsometry (SE) is a linear-optical technique that is used to obtain the dielectric function (ε) of a material. The dielectric function is inherently a macroscopic quantity that relates the macroscopic or average displacement field *D* that is present in a material system to the macroscopic or average electric field E according to D= εE. However, while ε is a macroscopic quantity, its properties are dictated by the way charges in the material system respond, on the atomic scale, to the imposed electric field. This response is quantum-mechanical in nature and therefore needs to be treated as such. This technique probes transitions between the O valence and material conduction states, and is very useful for detecting crystalline inclusions in otherwise amorphous material.

We built a VUV spectroscopic ellipsometer that accesses the 4 to 9 eV spectral range, and used it to obtain the first SE data on Ti silicate alloys from 1.5 to 9.0 eV. Using these data and additional measurements on a bench SE that operates from 1.5 to 6.0 eV, we were able to obtain dielectric functions and verify significant coordination change occurring between 500 and 700 ºC

1.3b Local Ti coordination.

Our comparison of O K_1 and Ti L_3 data of samples with low Ti concentrations suggests the presence of the separate symmetry sites of 4-fold and 6-fold in-solution coordination in both as-deposited and annealed material. From XAS Ti $L_{2,3}$ data we obtained relative concentrations of 4-fold in-solution, 6-fold in-solution, and 6-fold phase-segregated Ti for as-deposited and annealed silicate alloys from 0 to 100% Ti. Also, we found conversion of 6-fold in-solution to 4-fold in-solution coordinated material driven by second nearest neighbors. We also found conversion of 4-fold-coordinated in-solution material to phase-segregated 6-fold coordinated material by annealing, driven by Ti-O-Ti bonds. In general this analysis showed for the first time that it is possible to distinguish 6-fold in-solution, 4-fold in-solution, and 6-fold phase-segregated material. It also provides motivation for coordination conversion in Ti silicate alloys over the full composition and annealing range.

We found that the relative-concentration data, through a mid-range fit to a stochastic model, indicates that a 4-fold in-solution to a 6-fold phase-segregated transition occurs upon annealing, and is driven by Ti-O-Ti bonding. Simple combinations of reference spectra were used to obtain coordination concentrations, after which a stochastic model was applied to the results. Our primary conclusion is that any 4-fold in-solution site with bridging Ti-O-Ti bonds has a strong tendency to drive Ti from 4-fold in-solution to 6-fold phase-segregated coordination. We also found convincing evidence from OK_1 data for phase segregation and striation effects through annealing. The OK_1 data and the plateau in the fitted Ti $L_{2,3}$ data indicate

near-complete 6-fold coordination in annealed samples with Ti concentrations of 36% or greater. Comparison with previous studies shows that this near-complete 6-fold conversion can be explained by the segregation of the Ti phase into striations, which the data indicate forms a laminating “capping layer”.

We demonstrated theoretically that the $2p^5 3d^1$ final states of the Ti $L_{2,3}$ spectra do not maintain any significant degeneracy, even in the absence of a crystal field. Significant mixing, which redistributes the dipole selection rule, occurs when crystal-field effects are added.

1.3c Shallow-d-core-level spectra in Ga-containing semiconductors.

We show the usefulness and investigate the cability of a local-field atomic-like calculation to model shallow d-core transitions in a covalent semiconductor material. I find that the observed splitting of the Ga3d orbitals in shallow core transitions may not be solely due to the spin-orbit interaction, but that it is influenced, if not dominated, by a crystal-field effect brought about by the surrounding positive charge distribution of the anions.

Specifically, I model the shallow-d-core-level reflectance spectra of the $GaAs_{1-x}P_x$ alloy series, GaSb, and GaSe as localized atomic excitations. The atomic-multiplet calculation enables me to determine eigenvalues and dipole-allowed transition matrix elements for these transitions as well as fitted radial strengths for perturbative Hamiltonian terms, that is, the crystal-field splitting and the spin-orbit interactions of the 3d core hole and the 4p excited electron.

Using a “covalent” crystal field, I explain the observed reversal of the crystal-field splitting as well as the necessary reduction of the hole spin-orbit parameter in GaAs. Reasonable representations of the features in the second-energy-derivative spectra are achieved and understood in context of anion location in the periodic table.

1.4 Why Ti silicates: Importance and summary of previous work

Titanium silicates and their endpoint constituents have a number of important applications that motivate investigation. The number and variety of uses of SiO_2 are abundant. TiO_2 also has a wide variety of common applications. It is popularly known through its usefulness as the safe alternative to PbO_2 in commercial paints. In addition, TiO_2 has been used in many applications, including as an industrial catalyst for both thermal and photo-induced chemical reactions.[1,2]

For the Ti-silicate system, there are a number of current and possible future applications. Ti silicates are particularly useful because a specific composition has a near-zero thermal-expansion coefficient. A particularly noteworthy application is the primary mirror of the Hubble Space Telescope, which is fabricated from an ultra-low expansion (ULE) glass containing 7.5% TiO_2. This composition produces a homogeneous glass with a near-zero coefficient of linear thermal expansion.[3]

The Ti silicate system has been investigated extensively as a catalyst. This research has focused on discovering specific catalytic mechanisms, which possibly correlate with site coordination and bonding configurations. Ti silicates now find significant use as industrial catalysts. For these applications, Ti silicates are typically formed as mesoporous materials in a zeolite structure. These systems are

currently used by companies such as Plimeri Europa in industrial oxidation reactions with hydrogen peroxide. As a broad research topic, there has also been considerable interest in group-4 transition-metal oxides as replacements for SiO_2 as the gate dielectric in complementary metal-oxide-semiconductor (CMOS) devices.

Attempts to understand transition-metal chemistry and the electronic nature of transition-metal atoms and complexes have been at the heart of solid state physics since the earliest days of quantum theory. From Bethe and Van Vleck to the present, the role of d-orbitals and d-orbital electrons in material systems has been a compelling and important topic of research. For this study, the literature shows that much work has been done on understanding Ti coordination chemistry in various Ti complexes. Studies conducted in an attempt to understand the electronic structure and transitions include experimental work by XAS, EELS, and XPS, as well as quantum calculations from the one-electron approximation onwards. I present an overview of relevant studies.

Many of the compositions are given in past studies as weight percent (wt%) as opposed to molecular fraction $(TiO_2)_x(SiO_2)_{1-x}$. These are easily converted by the following equation:

$$wt\%_{TiO_2} = \frac{x \cdot (mw_{TiO_2})}{x \cdot (mw_{TiO_2}) + (1-x) \cdot (mw_{SiO_2})}$$

(mw = molecular weight)

which transforms to:

$$x = \frac{mw_{SiO_2}}{\frac{mw_{TiO_2}}{wt\%_{TiO_2}} + mw_{SiO_2} - mw_{TiO_2}}$$

Evans[4] performed a study of Ti silicate glasses of of 3.4 to 10.8 wt% TiO_2 prepared by flame hydrolysis by P. C. Schultz. X-ray diffraction patterns were obtained for both as-prepared and annealed samples, where annealing meant heat treating for 1 hour at 1540 ºC and "longer times" at 1450 ºC. The results were found to be identical between the as-prepared and annealed samples and indicated an increase in unit-cell dimension with increasing wt% TiO_2. This increase in unit-cell size was interpreted as an indication of a "true solution" of TiO_2 in SiO_2 as opposed to phase segregation of crystalline material.

While employed at Corning, Schultz published two papers on SiO_2-TiO_2 glasses in the 1970s. The first paper, published in 1972 with H. T. Smyth, investigated fused silica doped with 0 to 10 wt% TiO_2.[5] The second paper, published in 1976, examined binary titania-silica glasses containing 10 to 20 wt% TiO_2.[6] Schultz reported that "good quality glasses were obtained" for the 0 to 10 wt% series. All the glasses in their unannealed state had a yellowish-brown tint, but appeared "water white" when annealed to 1050 ºC. He attributed the brown tint to small amounts of Ti^{+3} ions (~ 10 ppm), which oxidize to Ti^{+4} after annealing. He purports this to be substantiated by magnetic susceptibility measurements as well as ultraviolet absorption measurements. In general, much work is focused on either

proving that Ti will, in fact, incorporate into SiO_2 as 4-fold coordination or that a Ti silicate compound will be useful as either a low expansion glass or a catalyst.

General work on the specifics of transformation stability over a compositional or annealing range due to ligand arraignments, is in general missing in the literature. To the author's knowledge, this thesis is the first attempt to systematically quantify the percentage of 4-fold and 6-fold coordinated ions in an alloy series through the analysis of direct XAS measurements over a broad enough range to connect coordination changes to specific bonding considerations.

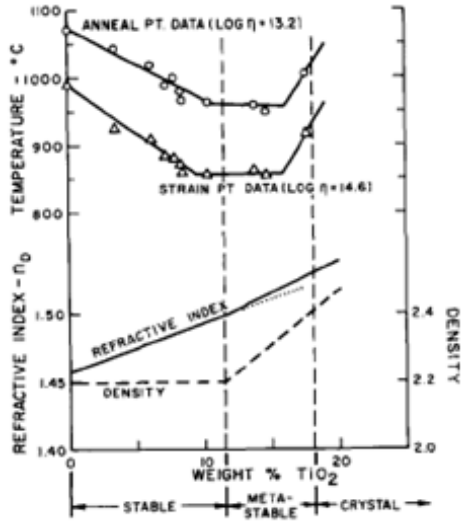

Figure 1.1 Effect of TiO_2 content on selected physical properties of unannealed TiO_2-SiO_2 glasses. (from Shultz 1972)

In the work of Schultz, density and expansion coefficient values were only presented for annealed samples (Fig. 1.1). They show a faintly decreasing (.004 g/cc from 0 to 9.45 wt% TiO_2) but nearly identical set of densities for all annealed compositions, indicating a consistent crystal structure. This decrease may be due to the increased length of the Ti-O bond relative to the Si-O bond.

In his 1976 paper, Schultz presented data on a series of SiO_2-TiO_2 glasses from 10 to 20 wt% TiO_2. Figure 1.2 reproduces a table from this work that shows that samples with a wt% of about 11 (clear except for a brown tint) are consistent with the 0-10wt% TiO_2 sample data presented earlier. His samples show good glass

formation properties up to 16.8 wt% TiO_2. At this composition, he reported that the glass remained transparent even after annealing for 1 hour at 960 ºC. In comparing this result with other regions of the boule that also yielded the 16.8 wt% TiO_2 sample, Schultz found that at 18.5 wt% TiO_2 the unannealed sample was “semi-translucent white” and at 19.4 wt% it was “dense white and opaque”, thereby placing the limiting composition for clear glass formation between 16.8 and 18.5 wt% for this production process.

Table I. Compositions/Descriptions of Binary TiO_2-SiO_2 Glasses Prepared for This Study

Boule No.	Sample location*	Nominal TiO_2 (wt%)	Visual description
1	Top	10.7	Clear glass, brown tint
	Bottom	10.3	Clear glass, brown tint
2	Top	14.9	Clear with opaque bands
	Bottom	13.8	Clear glass, blue tint
3		14.7	Clear glass, blue/brown tint
4		16.3	Clear glass, blue/brown tint
5	Top	18.5	Semi-opaque
	Middle	19.4	Opaque
	Bottom	16.8	Clear glass, blue tint
6		17.7	Opaque

*Vertical region in boule from which sample was taken.

Figure 1.2 Compositions/Descriptions of binary TiO_2-SiO_2 glasses (from Schultz 1976)

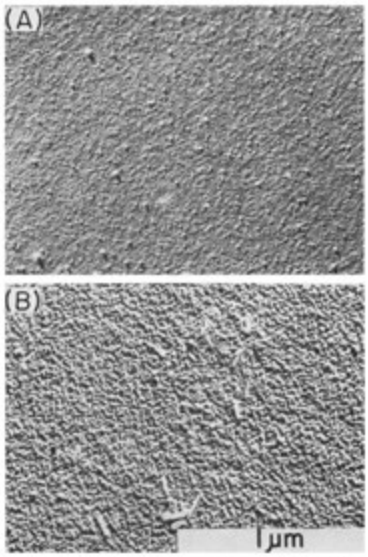

Fig. 8. Replica electron micrographs of etched specimens of SiO_2-TiO_2 glass 2 (A) unannealed and (B) annealed at 960°C for 1 h.

Figure 1.3 Electron micrographs of 13.8 wt% TiO_2 A) unannealed and B) annealed at 960°C for 1 hour.

Looking again at Fig. 1.1, viscosity, refractive index, and density data were compiled for both sets of samples prepared by Schultz. Schultz proposed that the discontinuity at 11 to 12 wt% TiO_2 indicates a structural rearrangement. He pointed out that, in the 0 to ~10 wt% TiO_2 range, 4-fold-coordinated Ti ions produce Si-O-Ti bridges that have lower bond energies than Si-O-Si bridges. The decreasing annealing and strain temperatures

with respect to increasing Ti concentration are a consequence of this lower bond energy at the Ti sites. Those materials with approximately 10-16 wt% TiO_2 compositions can be considered “metastable glasses”, where some of the TiO_2 has precipitated out of the continuous 4-fold coordinated network. Schultz believed that this precipitation may take “the form of phase separation and/or 6-coordinated Ti”. This will result in an increased concentration of Si-O-Si bridges in the continuous network, as well as the production of relatively rigid sections that are TiO_2-rich. The combinations of these two regions result in a “stiffening of the network” and an overall density increase due to the much higher density of TiO_2 (4.26 g/cm^3 for rutile vs. 2.202 g/cm^2 for vitreous silica).

Schultz examined electron micrographs of his clear glass sample (13.8 wt% TiO_2), both unannealed and after annealing at 960 ºC for 1 hour. The micrographs are shown in Figs. 1.3 and 1.4. The unannealed sample had a small amount of a spherical second phase, reported as glassy by other sources. The annealed sample contains a large amount of a second phase as well as “some well-developed crystals”. This second phase was characterized

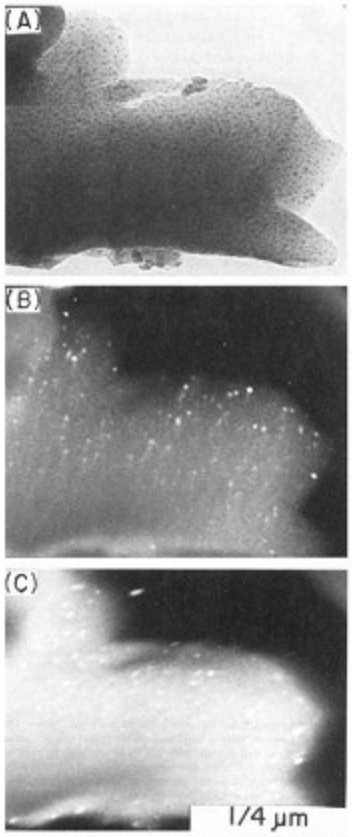

Fig. 9. Transmission electron micrographs of ion-thinned SiO_2-TiO_2 glass 2 annealed at 960°C for 1 h. (A) Bright-field image and (B) and (C) dark-field images at different angles.

Figure 1.4 Transmission electron micrographs of ion-thinned 13.8 wt% TiO_2 annealed at 960˚C for 1 hour. A) Bright-field image and B) and C) dark-field images at different angles.

through bright-field transmission electron microscopy as discrete droplets dispersed in a homogeneous disordered matrix. Both electron diffraction and dark-field transmission electron micrographs indicate that the majority of the droplets are anatase.

Schultz's work was expanded upon in a paper written by Sandstrom in 1980.[7] EXAFS data were obtained for unannealed samples with 7.5 and 9.5 wt% TiO_2, and Ti K-edge XAS data was gathered on unannealed samples with 3.4, 7.5, and 9.5 wt% TiO_2. The EXAFS data indicate a predominately 4-fold environment with ratios for 4- to 6-fold given in Fig. 1.5. Their XAS data corroborate that conclusion. Sandstrom concluded that TiO_2-SiO_2 glasses containing 3.4 to 9.5 atomic percent TiO_2 were predominantly 4-fold O coordinated with an average Ti-O bond length of 1.82 +/- 0.02 Å. Evidence was also discovered for 6-fold coordinated Ti with a Ti-O bond length of 2.1 Å, and that the "ratio" of 6-fold to 4-fold Ti increases with increasing TiO_2 composition.

Table 1
Summary of EXAFS results for Ti in SiO_2 glasses

Sample	Shell	N	R(Å)	$\Delta\sigma^2$(Å^2)	Fractional Ti coordination 6-fold : 4-fold
7.5% TiO_2	1	4.4 ± 0.5	1.81 ± 0.02	0.003	(0.05 : 0.95) ± 0.07
	2	0.9 ± 0.5	2.18 ± 0.05	−0.003	
9.5% TiO_2	1	3.8 ± 0.5	1.82 ± 0.02	−0.002	(0.18 : 0.82) ± 0.07
	2	1.6 ± 0.5	2.11 ± 0.05	0.001	

Figure 1.5 Table of EXAFS results for Ti in SiO2 glasses (from Sandstrom 1980)

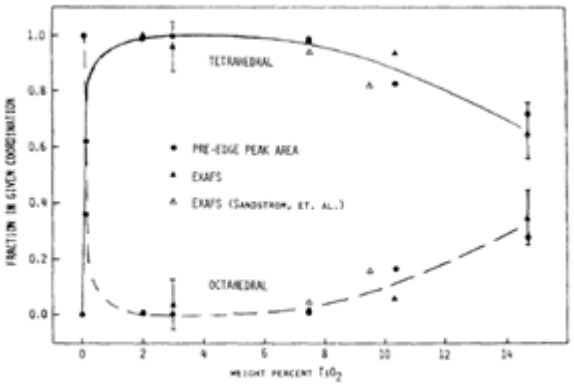

Fig. 10. Estimates of the fraction of Ti in fourfold and sixfold coordination versus composition. The solid triangles are from EXAFS data, the open triangles from Sandstrom et al. [9], and the solid circles from XANES.

Figure 1.6 Summary of estimates of Ti coordination fraction versus composition (from Greggor 1983)

Shown in Fig. 1.6 are the results of additional EXAFS AND XAS studies that were presented by the Schultz group in a paper written by Greegor in 1983.[8] Data were collected on unannealed samples prepared by flame hydrolysis, with TiO_2 wt% ranging from .012 to 14.7. Greegor reported that with concentrations below 0.05 wt% TiO_2, Ti exists in a rutile-like octahedral coordination. Up to 9 wt% TiO_2, they put forth the interpretation that Ti is best described by a two-site model (4-fold and 6-fold coordinated), with Ti predominately existing in 4-fold coordination. Finally, their analysis indicated that above 9 wt% TiO_2, the ratio of 6-fold to 4-fold sites increases dramatically until approximately 15% wt% TiO_2, when crystalline TiO_2 phase segregates. Furthermore, Greegor indicated that all Ti in the glass is in an oxidation state of 4+.

In the early 1970s Fisher conducted X-ray emission and absorption experiments to obtain the Ti $L_{2,3}$ spectra of various Ti and V compounds, as well as the TiL_3 Ti K and O K_1 of rutile TiO_2.[9,10] These studies presented the first picture of the molecular orbital electronic structure of the ground state of rutile TiO_2.

In 1982, Leapman conducted electron energy loss spectroscopy (EELS) experiments and obtained $TiL_{2,3}$ spectra of various transition-metal compounds including TiO_2.[11] He analyzed his data with single-electron calculations and was the first to notice that the L_3-to-L_2 white-line intensity ratio is 0.8:1, which disagrees substantially with the 2:1 ratio expected from statistics.

In other works, Brydson performed EELS studies on TiO_2 in both crystalline anatase and rutile forms.[12,13] He studied both ground-state and dynamic Jahn-Teller effects

to understand the Ti K_1 and O K_1 line spectra. de Groot presented XAS data for a variety of Ti-bearing minerals (PCM 1992) and described the Ti $L_{2,3}$ lineshape in terms of atomic multiplets. He performed calculations depicting how the shape of this line changes with respect to Ti oxidation state[14], Ti coordination[14], and both trigonal and tetrahedral distortions of the basic TiO_2 rutile octahedral structure.[15] Henderson presented L-edge XAS spectra on various Ti compounds and alloys, including TiO_2-SiO_2 glasses prepared using the sol-gel method.[16] The sol-gel method produces "homogenous glasses up to 7.4% wt% TiO_2" and heterogeneous glasses up to his sample composition limit of 14.9%. He concluded that Ti is predominantly 5-fold coordinated, in a square pyramidal structure, at <3.6 wt% TiO_2 and 4-fold coordinated, in a tetrahedral structure, at >3.6 wt% TiO_2 up to his weight-percent range of 14.9% TiO_2. Most importantly, their research indicated a complete lack of 6-fold coordinated Ti up to 14.9% TiO_2.

Recently, Lucovsky and his group have worked on transition-metal oxides to understand spectroscopic features in terms of 3d crystal-field symmetry breaking, with the objective of gaining a better understanding of these materials and the defects in them so as to provide direction for their use in integrated-circuits technology.

The present work, which includes an analysis of some of the data from the Lucovsky group, is a study of a full set of Ti silicate alloys and the change of Ti coordination and distortion through the alloy series and post-deposition annealing.

1.5 Theoretical Overview

Understanding the Ti silicate system requires knowledge of their electronic properties on an atomic and bonding scale, as well as their material properties on a macroscopic structural scale. Hence, these investigations will include real-space examinations as well as investigations of the electronic structure of the studied systems. To understand how the electronic structure correlates with the real-space configuration, a comprehensive review of various theoretical methods is undertaken. Many theoretical approaches are available for calculating the electronic structure of transition-metal systems. These include crystal field theory, molecular-orbital theory, ligand-field theory, and theories including the Jahn-Teller effect. All are primarily based on group theory and focused on symmetry considerations. These approaches are all well known and have produced results that are also well known. These results will be summarized in later sections.

In the theoretical sections, the methods used to understand Ti coordination in the Ti silicate system will be outlined. The focus will be on understanding and interpreting spectroscopic data obtained on this system, specifically data on the O K_1 and Ti $L_{2,3}$ edges obtained by near-edge X-ray absorption spectroscopy (XAS) and X-ray photoemission spectroscopy (XPS). Data also include those obtained by spectroscopic ellipsometry (SE).

I modeled the atomic multiplets of much of the Ti-silicate alloy system using the atomic-structure code of Cowan overlaid with a graphical user interface developed by de Groot. The calculations are perturbation-based and the final

outputs the results of a solved eigensystem. That is, the eigenvalues are the critical point energies and the eigenvectors are the vector moments that are the complex dipole-allowed components used to obtain transition probabilities. Through the theoretical interpretation of the spectroscopic data, insight is gained into Ti coordination at different Ti concentrations, including local structure as well as the amorphous-to-crystalline transition within the Ti silicate system.

Nearly all of the multiplet calculations and all of the nonlinear least-squares fitting of the data for the Ga-containing semiconductors were done using in-house code written in Mathematica by the author.

1.6 Experimental Overview

Studies of the electronic transitions of the Ti silicate samples were carried out on data obtained by X-ray photoemission spectroscopy (XPS), near-edge X-ray absorption spectroscopy (XAS), and vis-VUV spectroscopic ellipsometry (SE). The XPS measurements were done by students in the Opila Laboratory at the University of Delaware, and were provided by Les Fleming. The investigation starts with the Si $L_{2,3}$ transition, which involves excitation and removal of an electron from the Si 2p core states, then moves to the Ti $L_{2,3}$ initial state, which involves excitation and removal of the electron from the Ti 2p core states, and then moves to the OK_1 edge, which involves excitation and removal of an electron from the O 1s core states. XPS data record the energy of the emitted electron. The advantage of XPS is that it gives a clear picture of the valence of the ion being studied and provides information about the core levels *without* the added complication of multiplet effects resulting

from the presence of the final state electron in the material. We also use these data to assess whether the various structures in the XAS data are associated with localized final states or resonances that overlap the continuum.

These multiplet complications are unavoidable in XAS. Here, X-rays are absorbed by the sample at various wavelengths according to how the electrons in the system are affected by the incoming radiation. At appropriate energies that depend on the material, X-rays induce direct electronic transitions to conduction states. When an electron from the valence band falls into the resulting empty core level, either coherently during the absorption process or later, other electrons are ejected from the sample. The current needed to neutralize the resulting charge is monitored as a measure of the absorption. The XAS data that are analyzed here were obtained at Stanford Synchrotron Radiation Laboratories (SSRL) at the Stanford Linear Accelerator Center (SLAC) by the Lucovsky Group. These were collected on Ti silicate samples of various compositions, both as-deposited and annealed at 900ºC. We shall examine the total electron yield to understand 2 separate sets of electronic transitions. The first are the O K_1 transitions, which are excitations of an electron from an initial closed shell state of O to a final state consisting of an O1s hole and 3p electron. The second are the Ti $L_{2,3}$ transitions, which involve excitations from an initial closed state to a final state consisting of a Ti 2p hole and a 3d electron.

1.7 Thesis Overview

This investigation into the coordination chemistry of the Ti silicate system will proceed as follows. Chapter 2 is an explanation of the basic theoretical approaches used to understand and explain our topic. Chapter 3 details experimental methods. In Chapter 4, the Ti silicate results are presented and discussed. In Chapter 5, the results for the Ga-containing semiconductors are presented and discussed. Finally, in Chapter 6 the results are summarized, conclusions drawn, and recommendations made for future work.

1.8 References

1. V. E. Henrich, G. Dresselhaus, and H. J. Zeiger, Phys. Rev. Lett. 36, 1335 (1976)

2. R. H. Tait and R. V. Kasowski, Phys. Rev. B 20, 5178 1979.

3. D. S. Tucker, A. T. Nettles, H. Cagle, Journal of Materials Science Letters 21, 2002, 911– 91312.

4. Evans, D.L. (1970): Solid solution of TiO2 in SiO2. J. Am Ceram, Soc. 53.418-419

5. P. C. Schultz and H. T. Smyth; pp. 453-61 in Amorphous Materials. Edited by R.W. Douglas and Bryan Ellis. John Wiley & Sons, Ltd., London, England, 1972.

6. P.C. Schultz, "Binary titania-Silica Glasses Containing 10 to 20 Wt% TiO_2 ", J. Am. Ceramic Society, 59, 214-219 (Jun. 1976)

7. D.R. Sandstrom, F. W. Lytle, P.S.P. Wei, R. B. Greegor, J. Wong, and P. Schultz , Journal of Non-Crystalline Solids 41 (1980) 201-207

8. R. B. Greego F. W. Lytle, D. R. Sandstrom, J. Wong, and P Schultz, Journal of Non-Crystalline Solids 55 (1983) 27-43

9. David W. Fischer, Journal of Applied Physics, 41, 3561, 1970

10. David W. Fischer, Physical Review B, 5,4219 1972

11. R.D. Leapman, Physical Review B, 26, 614, 1982

12. 1987-BRYDSON-SolidStateCommunications64609—612

13. 1989-BRYDSON-JournalOfPhysics-CondensedMatter1797—812

14. F.M.F. de Groot, M.O. Figueiredo, M.J. Basto, M. Abbate, H. Petersen, and J.C. Fuggle Phys Chem Minerals (1992) 19:140-147

15. F. M. F. de Groot, J. Electron Spectrosc. Relat. Phenomena 67 (1994) 529.

16. Henderson, G.S., Liu, X. and Fleet, M.E. (2002) A Ti *L*edge X-ray Absorption study of Ti-silicate glasses. *Physics and Chemistry of Minerals*, **29**, 32 – 42.(2002)

2. THEORY

2.1 Argument for atomic-like calculations

These sections are aimed primarily at the theoretical treatment of transitions originating at shallow d core levels in the Ga-containing materials, but they include general background material and that relating to excitations from core levels to empty d orbitals in the Ti silicates as well. Approximately twenty years ago, at a Conference on the Physics and Chemistry of Surfaces and Interfaces (PCSI), Professor J. D. Dow remarked that the question to which band structure is the answer is not necessarily relevant to condensed-matter physics. With this statement in mind, and the general inability for band theory to present sufficient correct and consistent results for anything more than direct valence-to-conduction band transitions, it is necessary to look to atomic physics and specifically multiplet theory. We will be considering transitions between closed-shell initial states and electron-core-hole final states to best understand features in the spectra of both ionic and covalent-like systems.

One of the most difficult tasks to perform successfully is to argue the validity of a model calculation that is somewhat reasonably outside the model of a first-principles (ab-initio) type theory. Our calculations are essentially atomic-like, where we go from a closed-shell ion to a particle-hole state consisting of hydrogenic type orbitals (for example a d core hole and a p electron). Here we make arguments validating the possible use of an atomic-like approach for modeling. One way is to just simply state that the ion exists, from a local point of view, as a lone hydrogenic

entity residing in a charge environment. For the shallow core-level systems, this argument is equivalent to assuming that the atom resides in an ionic-like environment, but treating its Hamiltonian as if it exists in a purely covalent system (no Coulomb interaction terms). While this undoubtedly looks like a case of "having our cake and eating it, too", it establishes an environment that allows us to at least attempt to model the shallow-core-level transitions. One factor in our calculations, which points to their consistency, is that the magnitude of the crystal-field splitting is substantially less for the III-V system than for a system like titanium dioxide.

Attempting to justify an atomic-type calculation directly from an *ab initio* or molecular-orbital consideration is difficult, at best. The best description can be thought of as sp^3-cation hybridized orbitals to sp^3-cation hybridized orbitals. However, the only particle-hole combinations (the only configuration that concerns us here) that are dipole-allowed from the nominally closed-shell state are those involving Ga 3d holes and 4p electrons. The 4p electrons are dealt with as atomic-like orbitals, but for conceptualization purposes they are considered as being formed in antibonding-like states with respect to the sp^3-sp^3 states. In our considerations the 3d hole – 4d electron configurations are perturbed by the sp^3-sp^3 bonding states and the anion cores with respect to the crystal-field effects as well as the spin-orbit splitting of the 3d holes and the 4p electrons.

In general, we refer to deGroot's[3] explanation of the single electron approximation used for core level spectroscopies. This approximation is motivated through Fermi's golden rule with the dipole approximation.

$$W_{fi} \propto \sum_{q} |\langle \Phi_f | \hat{e}_q \cdot r | \Phi_i \rangle|^2 \delta_{E_f - E_i - \hbar\omega}$$

The given initial and final states are not known. We will be using single particle atomic wave functions, correlated as appropriate for atomic multiplets of more than one particle about the atom, as our simple model wave functions. Correlations between the final states excited electron and hole wave functions are the basis behind the atomic multiplets and follow directly from the one electron atomic approximation. The basis for appropriate ions (ie Ga^{+3}) is that the electrons pointed in the formal valence are used in the bonding configurations and the entity calculated, in the one electron approximation, is the same very same ion with the formal valence.

2.2 Calculation of atomic muliplet effects for closed shell initial states to electron-hole final states

Here we provide details that describe the local atomic-like multiplet calculations used to model the shallow d-core level transitions. Multiplet effects play an important role in any transition that involves a core hole other than a 1s in either the initial or final state.[2] For K-edge transitions, it may be appropriate to use simple single-electron scattering calculations that deliver a density of states and can be interpreted in a direct way. However, for L edges, simple density of state calculation is in poor agreement with XAS data. This is not due to incorrectly calculated densities of states, but rather to a strong overlap between the core and valence wave functions. For a model case we discuss first a Ti $L_{2,3}$ transition where the Ti

cation is in the +4 valence state and where the 2p core electron is excited into an empty 3d valence orbital. The excitation can be described as $2p^6 3d^0 \rightarrow 2p^5 3d^1$. Later we shall look at shallow core level transitions which we model as coming from a Ga^{+3} ion through a $3d^{10}4p^0 \rightarrow 3d^9 4p^1$.

Our calculations are a perturbation type calculation done in the Heisenberg matrix formalism. We now consider our perturbation Hamiltonian, which includes both intrinsic effects within the local atomic picture and extrinsic effects due to the electronic system surrounding the cation. The intrinsic terms include the direct Coulomb interaction, the Coulomb exchange interaction, the spin orbit interaction between the core levels, and the spin-orbit interaction between the electron levels. The extrinsic term describes the effect of the crystal field produced by the surrounding ligands.

The perturbative Hamiltonian consists of:

$$H_{per} = \frac{\vec{P}_{hole}}{2m_{hole}} + \frac{\vec{P}_{electron}}{2m_{\cdot}} + \cdot_{\vec{\cdot}_{electron}\ \vec{\cdot}_{hole}\ |\vec{\cdot}_{electron}\ \vec{\cdot}_{hole}|} \qquad ron\,/\backslash\,\cdot_{electron}\ \vec{\cdot}_{electron}\,/$$

$$+\xi(\vec{\cdot}_{hole}\,/\backslash\,\cdot_{hole}\ \vec{\cdot}_{hole}\,/\,\cdot\cdot_{cf}$$

$$\xi(\vec{\cdot},\qquad \frac{\cdot^2}{2m^2c^2r}\frac{dV(\vec{\cdot},}{dr}$$

$$H_{per} = E_{avg} + \sum_{k} f_k\left(l_1 l_2\right)F^k\left(l_1 l_2\right) + \sum_{k} g_k\left(l_1 l_2\right)G^k\left(l_1 l_2\right) + \xi(\vec{\cdot}_{electron}\,/\backslash\,\cdot_{electron}\ \vec{\cdot}_{electron}\,/$$

$$+\xi(\vec{\cdot}_{hole}\,/\backslash\,\cdot_{hole}\ \vec{\cdot}_{hole}\,/\,\cdot\cdot_{cf}$$

$$H_{per} = E_{avg} + H_{dircoul} + H_{exchcoul} + H_{SOE} + H_{SOH} + H_{cf}$$

The final perturbation Hamiltonian equation on the previous page lumps all given effects into 6 final terms. We see the first term describes the average energy, which is a measure of the combined overall kinetic and one electron Coulomb interactions with the core of the hole and electron, and is diagonal in all basis sets. The second and third terms are the direct and exchange columbic terms, diagonal in the LS basis set. These terms which result the single 2 particle Coulomb term but splitting into a direct interaction between the hole and the electron and an exchange term resulting from the quantum exchange of the electrons in the differing shells. The fourth term is the spin-orbit splitting of the electron diagonal in the jj basis. The fifth is the spin-orbit splitting of the hole also diagonal in the jj basis. Finally, the sixth is the cubic crystal-field splitting term, which affects directly the d final state calculated but not necessarily diagonal in the uncoupled basis set. In a single-particle situation this splitting removes the initial five-fold degeneracy of the 3d levels and converts them into 2- and 3-fold levels commonly designated in group theory terminology as e_g and t_{2g}, respectively.

Multiplet calculations are essentially angular-momentum calculations, with the radial parts of the matrix elements being parameterized. The initial and final states are constructed in the basis set that is chosen to be the basis that is easily calculable for the perturbation term being considered. After all effects have been taken into account we then transform the basis set into something more useful for achieving the desired goal, for example to the LS representation to find the amplitudes of the dipole-allowed transitions. We then solve the eigensystem

obtaining eigenvalues which are used as the critical point values with the corresponding complex amplitude of the eigenvector components used as the transition probability for that critical point.

The direct and exchange Coulomb terms are calculated in the LS basis set. In LS coupling the interaction is the mutual Coulomb repulsion between the coupled particles. The Coulomb repulsion only affects the angular momentum. Therefore, it couples the angular momenta to give eigenfunctions of L^2 and L_z and the spins to give eigenfunctions of S^2 and S_z. The coupled angular momenta and spins then combine to produce eigenfunctions of J^2 and J_z, where J = L+S.

$$H_{dircoul} = \sum_k f_k\left(l_1 l_2\right) F^k$$
$$H_{exchcoul} = \sum_k g_k\left(l_1 l_2\right) G^k$$

$$f_k(l_1 l_2) = \left\langle l_1 \left\| \boldsymbol{C}^{(k)} \right\| l_1 \right\rangle \left\langle l_2 \left\| \boldsymbol{C}^{(k)} \right\| l_2 \right\rangle \boldsymbol{I}_{12}^{(k)}$$

$$g_k(l_1 l_2) = \delta_{bb'} \left\langle l_1 \left\| \boldsymbol{C}^{(k)} \right\| l_2 \right\rangle^2 \left[-\frac{1}{\left[l_1, l_2\right]} + \delta_{kL}\delta_{S0} \frac{4}{\left[L\right]} \right]$$

$$\boldsymbol{I}_{12}^{(r)} = -\left(-1\right)^{l_1+l_2+L+r} \begin{Bmatrix} l_1 & l_2 & L \\ l_2 & l_1 & r \end{Bmatrix}, r > 0$$

$$E(^1P^0) = E_{av} - 0.200F^2 + 1.267G^1 - 0.043G^3$$
$$E(^3P^0) = E_{av} - 0.200F^2 - 0.067G^1 - 0.043G^3$$
$$E(^1D^0) = E_{av} + 0.200F^2 - 0.067G^1 - 0.043G^3$$
$$E(^3D^0) = E_{av} + 0.200F^2 - 0.067G^1 - 0.043G^3$$
$$E(^1F^0) = E_{av} - 0.057F^2 - 0.067G^1 + 0.325G^3$$
$$E(^3F^0) = E_{av} - 0.057F^2 - 0.067G^1 - 0.043G^3$$

For calculation we show, on the previous page, equations which include the direct Coulomb and exchange Coulomb terms. General treatment to obtain these values for non-equivalent electrons can be found in Chapter 12 of Cowan.[1] $f_k(l_1l_2)$ and $g_k(l_1l_2)$ are the angular momentum parts of the direct and exchange Coulomb terms, respectively, while F^k and G^k are their given radial strength terms. These are the fitted parameters in calculations when these are included. Given values of k are results of the triangle inequality and k's other than these results in zero value through this consideration. We see $\delta_{bb'}$ which is notion for requirement of the same bra and ket LS states for the exchange term which is implicit in the direct term. Quantities in the bra-kets are reduced matrix elements of modified spherical tensors ($C^{(k)}$) also described in Cowan. The bracketed notation is a standard 6-j symbol. The last set of energy equations are the calculated splitting for the pd final states which are valid for both $3d^94p^1$ and $2p^53d^1$ states.

$^1P_1$ Singlet 3 = 3 Degenerate States

$^3P_{0,1,2}$ Triplet 1+3+5 = 9 Degenerate States

$^1D_2$ Singlet 5 = 5 Degenerate States

$^3D_{1,2,3}$ Triplet 3+5+7 = 15 Degenerate States

$^1F_3$ Singlet 7 = 7 Degenerate States

$^3F_{2,3,4}$ Triplet 5+7+9 = 21 Degenerate States

Shown above are the LS coupling basis states where the final total angular momentum (J) of a single particle is the vector sum of its orbital angular momentum and its spin angular momentum. For core-hole–conduction-state transitions, this

calculation is done separately for the electron and hole. To obtain the final J value the results are added vectorially. The direct and exchange Coulomb effects are diagonal in this basis set. In addition, it is very easy to find the dipole-allowed transitions in this set. These transitions are just those that are nonzero when finding the expectation value from the $^1S_0$ state (that of a closed shell system) of a dipole operator. The result is nonzero only for the $^1P_1$ (singlet P_1) final state. These terms are not included in Ga semiconductor calculations because of their highly covalent nature reducing the overlap integral of the electron hole.

$$H_{SO} = \xi(\vec{r}) \vec{l} \cdot \vec{s}$$

$$\xi(r) = -\frac{e}{2m^2c^2r}\frac{dV(\vec{r})}{dr}$$

$$H_{SO} = \frac{\xi}{2}\left(j(j+1) - l(l+1) - s(s+1)\right)$$

The jj term for both the hole and electron are calculated through the above commonly known spin orbit splitting equations. ξ(r) is the radial strength parameter for the spin orbit splitting. The jj basis sets, for which the spin orbit terms are easily calculable are formed by first vectorially combining the orbital angular momentum of the core hole with its associated spin, doing the same for the conduction electron, then combining the result.

$\left[\frac{1}{2},\frac{3}{2}\right]_{1,2}$ Doublet 3+5 = 8 Degenerate States

$\left[\frac{1}{2},\frac{5}{2}\right]_{2,3}$ Doublet 5+7 = 12 Degenerate States

$\left[\frac{3}{2},\frac{3}{2}\right]_{0,1,2,3}$ Quartet 1+3+5+7 = 16 Degenerate States

$\left[\frac{3}{2},\frac{5}{2}\right]_{1,2,3,4}$ Quartet 3+5+7+9 = 24 Degenerate States

Shown above are the jj basis states for a p hole d electron set of states. For a d hole p electron coupling the first j and second would be reversed. The relevant variables are the combined angular momenta j of the individual states, which take two values l±s in this case, and ξ, which is the effective radial strength of the splitting given by the gradient of the surrounding potential. This potential is usually dominated by the core. The sign of the core-hole spin-orbit splitting will be opposite that of the electron, because the hole effectively has a positive charge.

For calculating the crystal field term we use the uncoupled basis set, which is easily represented symbolically as a product of the single-electron orbital angular momentum and spin angular momentum wavefunctions.

$$\left|l_1, m_{l_1}\right\rangle \left|s_1, m_{s_1}\right\rangle \left|l_2, m_{l_2}\right\rangle \left|s_2, m_{s_2}\right\rangle$$

Above is a symbolic representation of this uncoupled basis set: For the full set of perturbations of the orbital angular momentums and intrinsic spin, for a pd coupling, there will be 60 states.

$$H_{cf} = \sum_{i=1}^{N} eq_i \left[A_{mm'} F_4(R_i) Y_4^{m-m'}(\vartheta_i, \phi_i) + B_{mm'} F_2(R_i) Y_2^{m-m'}(\vartheta_i, \phi_i) + D_{mm'} F_0(R_i) Y_0^{m-m'}(\vartheta_i, \phi_i) \right]$$

$$A_{mm'} = (-1)^{m'} \frac{10\sqrt{\pi}}{27} C_{-m'm}^{224} C_{00}^{224}$$

$$B_{mm'} = (-1)^{m'} \frac{2\sqrt{\pi}}{5} C_{-m'm}^{222} C_{00}^{222}$$

$$D_{mm'} = (-1)^{m'} \left(10\sqrt{\pi}\right) C_{-m'm}^{220} C_{00}^{220}$$

Our treatment of the crystal field is given above and follows that of Appendix 2 in Bersuker.[2] Strength parameters F_2 and F_4 are fitting terms and are the radial parts of the crystal field. We have 4th 2nd and 0th terms because of symmetry considerations. 4th and 0th exist for tetrahedral or octahedral symmetries, 2nd become non-zero for trigonal distortions. $A_{mm'}$ $B_{mm'}$ $C_{mm'}$ are coefficients and their internal Cs are Clebsch-Gordon coefficients. For a tetrahedral configuration the obvious two angular distributions are those with the charges set along the (111) directions and one with one charge set along the +z axis and 3 set along a trigonally symmetric configuration along the -z axis with equal radii to the center as with the first +z charge. Because of the need to include trigonal distortions in some of our calculations we will conduct all calculations in the later trigonal framework. However, it should be noted that either angular approach with overall tetrahedral symmetry will have no effect on the radial strength parameters.

The intensities of features in the lineshapes are primarily determined by the selection rules of the involved transitions. The selection rule for the dipole transition is that the dipole matrix element is nonzero for an orbital angular momentum change of 1. These include the transitions s→p, p→d, or the inverse transitions p→s, d→p.

We can also have multipole transitions, the next being the quadrupole transitions s→d, p→f, or the inverse d→s, f→p. However, quadrupole transitions are usually two orders of magnitude weaker than dipole transitions, so they can be safely ignored. For the Ti^{+4} and Ga^{+3} cation, the $^1P_1$ state in the LS coupling scheme are the only satisfactory end states for dipole transitions from the $^1S_0$ ground state. Thus, we must enquire how we obtain such a large number of transitions when only a single LS dipole-allowed transition. These multiple transitions occur because of the mixing of states due to the lowering of symmetry caused by perturbation terms. The general form of the XAS transition matrix elements are:

$$I_{XAS} \propto \left\langle 3d^0 \left| p \right| 2p^5 3d^1 \right\rangle^2$$

With LS symmetry aspects:

$$I_{XAS} \propto \left\langle \left[{}^1S_0 \right] \left\| \left[{}^1P_1 \right] \right\| \left[{}^1P \right] \right\rangle^2$$

In our perturbative calculation, all individual term matrices, transformed into the LS basis set for easy calculation of transition matrix elements, are added together. We then diagonalize the Hamiltonian, thereby obtaining its eigenvalues and eigenvectors. To convert these results into spectra, we take broadening into account by using Lorentzian lineshapes, choosing a reasonable width then placing them at the energy locations of the eigenvalues with amplitudes proportional to the eigenvectors. This modeled system establishes the function for our least-squares analysis.

2.3 Differences in Final State Configurations: Effect on XAS and XPS

Differences in XPS and XAS spectra are due to the final-state configurations of the separate transitions. Using as an example TiO_2 with Ti in a +4 valence state, the initial states for both spectroscopes are the full $2p^6 3d^0$ symmetry designated as $^1S_0$ in the LS terminology. From a zero-order perspective, for XAS we transition to a $2p^5 3d^1$ state. For XPS, because the electron leaves the system, we have a final state of $2p^5 3d^0$. Due to the absence of the d electron in the final state there are no crystal-field or 3d spin-orbit effects (the latter is typically negligible anyway). Also absent are the dd and dp Coulomb interactions. The remaining interactions include the 2p spin-orbit splitting and pp Coulomb effects.

2.4 Typical coordination structures of titanium silicate alloys

The nearest-neighbor coordination is of primary importance in determining the electronic structure of an ion. For this discussion we refer to complexes where there is a central cation surrounded by a number of anions forming ligand bonds. The coordination number is obtained from the number of nearest-neighbor bonding ligands. For instance, in the typical case of tetrahedral SiO_2, each Si atom is connected to 4 O atoms and each O atom to two Si atoms, hence Si has a coordination number of 4 while that of O is 2.

To find the likely coordination of Ti in the various titanate systems, we first look at the most commonly occurring forms of crystalline TiO_2. Rutile, anatase, and brookite all possess Ti in 6-fold coordination in various distorted octahedral configurations, as shown for example in Figs. 2.1 and 2.2. Figure 2.1 depicts the

unit cell of rutile, with the Ti ions in gray and the O ions in red. Ti maintains a distorted octahedral environment with two longer bonds that for these purposes is arbitrarily assigned to the O atoms at +z and –z. The four shorter bonds in the xy plane are compressed due to the fact that they do not maintain angles of 90 degrees with each other. Figure 2.2 depicts the unit cell of anatase again with the Ti ions in gray and the O ions in red. Anatase also maintains a distorted octahedral environment for Ti, with two longer bonds again at +z and –z and four shorter O bonds.

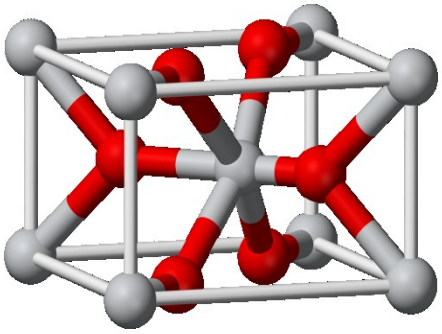

Figure 2.1 Rutile Unit Cell

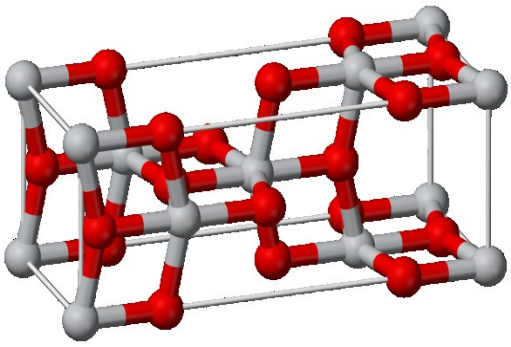

Figure 2.2 Anatase Unit Cell

We can now ask, what will be the likely coordination of a Ti cation if small amounts of Ti are present in SiO_2? We would suspect that Ti occurs as a 4-fold coordinated cation. It is known that this coordination environment exists: the example is Barium Orthotitanate (Ba_2TiO_4). For low Ti concentrations in SiO_2, the Ba_2TiO_4 example allows us to conclude that Ti can in principle substitute directly for Si in a 4-fold tetrahedral site. At first sight this appears to make sense because Ti maintains the same +4 formal valence as Si. However, upon closer examination it is apparent that this is an oversimplified perspective, because the sp^3 bonding of Si

depends entirely on the fact that the p orbitals that give rise to these bonds are antisymmetric and hence in combination with s can form directed orbitals essentially on one side of a (111) axis, whereas the bonding electrons in Ti are symmetric and so must extend equal distances both ways.

2.5 Modeling of coordination-complex modifications as a stochastic process

We can take advantage of basic probability theory to investigate the effect of nearest neighbors on the coordination change about an atom. Given that the composition of a sample can indicate the probability that an atom placed randomly in a system will be next to a particular atom, a probability calculation is a natural way to investigate what the various neighbor complexes are likely to be. However, this approach assumes that all processes involved are random. In particular, it is important to know that, while any event in a given process may be random over a short time scale, this might not be true in the long term. Hence the overall effects of a stochastic process may be discovered only over a large enough sample set. For the Ti silicate system the random process in which we are interested is the occupancy of the neighboring cations in a given Ti complex.

2.6 References

1. R. D. Cowan, *Theory of Atomic Spectra* (University of California Press, Berkeley, 1981).

2. I. B. Bersuker, *Electronic Structure and Properties of Transition Metal Compounds* (John Wily & Sons, Inc., 1996).

3. F.M.F. de Groot, Coordination Chemistry Reviews 249 (2005) 31–63

3. EXPERIMENTAL METHODS

3.1 Thin film preparation by remote-plasma-enhanced metal-organic chemical vapor deposition (RPE-MOCVD) and thermal annealing

The Ti silicate samples from which the XAS and XPS data were obtained were physically deposited by remote plasma-enhanced metal-organic chemical vapor deposition (RPE-MOCVD) on (100) Si wafers at 300 ºC by the Lucovsky group at North Carolina State University (NCSU). Silane and Titanium(IV) t-butoxide were used as precursors. The pressure during deposition was 3 millitorr. Following deposition, *in situ* plasma-assisted oxidation was performed at 300 °C.

3.2 X-Ray absorption spectroscopy (XAS)

XAS data was acquired by the Lucovsky Group at Stanford Synchrotron Radiation Laboratories (SSRL) at the Stanford Linear Accelerator Center (SLAC). X-Ray Absorption Spectroscopy (XAS) is a spectroscopic technique that is used to analyze the real-space and electronic structure of a material. This technique involves directing a beam of photons of selected X-ray energies at a sample. Electrons excited by these transitions leave the sample, creating a current that is measured. The current is proportional to the X-ray absorption. Absorption can either be detected directly, through measurement of the attenuated beam behind the sample, or indirectly by detecting the ejected electrons.

Denoting E_o as the binding energy of the electron, XAS spectra are usually divided into 4 separate regions:

1) Pre-edge ($E<E_0$);

2) X-Ray absorption near-edge structure (XANES) ($E = E_0 \pm 10eV$);

3) Near-edge X-ray absorption fine structure (NEXAFS) ($E = E_0+10eV$ to $E = E_0+50eV$);

4) Extended X-ray absorption fine structure (EXAFS) ($E = E_0+50eV$ to $E = E_0+1000eV$).

Here, we work with XANES. Through the investigation of these structures, much can be learned about the chemistry of the system involved, for example the oxidation state, the local coordination, and the electronic structure of the conduction states. It is important to have an understanding of the specific transitions involved when investigating the material in order to model the spectrum and extract appropriate properties. The Ti $L_{2,3}$ structure is discussed throughout this thesis. The above three properties mentioned will greatly affect the features seen, primarily due to the impact of multiplet effects. The detection event does involve Auger processes, but the total electron yield, which is the data, is an integrated average over these events with the structures being primarily influenced by the initial dipole matrix transition element. Auger effects may impact some of the local structure detected for XAS measurements and does, in fact, play a role in the broadening of the Ti L_2 spectra.

XAS Ti $L_{2,3}$ and OK_1 data on a series of Ti silicate thin films deposited on Si(100) as described above were obtained at Stanford Synchrotron Radiation Laboratories (SSRL) at the Stanford Linear Accelerator Center (SLAC) by the Lucovsky group. These films are characterized as pseudobinary alloys

$(TiO_2)_x(SiO_2)_{1-x}$ where x ranges from 0 to 1. Samples were examined both as-deposited and after annealing at 900 °C for 90 sec by a rapid thermal anneal (RTA) process. We investigate the fine structure present at the Ti 2p edge, as well as that at the O 1s edge. The Ti 2p edge produces the $L_{2,3}$ fine-structure spectrum, which is indicative of transitions from Ti 2p core orbitals initially in a closed shell Ti^{4+} $^1S_0$ spherically symmetric state to a final set of $2p^5 3d^1$ states, again about the Ti^{4+} cations. The O K_1 edge produces the O 1s fine-structure spectrum, which is due to transitions from initially closed O states to a coupled O 1s hole -- O 3p electron states.

3.3 X-Ray photoemission spectroscopy (XPS)

X-ray photoemission spectroscopy (XPS) is a core-level spectroscopy where the incident radiation ejects core-level electrons from the sample. The kinetic energy of the ejected electrons is recorded. We are interested in the binding energy, which is a measure of the energy difference between the core level states and the Fermi energy of the system. The total energy of the ejected electron is transferred from the incoming X-ray and converted to a combination of binding energy, kinetic energy, and the work function of the measuring system. Because the electron is transitioned to a continuum of states and is quickly removed from the atomic system, the initial to final transition will be of the form (for $TiL_{2,3}$ XPS for example) $2p^6 3d^0 \rightarrow 2p^5 3d^0$.

Because the interesting property is the kinetic energy of the escaped photoelectron, a large range of X-ray energies may be used above the binding

energy plus work function of the system. The resulting kinetic energy of the photoelectron will determine the mean free path of the electron as it transports to the surface. We are interested only in the core level binding energies, and therefore will be considering data obtained with relatively high X-ray energies and correspondingly large escape depths to eliminate any residual sensitivity to the surface.

The XPS data investigated here were taken on Ti silicate thin films in Professor Opila's laboratory at the University of Delaware, and were provided by Dr. L. Fleming. I requested these as they provide additional information about Ti coordination. All data are on as-deposited samples unless otherwise noted.

3.4 VIS-VUV spectroscopic ellipsometry[1]

Ellipsometers return information about the dielectric properties of materials by analyzing the change in polarization state of light reflected at non-normal incidence from a specular surface. Our laboratory already had a "bench" ellipsometer with a spectral range from 1.5 to 6.0 eV, but because the Ti silicates are wide bandgap materials, I constructed a vuv system that operates from 4 to 9 eV to obtain the necessary data. Except for the use of magnesium fluoride components, a vuv discharge lamp, and a container that allowed operation with either a purged N_2 ambient or a moderate

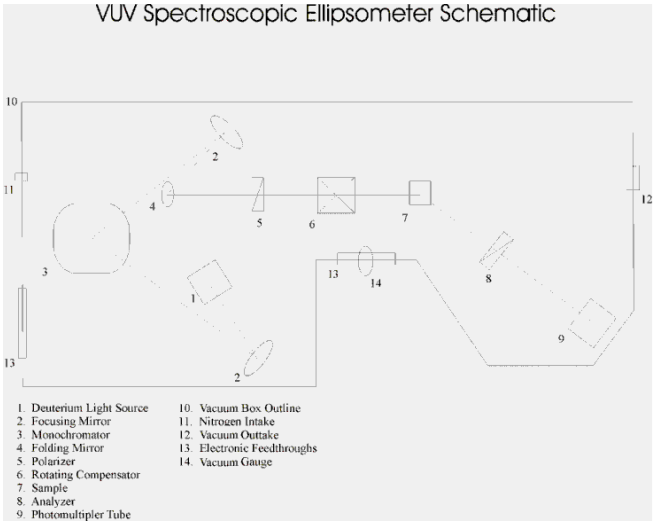

Figure 3.1 VUV Spectroscopic Ellipsometer Schematic

vacuum, the configuration was standard. It consisted, in this order, of a light source, monochromator, polarizer (a linear optical polarizer), a compensator (a waveplate or retarder), the sample (mounted to reflect the light into the analyzing components), an analyzer (a second linear optical polarizer) and the detector with all necessary focusing and folding optics between. Various components can be rotated, but to facilitate data acquisition I selected a rotating-compensator-ellipsometer (RCE) configuration, where the analyzer and polarizer are fixed at known azimuths with respect to the plane of incidence, and the compensator is rotated at a known rate. Design features that make this instrument unique are the MgF_2 optics and the airtight aluminum "tub" with a Lexan top with vacuum electrical feedthroughs. Oxygen has a sharp optical absorption cutoff at approximately 190nm (~6.52 eV). To acquire data in the required range, it was necessary either to flush the system with N_2 or to pump it down to approximately 10 millitorr. Either approach largely removed the UV absorptive O_2 from the system.

Ellipsometric data are analyzed using a system transfer function, which describes and parameterizes the ellipsometer through a set of Jones matrices. The Jones matrices describe how the different components act on the electric field vector of the light. Each optical element is represented by a 2x2 Jones matrix. Multiplying these together yields the output field, which when squared generates a Fourier series whose coefficients provide the information necessary to obtain the complex reflectance ratio $\rho = (r_p/r_s)$ of our sample. The system transfer function for the vuv ellipsometer is:

$$\begin{pmatrix} E_x \\ E_y \end{pmatrix} = \begin{pmatrix} 1 & 0 \\ 0 & 0 \end{pmatrix} \begin{pmatrix} Cos(A) & Sin(A) \\ -Sin(A) & Cos(A) \end{pmatrix} \begin{pmatrix} r_p & 0 \\ 0 & r_s \end{pmatrix} \begin{pmatrix} Cos(C) & -Sin(C) \\ Sin(C) & Cos(C) \end{pmatrix}$$

$$\begin{pmatrix} t_1 & 0 \\ 0 & t_2 \end{pmatrix} \begin{pmatrix} Cos(P-C) & -Sin(P-C) \\ Sin(P-C) & Cos(P-C) \end{pmatrix} \begin{pmatrix} 1 & 0 \\ 0 & 0 \end{pmatrix} \begin{pmatrix} E_x^i \\ E_y^i \end{pmatrix}$$

Once the complex reflectance ratio ρ is obtained, the sample is modeled in terms of the various relevant parameters (index of refraction/dielectric function, thicknesses, etc.), and the various parameters obtained by least-squares fitting. Because the samples we are investigating consist abstractly of multiple uniformly thick layers of different materials, we analyze samples using standard multilayer analysis.

The relevant Fresnel equations describing the optical properties of a multilayer stack are obtained as a solution to a standard boundary-value problem that is solved by imposing three requirements. First, normal D and B and tangential E and H are continuous through each boundary. Second, the projection of the wave vector k at the boundary, must be continuous through the entire system (the kinematic condition). Third, the dispersion equation must be satisfied in each material.

For the case of a 2 layer model consisting of a substrate in an ambient, the equations are:

s-polarized light:

$$E_o^l = \frac{1}{2}(1+\frac{n_{sppd}}{n_{oppd}})E_s^l + \frac{1}{2}(1-\frac{n_{sppd}}{n_{oppd}})E_s^r$$

$$E_o^r = \frac{1}{2}(1-\frac{n_{sppd}}{n_{oppd}})E_s^l + \frac{1}{2}(1+\frac{n_{sppd}}{n_{oppd}})E_s^r$$

p-polarized light:

$$H_o^l = \frac{1}{2}(1+\frac{\varepsilon_o n_{sppd}}{\varepsilon_o n_{oppd}})H_s^l + \frac{1}{2}(1-\frac{\varepsilon_o n_{sppd}}{\varepsilon_s n_{oppd}})H_s^r$$

$$H_o^r = \frac{1}{2}(1-\frac{\varepsilon_o n_{sppd}}{\varepsilon_o n_{oppd}})H_s^l + \frac{1}{2}(1+\frac{\varepsilon_o n_{sppd}}{\varepsilon_s n_{oppd}})H_s^r$$

The complex reflectance is described as the ratio of the emerging and the incident field. The three-phase model follows by solving the boundary conditions for another layer between substrate and ambient.

Linear Dielectric function:

The dielectric function (also known as the permittivity) of an isotropic medium is a scalar quantity that relates the displacement field D in a medium with the electric field E in the medium. The constant of proportionality is the dielectric function ε according to the constitutive relation

$$\vec{D} = \varepsilon \vec{E}$$

From first principles:

$$\vec{D} = \varepsilon_o \vec{E} + \vec{P} = \varepsilon_o \vec{E} + \varepsilon_o \chi \vec{E} = \varepsilon_o \vec{E}(1 + \chi)$$

where

$$p = \sum_{i=1}^{N} q_i r_i$$

.

The transitions probed with ellipsometry are the transitions from the O 2p filled states to the O 3s or 3p states affected by the surround cation environment. Data from 1.5 to 6 eV were acquired on a "bench" rotating-compensator ellipsometer (RCE) using a Xe arc lamp as a light source, quartz optics, and a photomultiplier tube as a detector. Data from 4.5 to 9 eV were acquired with the vuv ellipsometer described above. Data were obtained 4 compositions: 6, 11, 16, and 24 % TiO_2. Each of these compositions was measured in as-deposited and RTA forms, where the RTA was done for 90s at 500, 700, and 900 ºC.

3.5 Ga3d core-level reflectance data

The reflectance data analyzed for the properties of the Ga3d core-level transitions were obtained at the Stoughton synchrotron radiation facility Tantalus from about 1980 to 1982.[2] Reflectance was measured by recording the intensity of the light reflected reflected from the sample, then normalizing it by the current circulating in the storage ring. To enhance features in these spectra, second energy derivatives were calculating numerically using standard Savitzky-Golay methods.[3] Models were fit to these data by means of a standard nonlinear least-squares method using appropriate numerical techniques to obtain local minimizations with mean square deviations and variable statistics.

3.6 References

1. Characterization of Semiconductor s and Semiconductor Structures by Opitcal Techniques/Optical Properties of Material and Structures, D. E. Aspnes (1990)

2. S. M. Kelso, D. E. Aspnes, C. G. Olson, D. W. Lynch, and D. Finn, Phys. Rev. Lett. 45, 1032 (1980)

3. Savitzky, A.; Golay, M.J.E. (1964). "Smoothing and Differentiation of Data by Simplified Least Squares Procedures". Analytical Chemistry 36 (8): 1627–1639

4. TITANIUM SILICATE ALLOYS

4.1 XPS Ti $L_{2,3}$, Si $L_{2,3}$, O K_1 data presentation

Figure 4.1 presents Ti $L_{2,3}$ XPS data for a series of as-deposited Ti silicate alloys. As noted above, these data, and the subsequently shown XPS data, were taken on Ti silicate thin films in Professor Opila's laboratory at the University of Delaware, and were provided by Dr. L. Fleming. They represent the 2p core electron binding energies of the Ti $L_{2,3}$ edge for a set of Ti silicate alloys. The binding energy is defined as the difference in energy between the core level and the vacuum level. These transitions occur from a closed-shell initial state to a final state consisting of a core hole.

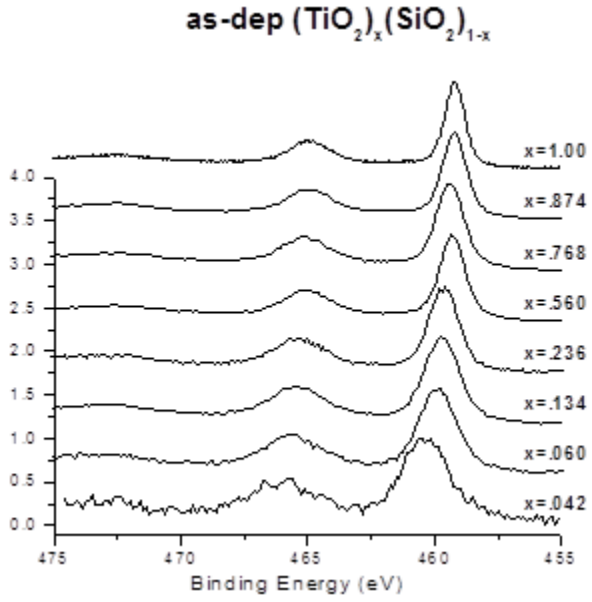

Figure 4.1 Ti $L_{2,3}$ XPS

Three features are associated with the J = 3/2 at and J = 1/2 levels at ~466 eV and ~460 eV, respectively, as well as a charge transfer multiplet at ~473 eV. The spin orbit splitting for the features between J=3/2 and J=1/2 is consistent with 2p spin orbit splitting for the Ti^{+4} ion. It is important to notice a general increase in binding energy from TiO_2 to the low concentration Ti-silicate alloys. Lowering of formal valence of a cation typically brings a lowering of binding energy. From this observation we can conclude that the Ti is nearly all in the form of Ti^{+4} ions.

Figure 4.2 shows the binding energies of the Si $L_{2,3}$ XPS edge for the same set of Ti silicate alloys. The single peak is actually a convolution of two peaks associated with the L_2 and L_3 transitions with a spin orbit splitting of approximately 0.6eV. The spin-orbit splitting cannot be resolved because it is less than the resolution of the instrument. The binding energy evolves from ~104 eV for SiO_2 to ~102 eV for samples with high Ti concentrations. The shift in binding energies of the Si $L_{2,3}$ peak is due to a change in bonding structure from 4 Si-O-Si bonds to an increasing concentration of Si-O-Ti bonds.

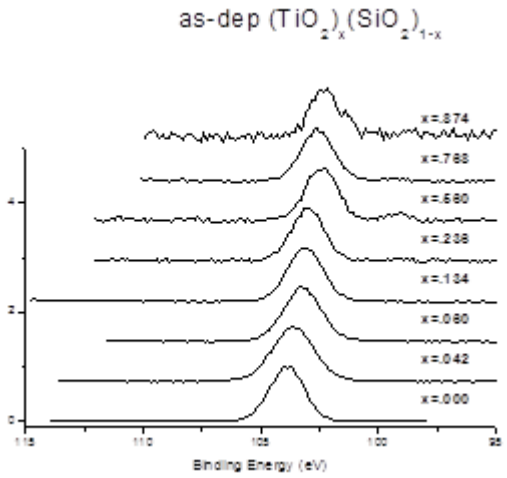

Figure 4.2 Si $L_{2,3}$ XPS

In Figure 4.3 the O K_1 edge XPS data are shown for the same Ti silicate thin films. These transitions are from O core levels in either 2- or 3-fold coordination with Si or Ti.

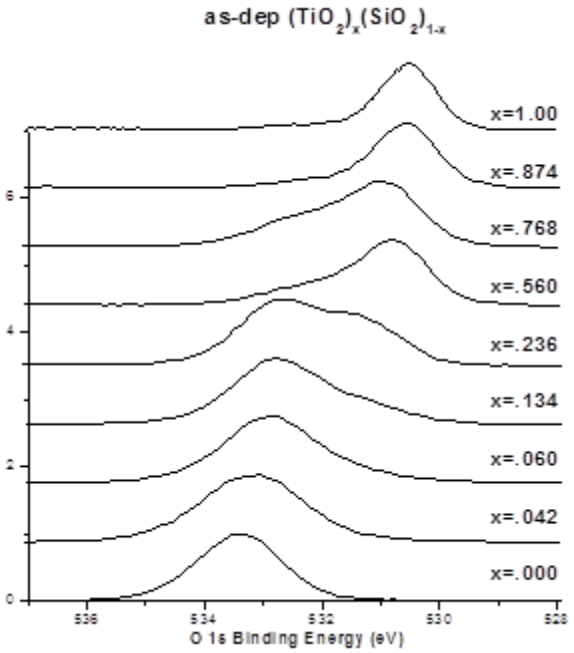

Figure 4.3 O K_1 edge XPS

4.2 XPS Ti $L_{2,3}$, Si $L_{2,3}$, O K_1 discussion

Figure 4.4 shows the binding energies of the Ti $L_{2,3}$ XPS edge for the same set of Ti silicate alloys. Binding energies were fitted as a single Gaussian with amplitude width and energy least squares fitted. A summary of the central energy is given in Table 4.1. The relative binding energy between TiO_2 and the low-concentration Ti silicate alloys is about 1.2 eV. There is a sharp decrease in binding energy from the lowest concentration of TiO_2 on up, with the binding energy basically leveling out at concentrations of 56% Ti and above. This is indicative of a relatively large conversion to the 6-fold environment at high Ti concentrations. For compositions at and below x=0.236 we observe a gradual increase in binding energy as we move down

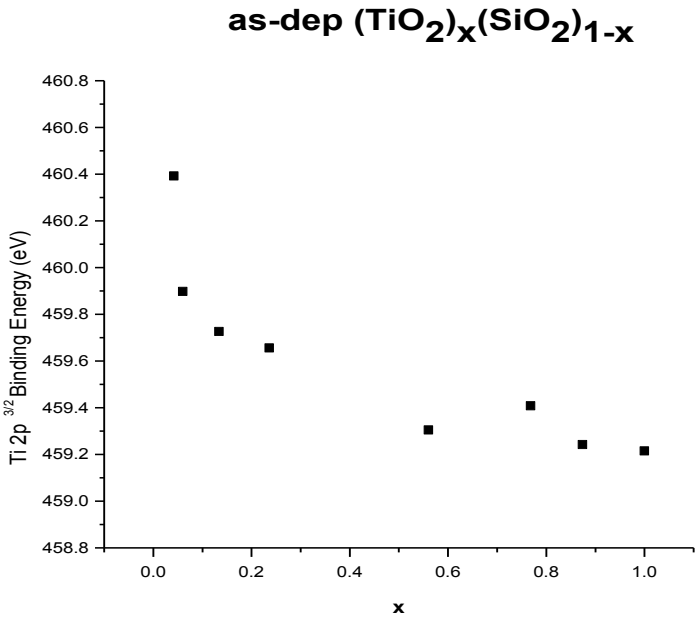

Figure 4.4 Ti $2p_{3/2}$ Binding Energy versus x

Table 4.1 Ti $L_{2,3}$ XPS Binding Energies

X	Ti $2p_{3/2}$ BE	+/- error
0.042	460.39163	0.01936
0.06	459.89752	0.01606
0.134	459.72663	0.01012
0.236	459.6552	0.01131
0.56	459.30469	0.00802
0.768	459.40849	0.01358
0.874	459.2415	0.01342
1.000	459.21443	0.00682

in alloy composition towards SiO_2, indicating a mixture of 4-fold and 6-fold coordination.

The binding energy of the cations in XPS spectra is dictated predominantly by the valence of the transition-metal cation. Smaller shifts can and do occur for changes in ligand structure, notably cation coordination number, bond length, type of ligand, and coordination about the ligands. For the Ti silicate system, we are primarily interested in the change in cation coordination from 6-fold octahedral to 4-fold tetrahedral. Difficulties in interpretation occur if the barium orthotitante data are used as an indicator for 4-fold coordination. This system shows a decrease in the binding energy of the Ti $L_{2,3}$ edge when compared to rutile or anatase. However, many papers, as well as the data presented here, demonstrate an increase in binding energy for the barium orthotitanate structure. Specifically, the XPS studies referenced were conducted on Ti silicalite (Ti- 1), an often-studied material in the catalysis field that contains 4-fold coordinated Ti cations.

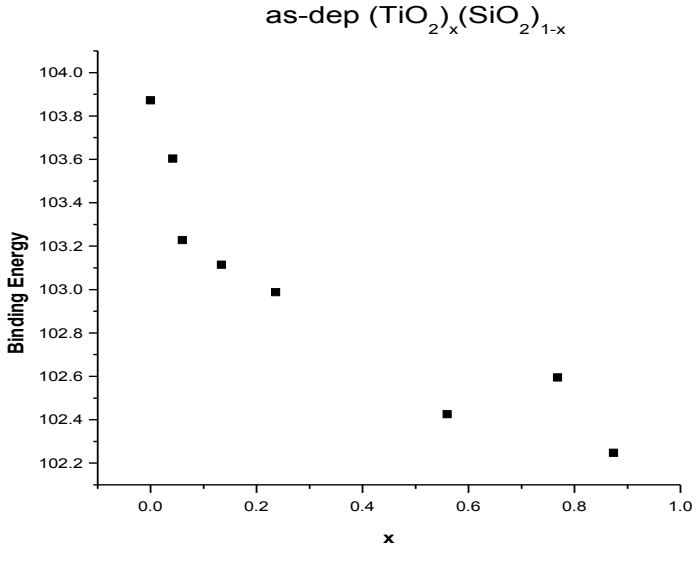

Figure 4.5 Si $L_{2,3}$ Binding Energy versus x

Figure 4.5 shows the binding energies of

the Si $L_{2,3}$ XPS edge for the same set of Ti silicate alloys. Binding energies were fitted as a single Gaussian with amplitude width and energy least squares fitted. A summary of the central energy is given in Table 4.2. The binding energy of the Si2p core level in the Si $L_{2,3}$ XPS spectra is about 1.6 eV higher in SiO_2 than in the alloys with a high Ti concentration. This may be due to the relative difference in absolute binding energy between the Si $L_{2,3}$ transition and the Ti $L_{2,3}$ transition, but may also be attributed to the fact that SiO_2 is less ionic than TiO_2. There is a sharp decrease in binding energy with alloys of greater Ti concentration with less of the leveling-out characteristic of the Ti $L_{2,3}$ binding energy. This may be less indicative of a formal conversion of the environment than a change of ligand types. That is, more types of local environments may be permissible for 4-fold-coordinated Si than for 4-fold-oordinated Ti.

Table 4.2 Si $L_{2,3}$ XPS Binding Energies

x	Si $L_{2,3}$ BE	+/- error
0	103.87157	0.00242
0.042	103.60375	0.00284
0.06	103.2279	0.00314
0.134	103.11399	0.00333
0.236	102.98794	0.00503
0.56	102.42575	0.00847
0.768	102.59416	0.00507
0.874	102.24736	0.02976

In Figure. 4.6 I compare the binding energy of the Ti $2p_{3/2}$ state with the average binding energy of the Si $L_{2,3}$ states. With increasing concentrations of Ti, the binding energies of both the Si 2p and Ti 2p core states decrease. The binding energies go down as the material approaches the more ionic TiO_2 environment. The

change in binding energies in the red points are the 4.2, 6.0, and 13.4% TiO_2 concentrations, and indicate a changing ligand environment of both 4-fold Ti and Si, as well as the introduction of Ti converted tp 6-fold coordination.

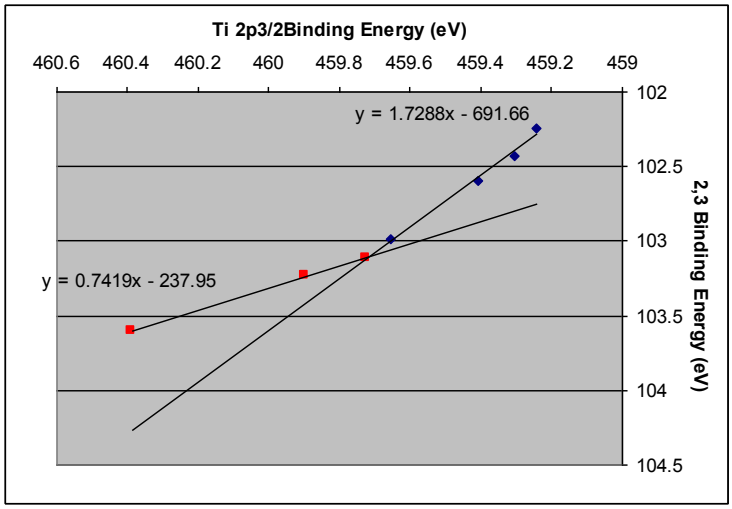

Figure 4.6 Comparison of Ti $2p_{3/2}$ binding energy with average binding energy of the $SiL_{2,3}$ states.

For the OK_1 XPS spectra binding energies were fitted as a single Gaussian with amplitude width and energy least squares fitted. A summary of the central energy is given in Table 4.4. The differences between the binding energies of O in the SiO_2 and TiO_2 cases are about 2.9 eV. This large difference is understood by the localization of the bonding-charge distribution about the oxygen. This reflects the

Table 4.3 O K_1 edge XPS Binding Energies

x	OK_1 BE1	error	OK_1 BE2	error
0	533.421	±0.0026		
0.042	533.1799	±0.00348		
0.06	532.8871	±0.00772	531.0165	±0.05742
0.134	532.7809	±0.01431	531.1381	±0.05119
0.236	532.6993	±0.01041	531.2016	±0.01358
0.56	531.9592	±0.07288	530.7362	±0.00773
0.768	532.097	±0.04456	530.8515	±0.0075
01.00	532.5251	±0.12585	530.5011	±0.00532

difference in ionicity between SiO_2 and TiO_2, which more greatly affects the oxygen binding energy than that of either Si or Ti.

4.3 XAS Ti $L_{2,3}$ (0-100% TiO_2) data

In this section I introduce the XAS Ti $L_{2,3}$ spectra for a series of Ti silicate alloys that focuses on changes that occur in the midrange of alloy compositions. As noted above, these and subsequent XAS data were acquired by the Lucovsky group at Stanford Synchrotron Radiation Laboratories (SSRL) at the Stanford Linear Accelerator Center (SLAC). These data are used to investigate the changes between 4-fold and 6-fold Ti coordination, possible distortions of 4-fold and 6-fold coordination, and phase segregation as we move through alloy composition.

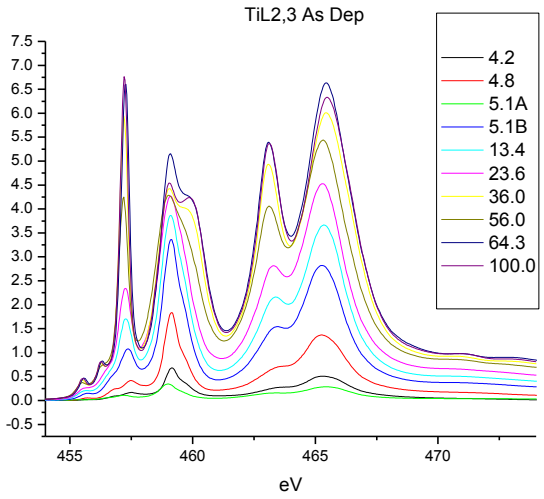

Figure 4.7 $TiL_{2,3}$ XAS (0-100% TiO_2) as-deposited

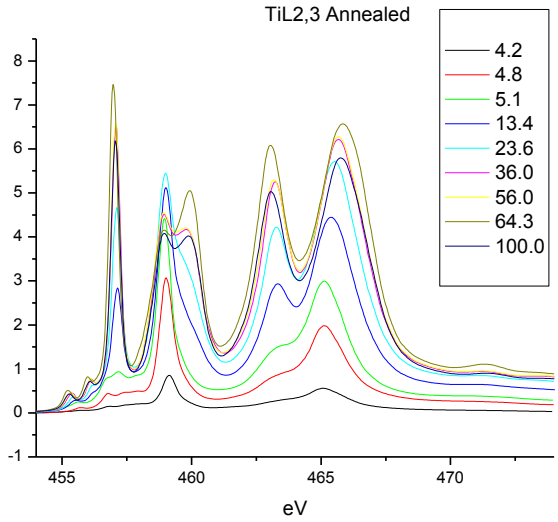

Figure 4.8 $TiL_{2,3}$ XAS (0-100% TiO_2) annealed

Figure 4.7 shows a set of $TiL_{2,3}$ XAS spectra for as-deposited samples with compositions from 4.2 to 100% Ti. It covers the energy range from 454 eV to

474 eV. These spectra are baselined, but otherwise present measured total electron yield (TEY) intensities. Figure 4.8 shows a similar set of $TiL_{2,3}$ XAS spectra for the same compositions, but for samples that are annealed.

Figure 4.9 singles out a representative Ti $L_{2,3}$ spectrum of a TiO_2 as-deposited thin film with 6-fold coordinated Ti sites. The five obvious relatively narrow lowest-energy features, designated L_3, are a manifold associated with the spin-3/2 2p hole. The next two fairly broad features at higher energy, designated Ti L_2, are associated with the spin-1/2 2p hole. Finally, there are two subtle features at 471.6 and 473.5 eV, which are due to transitions associated with charge-transfer effects.[3] This broad organization is maintained independent of composition and annealing. The separation of the L_2 and the L_3 manifolds is due to the spin-orbit coupling of the 2p core holes in the final states of the system.

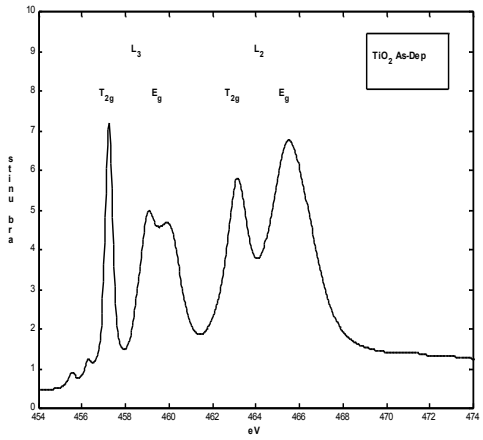

Figure 4.9 Ti $L_{2,3}$ spectrum of a TiO_2 as-deposited thin film with 6-fold Ti sites.

XAS spectra of transitions from the filled Ti $2p_{3/2}$ (L_3) valence orbital to the empty Ti 3d conduction orbital for samples both as-deposited and RTA at 900 ºC for 90 s are shown in Figure. 4.10. These present data for the Ti L_3 transition for both as-deposited (black) and annealed (red) TiO_2 for a series of compositions from 100% to 4.2% TiO_2. All data sets are presented in this series to facilitate direct

comparison among compositions, including those between 100 to 36% TiO_2. For this range of compositions we observe very little in the way of fundamental changes in the spectral lineshapes with annealing.

However, lineshape changes are quite evident in the composition range 36 to 4.2%. The overall lineshape changes significantly, and there is a substantial decrease in the intensity of the peaks about 457 eV and 460 eV. This general change occurs as a result of Ti changing from primarily 4-fold fold, in solution to primarily 6-fold phase segregated coordination through a mechanism, proposed by the author, of Ti-O-Ti bond formation which is energy minimized driven through the annealing process.

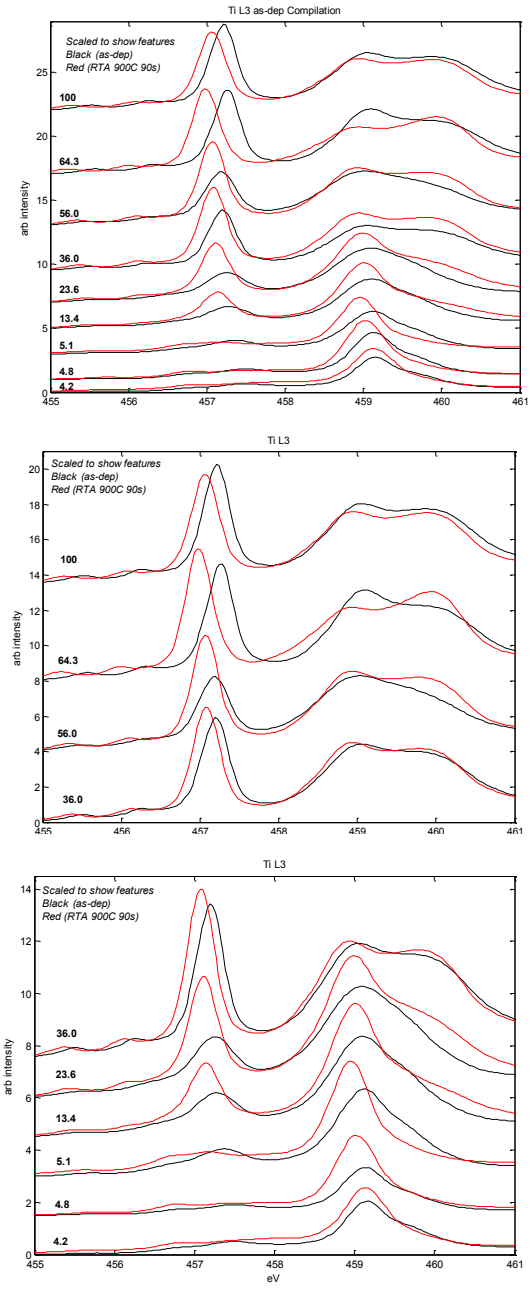

Figure 4.10 XAS Ti L_3 Spectra 4.2% to 100% TiO_2

4.4 XAS O K_1 (0-100% TiO_2) data

Figure 4.11 shows the OK_1 XAS spectra from 525 eV to 555 eV for all as-deposited samples. These spectra are normalized to their maximum values. Note a steady increase of the "pre-peak" transition-metal d-orbital features from 528 eV to 535 eV. We can also note that the basic SiO_2 structure is maintained for all compositions up to and including x = 0.236. For x = 0.360 and above, a dramatic shift occurs in the post-535eV range to those of TiO_2.

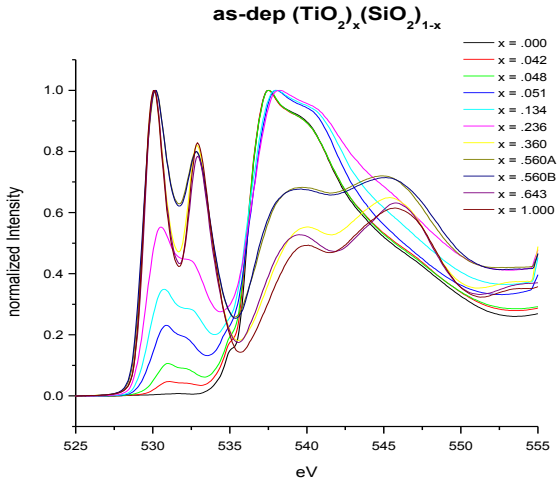

Figure 4.11 OK_1 XAS spectra for the as-dep samples

Figure 4.12 shows similar OK_1 XAS spectra for the annealed samples. Again, the steady increase of the "pre-peak" transition-metal d-orbital features in the 528 eV to 535 eV range is apparent. We again observe that the basic SiO_2 structure is maintained for all compositions up to and including x = 0.236. Beyond x = 0.360 a dramatic shift of structures to those resembling TiO_2.occurs again.

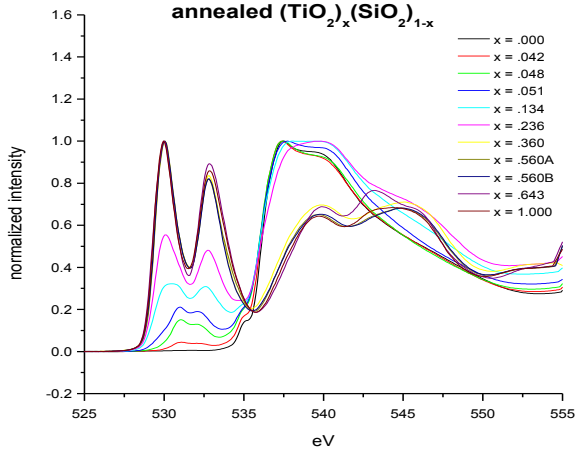

Figure 4.12 OK_1 XAS spectra for the annealed samples

4.5 XAS Ti $L_{2,3}$ (2-14% TiO_2) data

Here we consider XAS data for Ti silicate thin films deposited by RPE-MOCVD on Si(100) substrates both as-deposited at 300ºC and RTA-annealed at 900ºC for 90 s, as described earlier. In pseudobinary notation $(TiO_2)_x(SiO_2)_{1-x}$ compositions range from x = 0.02 to x = 0.14.

Figure 4.13 shows a normalized staggered plot of data for both as-deposited and annealed alloys.

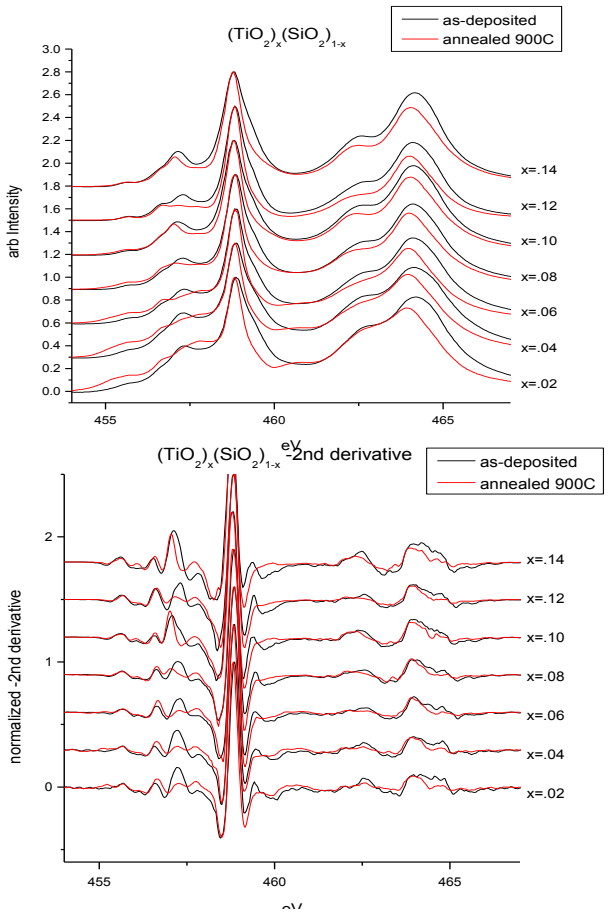

Figure 4.13 XAS Ti $L_{2,3}$ 2%-14% Ti (as-deposited and annealed 900˚C)

4.6 XAS O K_1 (2-14% TiO_2) data

Figure 4.14 presents a set of OK_1 XAS spectra for as-deposited samples for compositions from 2 to 14% for energies from 524 to 555 eV. These are again normalized to their highest values.

Figure 4.15 presents a set of

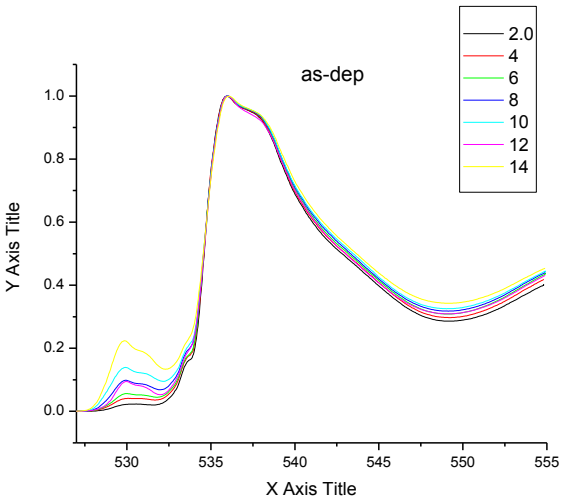

Figure 4.14 OK_1 as-dep XAS 2-14% TiO_2

OK_1 XAS spectra for the annealed samples for compositions from 2 to 14% for energies from 524 to 555 eV. These are again normalized to their highest values.

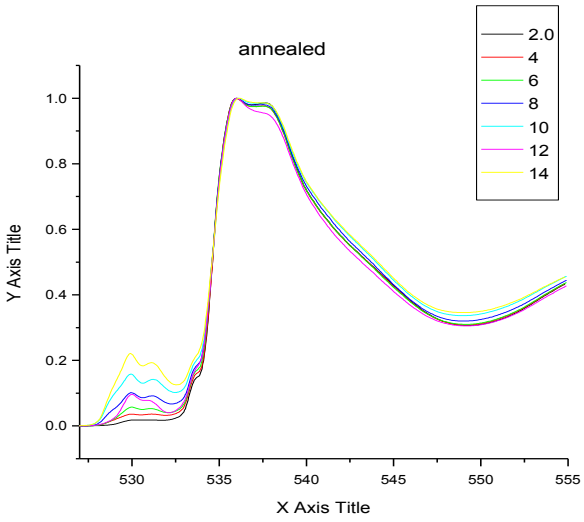

Figure 4.15 OK_1 Annealed XAS 2-14% TiO_2

4.7 Comments

To interpret these data It is essential to examine XAS data found in the literature that were taken on samples where the coordination is know through crystallographic measurements. By correlating features among these data, we can establish convincingly the Ti coordinations in our Ti silicate alloys.

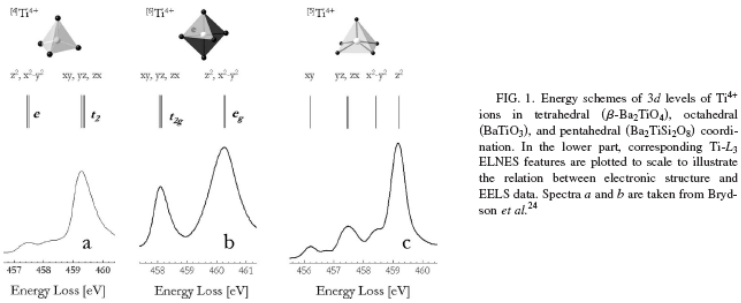

FIG. 1. Energy schemes of 3*d* levels of Ti^{4+} ions in tetrahedral (β-Ba_2TiO_4), octahedral ($BaTiO_3$), and pentahedral ($Ba_2TiSi_2O_8$) coordination. In the lower part, corresponding Ti-L_3 ELNES features are plotted to scale to illustrate the relation between electronic structure and EELS data. Spectra *a* and *b* are taken from Brydson *et al.*[24]

Figure 4.16 Ti $L_{2,3}$ edge spectra for 6-fold, 5-fold, and 4-fold materials (Hoche 2005)[1]

One of the most comprehensive analyses of Ti L_3 transitions was performed by Henderson, applying XANES to various series of Ti-silicate glasses.[1] They presented three spectra representative of 4-, 5-, and 6-fold coordination. These are

reproduced in the Figure. 4.17. The 6-fold-octahedral coordination data are from rutile, the 4-fold tetrahedral coordination data are from Ba_2TiO_4, and the 5-fold square-pyramidal data are from Fresnoite. The main differences among the different spectra result from the way that the ligand environments split the initial degeneracy of the electron d-orbitals of the p^5d^1 electron-hole final states.

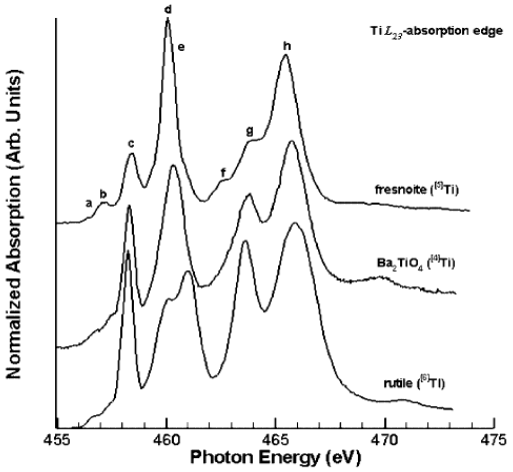

Fig. 2 Ti $L_{2,3}$-edge spectra for rutile (TiO_2), Ba_2TiO_4 ([4]Ti), and fresnoite ([5]Ti) ($Ba_2TiSi_2O_8$). The Ti coordination in each phase is indicated. *Labeling of peaks* corresponds to Fig. 1

Figure 4.17 Ti $L_{2,3}$ edge spectra for 6-fold, 5-fold, and 4-fold materials (Henderson 2002)[2]

Additional information on fourfold-coordinated first-row transition-metal ions is provided by a series of electron energy loss near-edge structure (ELNES) $L_{2,3}$ spectra on isoelectronic 4-fold coordinated closed-shell first row transition metal systems.[3] Figure 4.18 shows ELNES spectra for $KMnO_4$, $PbCrO_4$ $Pb_5(VO_4)_3Cl$ and Ba_2TiO_4. The fourfold-coordinated materials consistently show 2 major peaks, in contrast to 5- and 6-fold coordinated materials (cf. Figure. 4.17). The consistency of these spectra, which differ only in

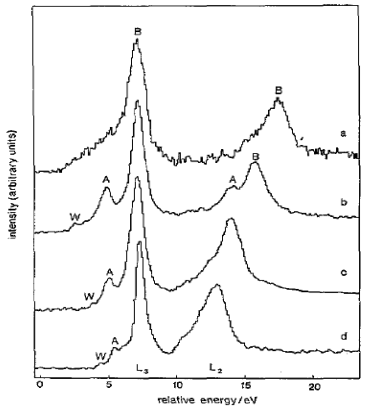

Figure 1. a, Mn $L_{2,3}$ ELNES of $KMnO_4$; b, Cr $L_{2,3}$ ELNES of $PbCrO_4$; c, V $L_{2,3}$ ELNES of $Pb_5(VO_4)_3Cl$; d, Ti $L_{2,3}$ ELNES of orthorhombic Ba_2TiO_4. The spectra are shown on a relative energy scale and have been aligned at peak B.

Figure 4.18 ELNES Ti $L_{2,3}$ spectra on isoelectronic 4-fold coordinated closed-shell first row transition metal systems. (from Brydson 1993)[3]

experimental resolution and spin-orbit splitting, allows one to confidently identify 4-, 5-, and 6-fold coordination.

4.8 XAS Ti L_3 spectra: discussion

We will be examining 2nd-derivative spectra though much of the following discussion because 2nd-derivative spectra strike a good balance between removing background white noise without sacrificing information about critical-point structures. This can be shown easily in reciprocal-space analysis. Data on as-deposited samples are nearly identical from 100% TiO_2 down to 36.0% TiO_2 as a result of Ti being 6-fold octahedrally coordinated. This assignment is made unambiguous by matching to the spectra presented above, where Ti is known to be in a 6-fold environment. Primary features occur at approximately 455.5, 456.2, 457.2, 458.5, 458.9, 459.7, and 460 eV. Consistent structural forms also occur at 455.7, 456.8, 457.5, 458, 459.2, and 459.8 eV in the 4.8% and 4.2% Ti alloys. These "extra" structures

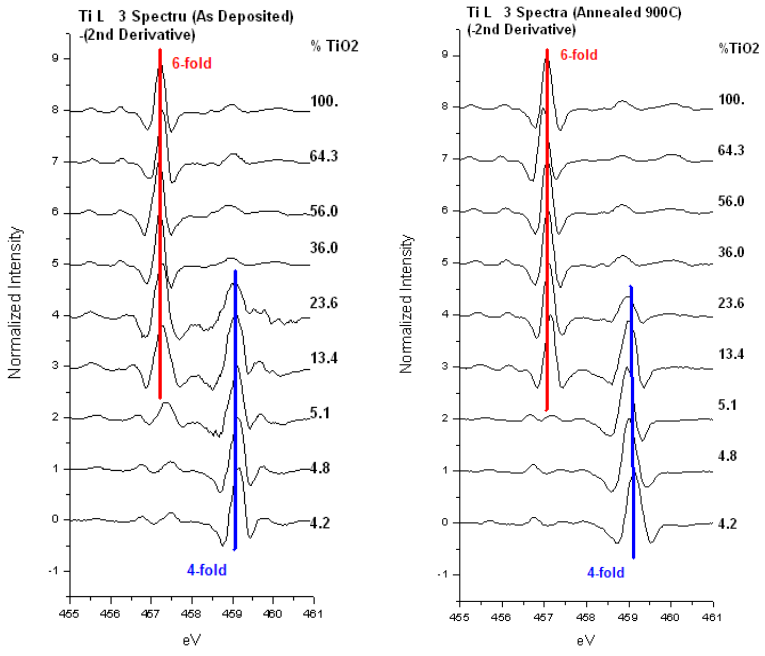

Figure 4.19 -2nd Derivative Spectra XAS $TiL_{2,3}$ highlighting prominent 4-fold and 6-fold feature

are consistent with the general critical-point features of rutile and anatase for high-Ti-concentration alloys.

Figure 4.19 shows -2nd Derivative Spectra of XAS Ti$L_{2,3}$, highlighting prominent 4-fold and 6-fold feature. By comparing these spectra to those where Ti is known to be 4-fold coordinated, we can also identify the presence of 4-fold-coordinated sites. Unlike the XAS data for the OK_1 edge, there is very little "movement" of the critical points. The stability of these Ti $L_{2,3}$ features is due to the fact that they are primarily influenced by the cubic crystal-field effects on the d-orbital pair. Also, as shown by comparing the spectra for rutile, anatase, and brookite, the different distortions primarily establish peak heights, that is, dipole-transition intensities, and not critical-point energies. A distinct feature at 459.8 eV appears at the onset of 4-fold-coordination (23.6%) and continues down to the lowest Ti percentages measured. However, as indicated below, there is no corresponding feature in the data of any of the annealed samples. The annealed data again consistently demonstrate 6-fold coordination from 100% TiO_2 to 36% TiO_2 and 4-fold coordination below, particularly with 4-fold coordination at the compositions 5.1%, 4.8%, and 4.2%. The 23.6% and especially, the 13.4% compositions show a mixture indicating the presence of 4-fold, anomalous, and 6-fold coordinations. However, due to the consistency of energies between as-deposited and annealed samples, it is probably not possible from these Ti L_3 data sets to distinguish between Ti incorporation as a continuous network or by phase segregation.

Figure 4.20 show Ti $L_{2,3}$ data at low concentrations of TiO_2. The lack of change in the 4-fold coordinated features is noticeable. In addition, the nearly complete attenuation, through annealing, of the feature at 459.5 eV is easily seen. This can be attributed to a distortion of the 6-fold coordination in an octahedral environment, or a change between distorted 4-fold tetrahedral symmetry sites.

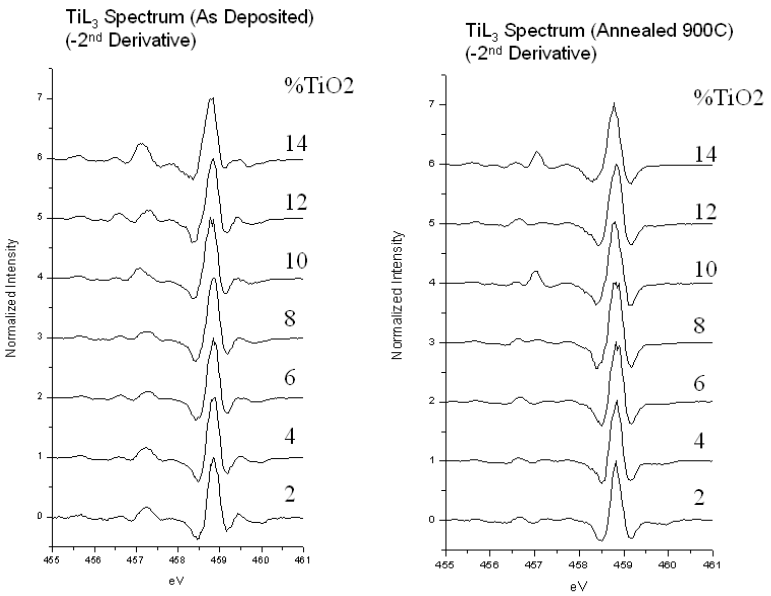

Figure 4.20 (-2nd Derivative) Ti $L_{2,3}$ data at low concentrations of TiO_2.

4.9 Compositional analysis of XAS spectra

Ti $L_{2,3}$ XAS data are available on Ti-silicate alloys of the following compositions: 100, 64.3, 56.0, 36, 23.6, 13.4, 5.1, 4.8, and 4.2% in both as-deposited and annealed forms. Our goal is to understand these data sets within the context of previous studies and the general physics of the

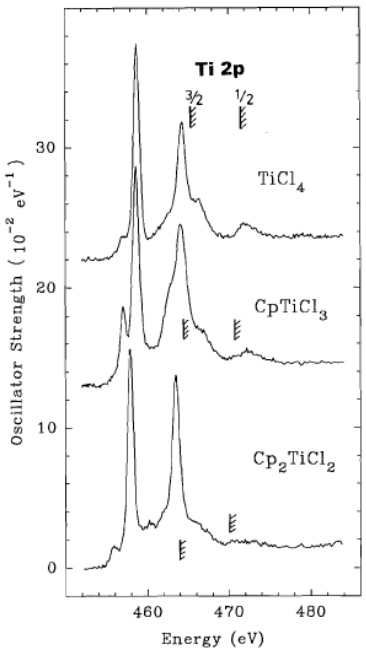

FIG. 5. Titanium 2*p* oscillator strength spectra of $TiCl_4$, $CpTiCl_3$, and Cp_2TiCl_2. The hatched lines indicated measured (45, 46, 48) or estimated Ti 2*p* IPs. See Fig. 2 for experimental details.

Figure 4.21: EELS spectra of $TiCl_4$ $CpTiCl_3$ and Cp_2TiCl_2[6]

annealing of amorphous solids. Specifically, we are interested in coordination conversion with cation distribution as well as phase segregation.

In Figure 4.21, I show EELS spectra of $TiCl_4$, $CpPCl_3$, and Cp_2TiCl_2 reported by Wen and Hitchcock.[6] Cp is short for cyclopentadienyl and identifies the attached metal complex that contains one or more ligands of $C_5H_5^-$. These three spectra represent different types of distortion of Ti in tetrahedrally coordinated compounds. The symmetry groups to which each of these compounds belongs are as follows. $TiCl_4$ maintains full T_d tetrahedral symmetry; $CpTiCl_3$ maintains C_{3v} symmetry appropriate for a 3-fold axis, i.e., a trigonally distorted tetrahedron; and Cp_2TiCl_2 maintains a

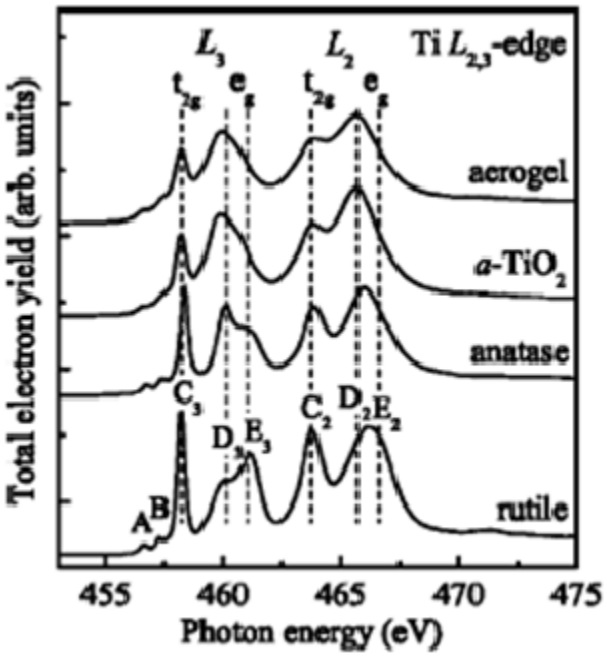

Figure 4.22 Titanium $L_{2,3}$-edge XANES specta of rutile, anatase used for reference as well as amporhpous TiO2 and titania aerogel[11]

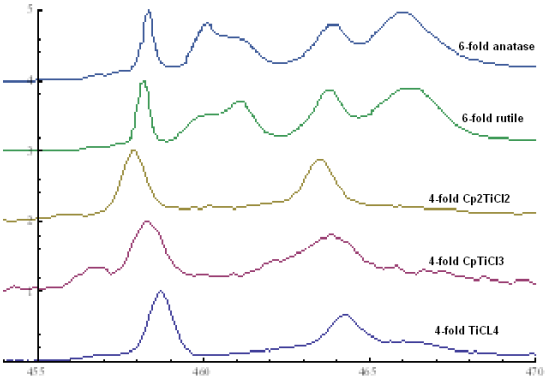

Figure 4.23 TiO_2 Reference spectra for fitting.[6,11]

cyclic rotational symmetry with a 2-fold axis, i.e., that of a tetragonally distorted tetrahedron. Ti maintains a +4 oxidation state in all three compounds. In Figure 4.22, I show Titanium $L_{2,3}$-edge XANES specta of rutile, anatase used for reference.

Using these reference spectra as a basis, I established coordination fractions by least-squares fitting the Ti L_3 data on as-deposited and 900 ºC annealed samples. Ti L_3 was fitted instead of the entire $TiL_{2,3}$ spectra because the L_2 maintains broadening due to decay effects. The functional form of the fit is $a_1*f[x-a_{01}] + a_2*f_2[_{x-a02}]$ etc., where a_1 and a_{01} pertain to $TiCl_4$; a_2 and a_{02} to $CpTiCl_3$; etc. The reference spectra themselves are shown in Figure. 4.23.[6,11] From bottom to top these are from 4-fold tetrahedral coordinated $TiCl_4$, $CpTiCl_3$, Cp_2TiCl_2, and 6-fold octahedral coordinated rutile and anatase, respectively. Each exhibits distinct features appropriate to the type of distortion.

We first obtain an overview of the general differences among the data with respect to composition. We can separate these compositions into three different categories. The complete similarity to literature spectra for crystallized TiO_2 of data on samples with a TiO_2 compositions equal to and greater than 36% TiO_2 indicates complete phase segregation. The TiO_2 inclusions are probably a mixture of anatase and rutile; the differences between anatase and rutile spectra not being large enough at the moment to allow them to be distinguished. However, we return to this point below. Next, spectra for the lowest TiO_2 compositions match the spectra for 4-fold coordinated materials. Finally, the data indicate that samples in the middle

composition range (5.1%, 13.4% and 23.6%) are mixtures of phases where Ti occurs both in 4-fold tetrahedral and 6-fold anatase/rutile forms.

4.10 Coordination structures from XAS spectra

Table 4.4: Coordination fractions for as-deposited and annealed 0-100% compositions.

% TiO_2	4-fold Td	4-fold C3v	4-fold C2v	6-fold rutile	6-fold anatase	ms error
100% as-deposited	0.041481	0.027828	8.62E-06	0.560803	0.369879	1.19016E-05
64.3% as-deposited	0.025503	0.113434	2.56E-08	0.454689	0.406373	2.16515E-05
56.0% as-deposited	0.108174	0.178339	6.97E-09	0.405666	0.307821	1.33927E-05
36.0% as-deposited	0.069764	0.043725	0.000472	0.527746	0.358294	8.10032E-06
23.6% as-deposited	0.263361	0.291822	0.006381	0.161484	0.276952	1.72903E-05
13.4% as-deposited	0.315645	0.282643	1.57E-05	0.091633	0.310063	2.51032E-05
5.1% as-deposited	0.445986	0.151304	0.035509	0.126313	0.240888	3.62208E-05
4.8% as-deposited	0.389953	0.275003	0.03067	0.12142	0.182954	4.05725E-05
4.2% as-deposited	0.45485	0.075011	0.218306	0.048141	0.203692	6.59415E-05
100% annealed	0.042006	7.94E-06	6.84E-06	0.697835	0.260145	1.03E-05
64.3% annealed	0.000391	3.6E-05	0.000183	0.8169	0.182491	1.74E-05
56.0% annealed	0.064213	4.41E-06	5.98E-06	0.629921	0.305856	1.17E-05
36.0% annealed	0.056763	4.48E-06	3.53E-05	0.5971	0.346097	1.33E-05
23.6% annealed	0.16315	0.020761	0.070156	0.395485	0.350448	1.2E-05
13.4% annealed	0.260294	0.010083	0.123337	0.240825	0.36546	2.42E-05
5.1% annealed	0.393715	0.177401	0.228958	4.79E-06	0.199922	0.000151
4.8% annealed	0.491008	0.001706	0.348448	1.27E-05	0.158825	0.000127
4.2% annealed	0.500164	0.134822	0.084456	0.10014	0.180418	0.000118

By least-squares fitting our model spectra to the data with volume fractions as the scaling parameters, we obtain general trend with which we will later be able to draw some conclusions and model with a stochastic method.

Figure 4.24 shows the relative concentrations of 4-fold Ti with T_d symmetry, 4-fold Ti with C_{3v} symmetry, anatase, and rutile phases in the annealed samples obtained using this approach and these are summarized and presented in Table 4.4. The plateau that occurs for both as-deposited and annealed samples for Ti

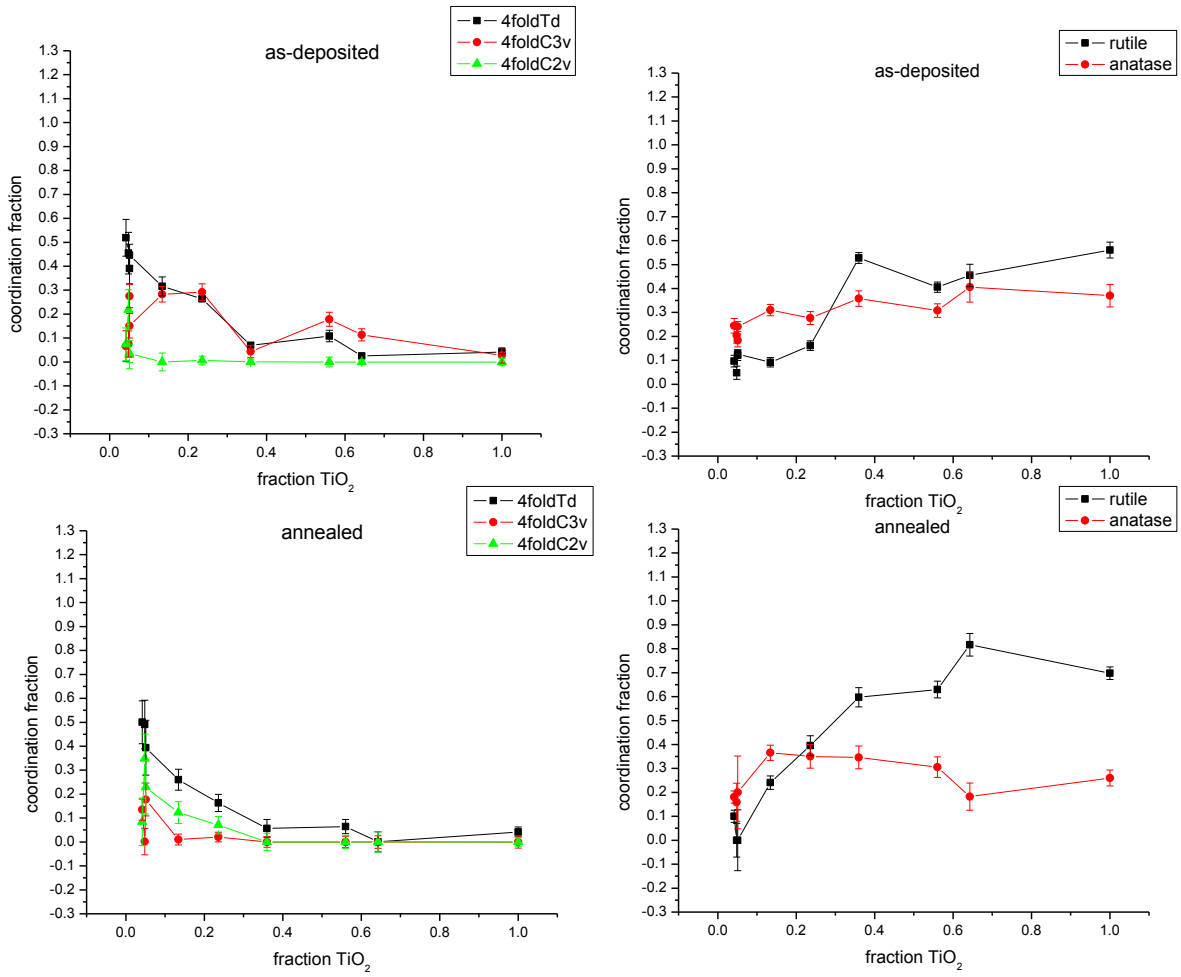

Figure 4.24 Coordination fraction versus fraction TiO_2

compositions greater than 36% Ti shows that for these compositions Ti is entirely in 6-fold coordination to the accuracy of the procedure. The results for the annealed-samples show a consistent shift towards the more energetically favorable 6-fold coordination at even lower concentrations.

4.11 Nearest-neighbor effects on Ti coordination

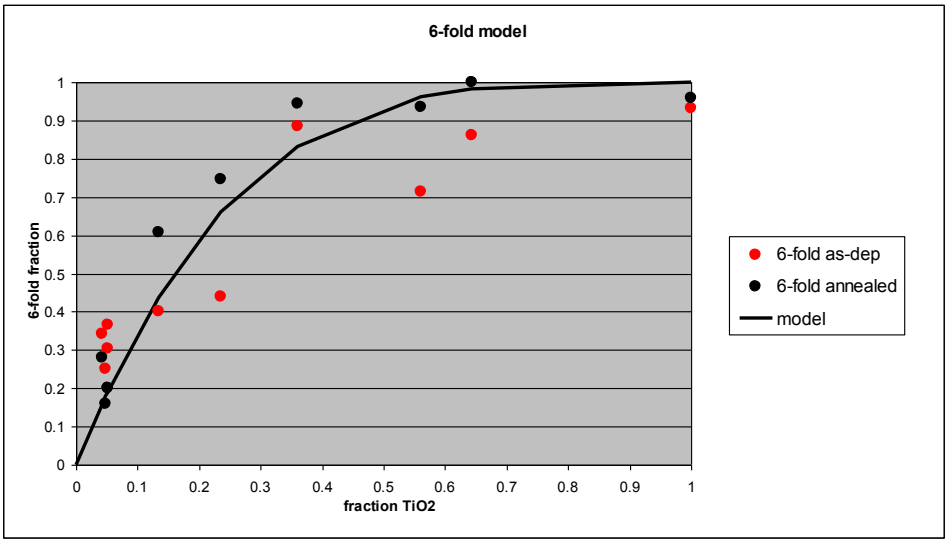

Figure 4.25 Comparison between 6-fold Extraction and Stochastic Model

To obtain some insight as to what is driving this change to 6-fold coordination, I consider a 4-site model about the Ti ion. Assuming that the sites are occupied randomly, I calculate the expected identity of the four nearest neighbors as a function of Ti composition. In this stochastic model, the probability of having one Ti-O-Ti combination is $1-(1-x)^4$, although the exact value of the exponent is less important than the fact that the concentrations follow a power law. This indicates that occupancy is indeed stochastic. Comparing this to the expected fraction of 6-fold composition, as shown in Figure 4.25, the results indicate that if any O-bridged

Ti-O-Ti groups form, there is a very strong likelihood the material becomes locally 6-fold coordinated.

4.12 Correlation of annealing-induced conversion of Ti coordination from 4- to 6-fold with the stochastic model

Literature reports and our analysis both show that when Ti is incorporated into SiO_2 in amounts of the order of 1 to 10%, the Ti is incorporated substitutionally in 4-fold-coordinated tetrahedral sites ordinarily occupied by Si. The Ti links to Si through 2-fold-coordinated O ligands. Our demonstration of coordination extraction, coupled with stochastic modeling, supports the idea that the formation of Ti-O-Ti bonds drives the change in Ti coordination. When the Ti concentration is sufficiently high, we would expect all Ti to be in 6-fold octahedral sites. Here, we critically test this idea.

To begin, we note that if Ti is surrounded by 4 nearest-neighbor Si cations it maintains its 4-fold coordination even when annealed to 900 ºC. However, if one of these 4 nearest neighbor cations happens to be Ti, these Ti transition to 6-fold coordination. The question is, why does this occur, or more important, what is so fundamental about two Ti atoms being nearest neighbors that result in a transition to 6-fold coordination above a certain temperature. One possible explanation lies with the atomic orbitals of the cations and their parity in their ground state.

Si maintains sp^3 hybridization in SiO_2. The combination of s orbital character, which has even parity, and p orbital character, which has odd parity, creates lobes that extend in the <111> directions, thereby allowing maximum separation of the

electrons of the system. Conversely, from a covalent standpoint, Ti has available only electrons in the 4s and 3d states, both of which maintain positive parity. Hybridizing them does not allow lobe extension of the wave functions. When two Ti cations share a common O, the O does not accommodate a spread electron density distribution so the configuration is unstable. Thereby, it changes its coordination. This is the simple qualitative explanation of why Ti goes from 4- to 6-fold coordination upon annealing.

Our analysis, so far, has been limited to the specifics of four-fold in solution to six-fold phase segregated conversion after annealing as a result of the presence of Ti-O-Ti bonds about a titanium site, and the suggestion that the presence of 2^{nd} order titanium atoms may drive 6-fold titanium in solution to 4-fold titanium in solution with respect to low concentrations of Titanium in the alloy series. These are specific local effects that depend on equilibration at annealing temperatures. Other effects, such as the percolation threshold at 16% critical volume in 3d lattices[10] may possibly have some value to understand the results we see; however, the stochastic method does appear to model the data rather effectively.

4.13 Phase segregation and striation in medium- to high-Ti-percentage alloys

As seen in Figure 4.26, comparing the XAS Ti $L_{2,3}$ data for TiO_2 compositions $\geq$36% annealed and 36% and 64% as-deposited, we observe only 6-fold coordinated Ti with narrow features associated with phase-segregated crystalline material. The fact that this is true for the 36% annealed sample may not be unexpected, but if one considers only composition for the as-deposited 36% sample,

this is surprising. Comparing the 36% as-deposited data to the 26.3% as-deposited data, as in Figure 4.27, this abrupt change is even more apparent. Also noteworthy is the near-complete similarity between the 36% as-deposited and annealed data, as well as the lack of any evidence of 4-fold coordination in the samples. This indicates a complete conversion to octahedral coordination.

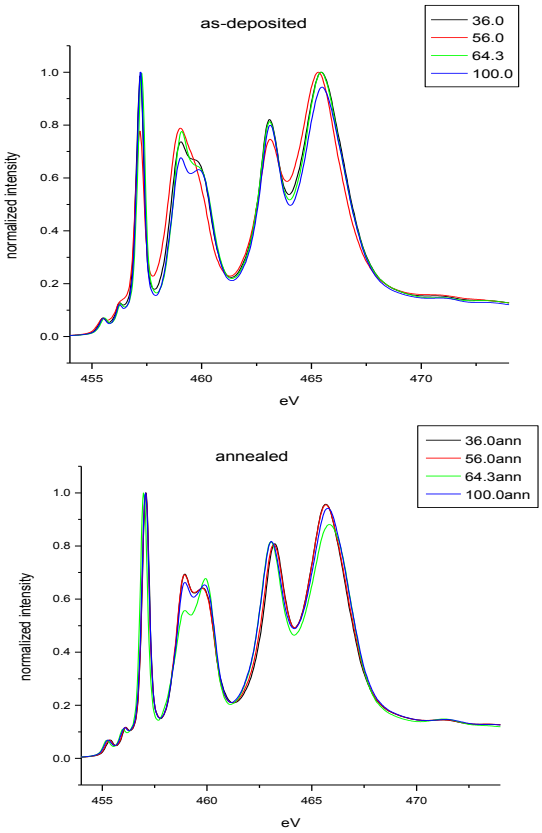

Figure 4.26 Ti $L_{2,3}$ As-deposited and annealed 36% to 100% TiO_2

To further understand this somewhat surprising situation, we turn to the XAS OK_1 data, showing in Figure 4.28. These are shown with the 23.6% results for comparison. What is also surprising is that the data for all annealed compositions for $x \geq 36\%$, as well as the 36% and 64.3% as-deposited, are nearly identical. They all appear to be transitions involving 3-fold

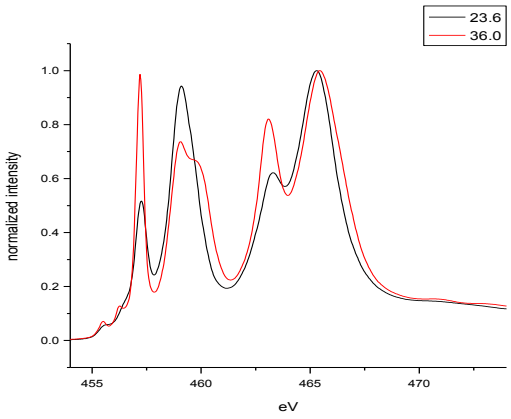

Figure 4.27 Comparison between as-deposited 23.6% and 36% TiO_2

coordinated O associated with TiO_2. The only differences we detect, as with the Ti $L_{2,3}$ data, are associated with transitions from one crystalline phase to another. The fact that we see no signal in the XAS OK_1 data associated with SiO_2 makes very little sense if we are thinking about these materials as being composed of phase-segregated TiO_2 nanoparticles embedded in an SiO_2 matrix, as we are for the annealed samples for x < 36%, which do phase segregate. This is even more unreasonable for the as-deposited samples, as we would expect to see no phase segregation of the TiO_2. The question then becomes, where is the SiO_2, recalling that for the 36% sample 64% of the material should be SiO_2.

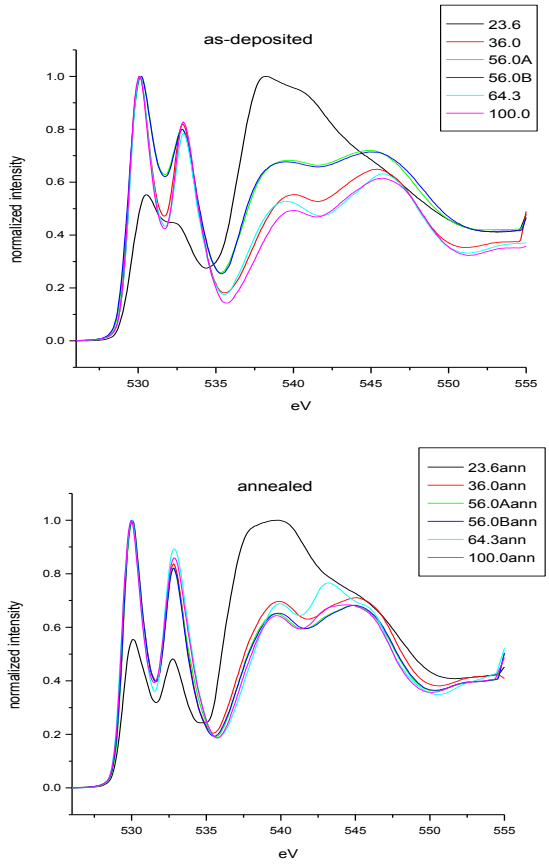

Figure 4.28 OK_1 As-deposited and annealed 23.6% to 100% TiO_2

The reason for this apparent lack of SiO_2 XAS OK_1 signal, and why we see phase-segregated TiO_2 in the 36% and 64.3% as-deposited samples can be understood in terms of a transformation of the configuration. At compositions between 23.6% and 36.0% the data show that the material converts to a striated configuration where all the TiO_2 is in the top layer of the system and all the SiO_2

below. This reorganization, coupled with the fact that XAS spectra acquired through total electron yield (TEY) spectroscopy, primarily a surface probe with a penetration depth on the order of a several nm[4], would explain why there is an almost complete lack of signal for O associated with SiO_2. However, the anomaly in the 56% as-deposited data set with respect to the 36% and 64.3% as-deposited sets should be noted. There is complete phase segregation and apparent striation in the annealed 56% TiO_2 samples. However, the 56% as-deposited sample shows some SiO_2 signal and may indicate an incomplete striation. It should be noted that the striations could also be angled relative to the surface. Evidence for these striations can also be found in the literature. Hodroj found striated structures in an annealed sample with an as-deposited overlayer thickness of 119.3 nm and a Ti concentration of 40%.[5] However, Hodroj presents an as-deposited sample with no striations. These results are represented in Figure 4.29.

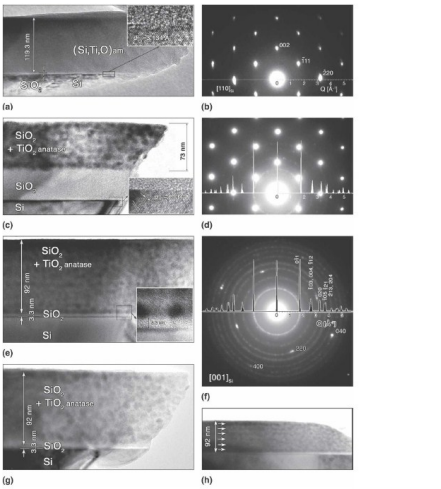

FIG. 3. Bright-field transmission electron micrographs and selected area diffraction patterns of a mixed TiO_2–SiO_2 film (A: atomic rat TiO_2:SiO_2 = 40/60) (a, b) as-deposited, (c, d) annealed for 1 h at 950 °C under air, (e, f) annealed for 1 h at 950 °C under argon, (g) anneal for 12 h at 950 °C under argon. The insets in (a), (c), and (e) correspond to high resolution images of the Si/film interface. A multilay microstructuring is shown in (h).

Figure 4.29 TiO_2-SiO_2 striations (Hodroj 2008)

Hodroj found striated structures in an annealed sample with an as-deposited overlayer thickness of 119.3 nm and a Ti concentration of 40%.[5] However, Hodroj presents an as-deposited sample with no striations. These results are represented in Figure 4.29.

The stocastic model describes relative concentrations of the coordination centers fairly accurately and provides motivation for coordination conversion, but it does not explain full conversion to phase segregation with annealing nor deviations from the stochastic model. For this, the best option is to look at additional effects

driven by percolation. In fact, percolation theory could explain a range of phase segregation at a critical threshold with annealing, while a stochastic model would not. We note that percolation theory gives the critical threshold at 16% critical volume in 3d lattices[10] while we see the critical threshold to be, at least above 23.6%.

4.14 Lineshape changes in XAS Ti $L_{2,3}$ spectra of low-percentage TiO_2 alloys with annealing

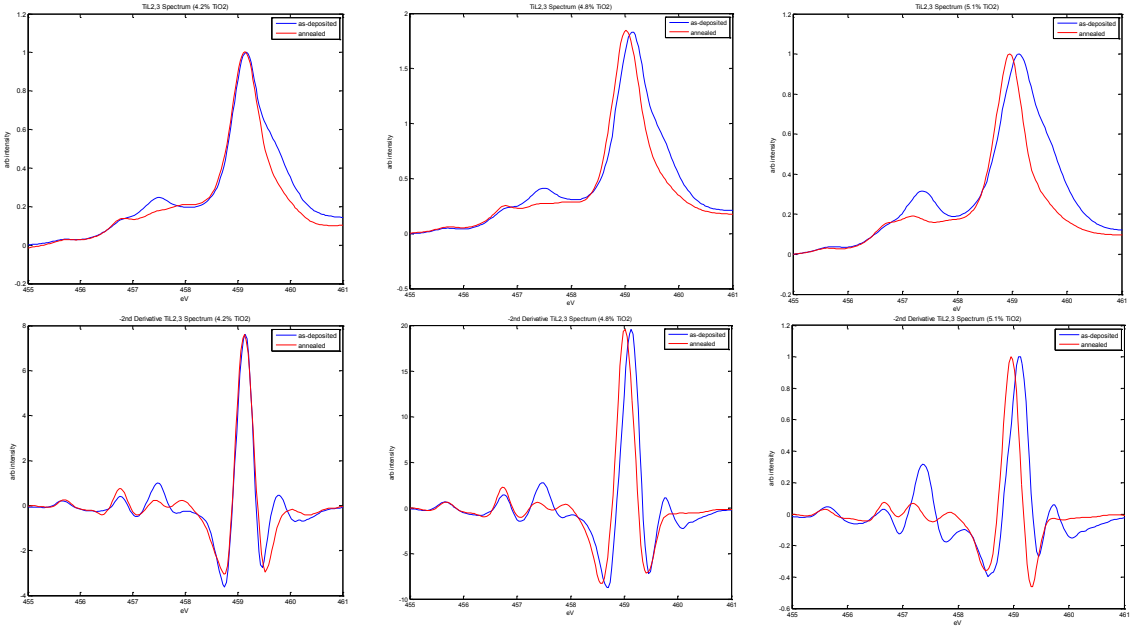

Figure 4.30 Aligned comparisons of Ti $L_{2,3}$ spectra taken on annealed and as-deposited 4.2%, 4.8%, and 5.1% Ti silicate alloys

Figure 4.30 shows aligned comparisons of Ti $L_{2,3}$ spectra taken on annealed and as-deposited 4.2, 4.8, and 5.1% Ti silicate alloys. The upper row shows the data with zero values aligned and the spectra normalized to the amplitude of the largest feature. The lower row gives the negative second derivatives of these data

with respect to energy. The reason for showing the second derivatives is that there are a large number of closely spaced features in these L_3 spectra, so it is nearly impossible to obtain a clear picture of the contributions or their evolution with annealing without resorting to some method of enhancing weak spectral features. In particular, this allows us to better extract the critical point energies associated with the spectra even if they are in relatively close proximity.

One of the first logical points to make is that at low Ti concentrations we expect little change upon annealing, and so we should observe little change in the XAS $TiL_{2,3}$ spectrum. In fact, we observe substantial changes. We interpret this as evidence for local distortions of 4-fold coordinated Ti. Later, in the 2 to 14% Ti series we shall look at reference materials to determine the actual distortions taking place. When examining these for both as-deposited and annealed samples, we illuminate the distortion that occurs within 4-fold coordination. The data show six separate features. What immediately emerges is the reduction of the ~457.5 and ~459.8 eV features with annealing. In contrast, the first and largest features do not change either their critical point energies or relative amplitudes, which indicates that this is not due to changes from 4- to 6-fold coordination.

Our goal is to establish this distortion in low-Ti silicates. We start by assuming that the Ti coordination is 4-fold tetrahedral. First, to facilitate our understanding of which features are correlated in the Ti $L_{2,3}$ spectra, we attempt to align the intensities of the negative second derivatives of the as-deposited and annealed 4.2% Ti alloys. By aligning the intensities, we see that the intensities are maintained for the three

features at approximately 455.7, 456.8, and 459.1 eV. In addition, we observe the relative increase of a feature at 457.9 eV, which is due to the reduction of intensity of a feature at 457.4 eV. Thus, as inferred by comparison of the direct intensity plots, there is no real reduction of intensity. To determine the actual distortions taking place we now consider the 2%-14% Ti series.

4.15 Verification of annealing-induced distortions of 4-fold Ti coordinations

Comparisons among XAS Ti $L_{2,3}$ spectra on as-deposited and annealed samples of low Ti concentrations demonstrate significant changes in features. Specifically, there is a clear reduction of the two features at 457.5 and 459.7eV. We see this reduction in the second-derivative data as well as in the aligned data themselves.

The results are shown in Figure. 4.31 as as-deposited and annealed pairings and compares 4- and 6-fold amplitudes from the given references. Figure 4.32 shows the total 6-fold coordination.

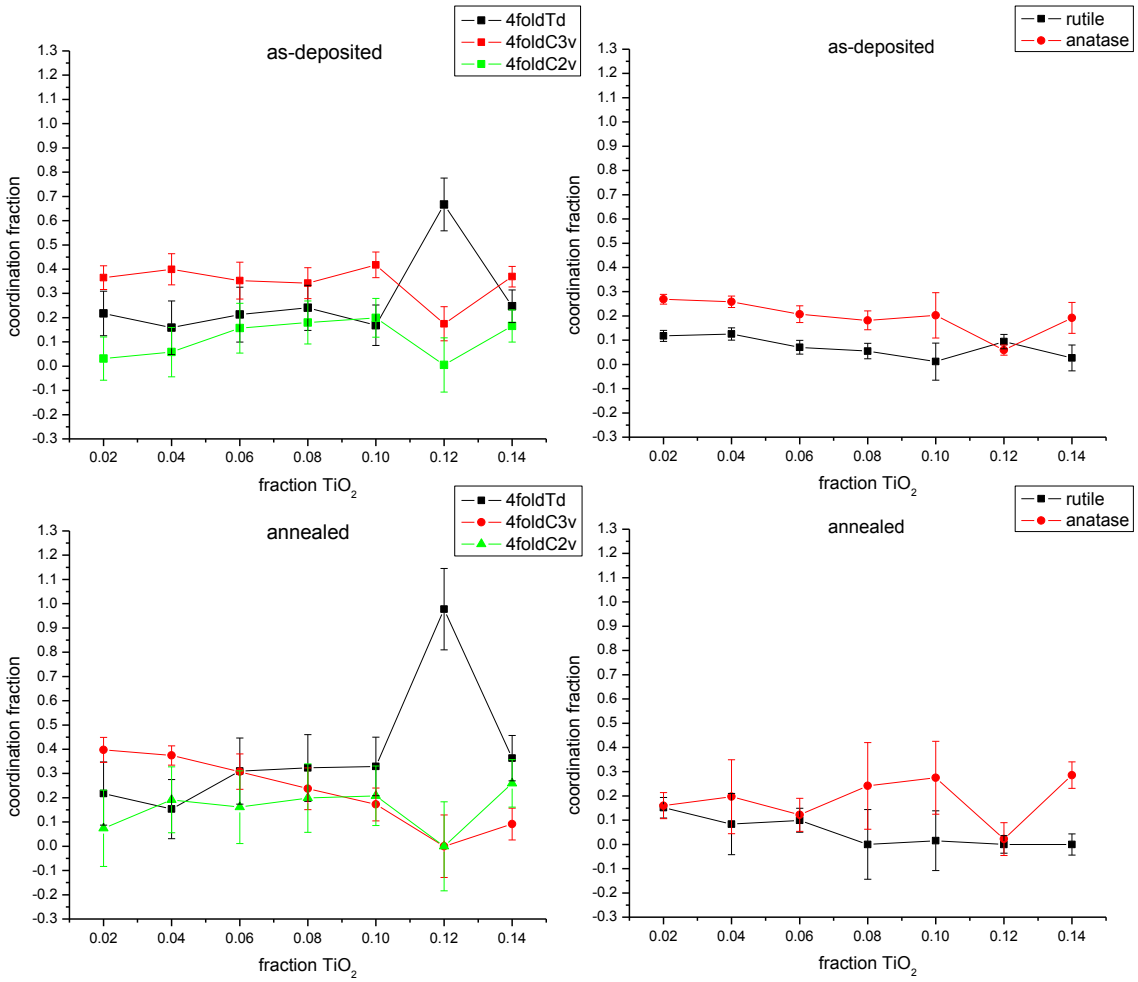

Figure 4.31 Comparison of 4-fold and 6-fold reference amplitudes.

In general we see that annealing shifts structure composition towards the more energetically favorable coordination. The results are generally well outside the estimated uncertainties as shown by the error bars. Also we see that the determined rutile or anatase fractions are well under the 4-fold coordination centers. This is probably consistent with the fact that the chance of second-nearest-neighbor Ti cations is low, referring back to our stochastic calculation. The dominate 4-fold constituent, in as deposited samples, appears to be $CpTiCl_3$ indicating predominant

4-fold coordination with trigonal distortion. There is movement towards 4-fold tetrahedral symmetry with annealing. There is an interesting crossover at about 8% Ti for decreasing-to-increasing 6-fold coordination due to annealing. We attribute this property change to the presence, or lack thereof, of 6-fold in solution coordinated Ti in the material that is sensitive to second nearest- neighbor Ti cations.

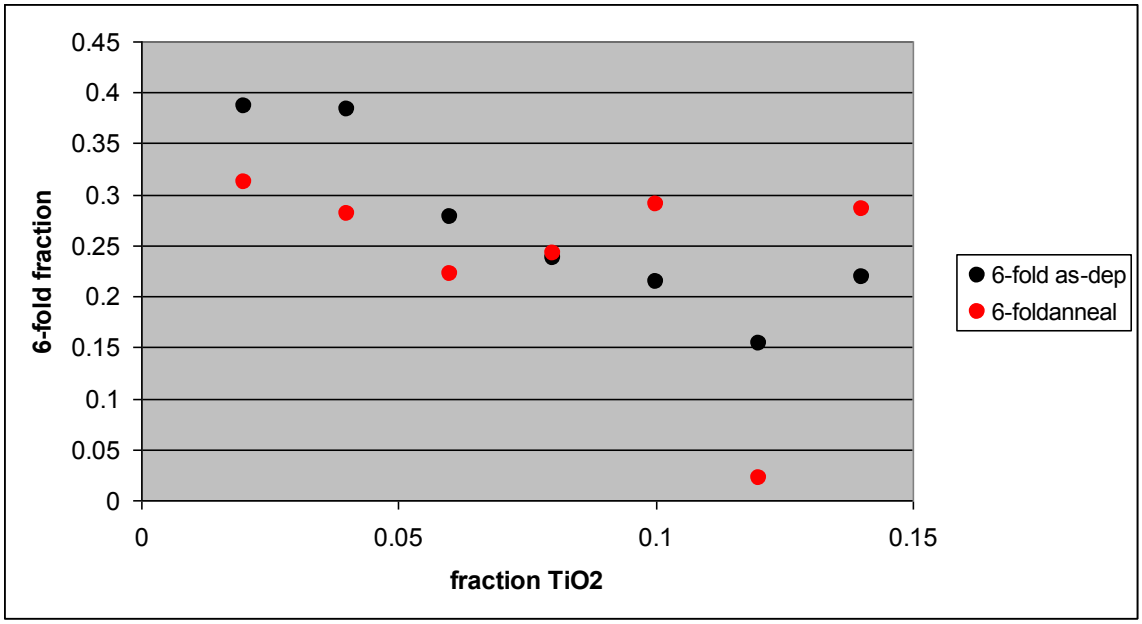

Figure 4.32 Comparison of 6-fold fraction in as-dep and annealed
This concentration goes down precipitously with increased Ti concentration.

4.16 XAS Ti $L_{2,3}$ multiplet calculations

In this section, we critically assess assignments by comparing the XAS Ti $L_{2,3}$ data to the results of multiplet calculations done in an LS basis set. The point is to gain additional insight by capitalizing on oscillator strengths, using the fact that the only dipole-allowed transition is $^1S_0$ to $^1P_1$, which propagates through different combinations of initial and final states. For these calculations I use Cowan's program

with crystal-field transformations by Thole, which is interfaced through the charge transfer multiplet program of de Groot. The program includes Butler's point-group symmetry methods for ligand/crystal field multiplet calculations by Thole and the base atomic-multiplet code of Cowan. Crystal-field potentials and Slater integrals are changed systematically to show how lineshapes are affected and degeneracies are broken with the different parameters. A negative crystal field potential indicates tetrahedral crystal-field symmetry, while a positive crystal-field potential indicates octahedral symmetry. These potentials, and their associated negative or positive signs, follow from single-electron calculations for d-orbital degeneracy splitting. The code not only calculates ground-state orbitals and energies, but also dipole moments between transition orbitals. The underlying theory can be found in texts on crystal-field theory.[7]

Specifically, the Ti silicate system involves transitions about the Ti^{+4} cation from a closed shell $2p^6 3d^0\ ^1S_0$ state to a series of $2p^5 3d^1$ final states. The direct and exchange Coulomb effects are included with Hartree-Fock values of F^2 = 5.042 eV, G^1 = 3.702 eV, and G^3 = 2.106 eV and the Slater integrals are reduced by factors indicated in the calculations. We include a spin-orbit splitting of 3.78 eV for the 2p hole, and a very small electron spin-orbit splitting of 0.032 eV. The cubic crystal field splitting values are given in the indicated calculations.

Figure 4.33 shows the result for a spherically symmetric Ti^{4+} ion with the Slater integrals set at 60% of their calculated values and no spin-orbit effects included. When Ti $L_{2,3}$ excitations of transition-metal compounds are modeled, it is well known that the Slater integrals must be reduced to achieve a good fit to data. I verified this with $SrTiO_3$, where the Ti is octahedrally coordinated. I also examined Ba_2TiO_4, where Ti is tetrahedrally coordinated. Both calculations show the need for a significant reduction of the Slater integrals of the tetrahedrally coordinated compound relative to the octahedrally coordinated compound. This is necessary to obtain the correct XAS line shapes for our materials.

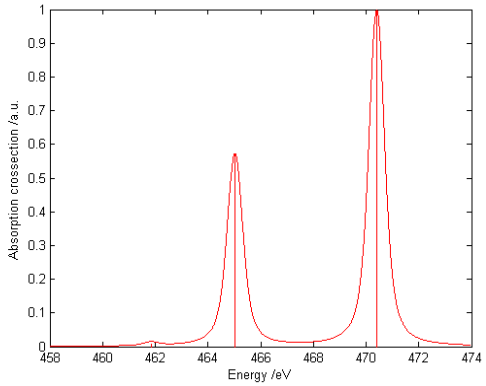

Figure 4.33 Ti^{4+} spherically symmetry, full 2p 3d splitting, slater integral 60% of normal

Figure 4.34 shows the result of adding an octahedral crystal field splitting of 1.8eV. The traditional L_3 and L_2 mainfolds are beginning to be formed.

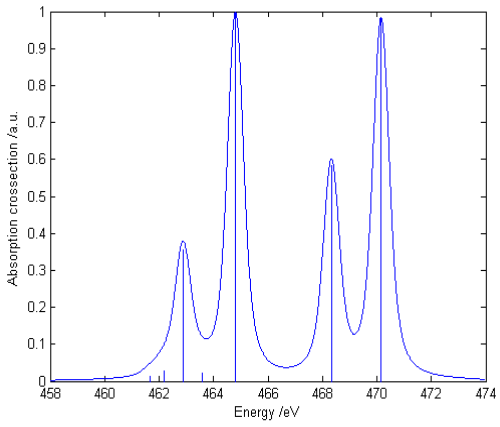

Figure 4.34 Ti^{4+} octahedral symmetry with a crystal field splitting of 1.8 eV, full 2p 3d splitting, slater integral 60% of normal

Figure 4.35 shows the result of adding a cubic crystal field splitting -1.8eV, indicative of a tetrahedral ligand environment. We can clearly see a reduction of the low energy levels, by about a factor of two, with respect to both the L_3 and L_2 manifolds. This overall moment reduction is clearly evident in comparisons of 4-fold and 6-fold titanium compounds as well as our titanium silicate alloy series.

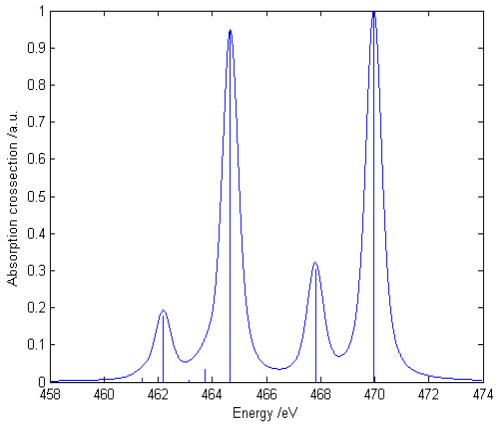

Figure 4.35 Ti^{4+} Oh symmetry with a crystal field splitting of -1.8 eV full 2p 3d splitting, slater integral 60% of normal

Figure 4.36 shows the result of a set of calculations where the crystal field potential 10Dq is changed from -2.0 to 2.0 eV by steps of 0.2 eV. These calculations were performed with Slater Integrals set at 60% with full 2p and 3d spin orbit effects. Note the strong anti-crossing phenomena in the second, third, and fourth highest-energy transitions. Even when the crystal field is zero there is significant splitting of the energy-level structure. With the present spin-orbit splitting of the p-hole and the direct and exchange effects, the crystal field perturbation affects more as a general inclusion of

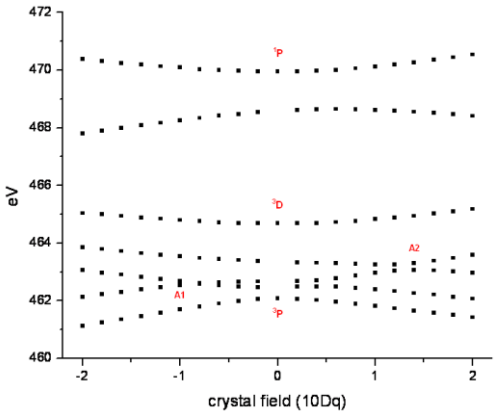

Figure 4.36 Crystal Field Calculations

dipole allowed transition moment intensities in typically forbidden transtions than actual splitting of particular degeneracies.

Figure 4.37 shows the results of two multiplet calculations for Ti $L_{2,3}$ XAS spectra. Both are performed with a crystal field potential of 2.0 eV and full inclusion of 2p and 3d spin-orbit effects.

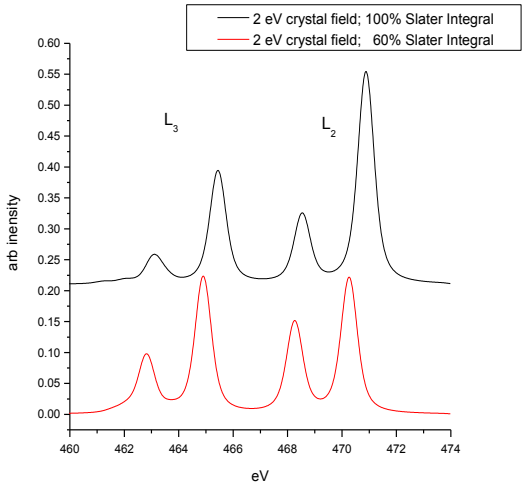

Figure 4.37 Multiplet calculations for Ti $L_{2,3}$ XAS spectra

However, the upper plot is created with the full Slater Integral while the bottom is created with the Slater Integral reduced by 40%. The lower spectrum clearly gives a better representation of the four strongest peaks of the $SrTiO_3$ XAS data. For reference, we note the near equality in peak heights of the higher-lying features in the L_2 and L_3 ranges in both the $SrTiO_3$ data and in the simulation done with the Slater-Integral contribution reduced by 40%. The XAS $TiL_{2,3}$ spectrum of $SrTiO_3$ is shown in Fig. 4.38.[8] Significantly, the two peaks labels E_g have similar

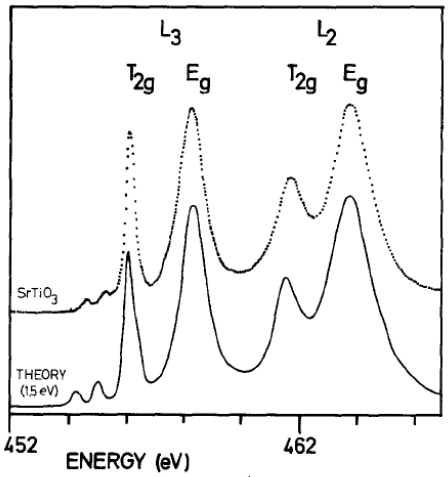

Fig. 1. 2*p* X-ray absorption spectrum of $SrTiO_3$ taken with the SX700(II) monochromator, compared with the theoretical atomic multiplet calculation (*bottom*) and the cubic crystal field calculation with a strength (10 Dq) of 1.5 eV

Figure 4.38 XAS $TiL_{2,3}$ spectrum of $SrTiO_3$

amplitudes. In particular, while the L_2 peaks are nominally broader due to Auger effects, the widths of the high energy features for the L_3 and L_2 sets are similar.

We consider in Figure 4.39 the comparison of the formal valences of Ti +4, Ti +3, and Ti+2 with staggered octahedral crystal fields of 2, (4/5)*2, and (3/5)*2 to approximate the effect of missing ligands. The spectra may be mistaken for 4-fold coordination, but XPS data reveal a Ti 2p binding energy that increases at low concentrations of Ti, as noted earlier. These data are inconsistent with decreasing formal valence.

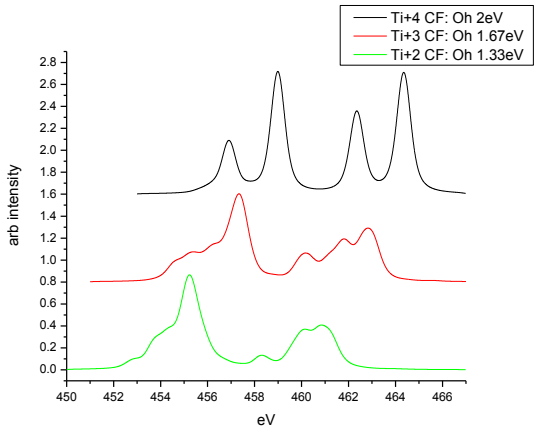

Figure 4.39 Ti Formal Valence Comparison

Next, we consider representative ELNES data for which the spectral line shapes are very similar to those seen in XAS. Figure 4.40 displays ELNES spectra of a number of compounds where one of the metal ions is tetrahedrally coordinated,[2] specifically the Ba_2TiO_4 spectrum at the bottom. All exhibit very similar line shapes, differing only in crystal-

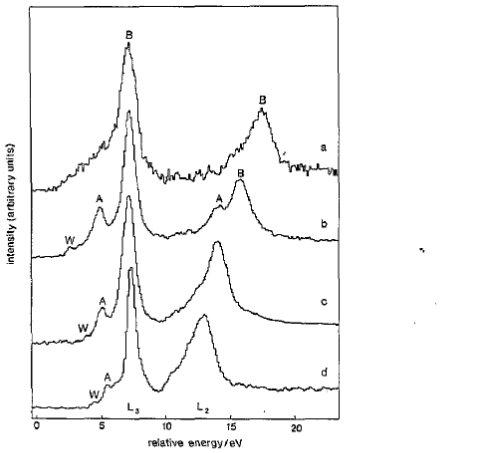

Figure 1. a, Mn $L_{2,3}$ ELNES of $KMnO_4$; b, Cr $L_{2,3}$ ELNES of $PbCrO_4$; c, V $L_{2,3}$ ELNES of $Pb_5(VO_4)_3Cl$; d, Ti $L_{2,3}$ ELNES of orthorhombic Ba_2TiO_4. The spectra are shown on a relative energy scale and have been aligned at peak B.

Figure 4.40 ELENS of 4-fold coordinated compounds.

field potentials and the 2p spin-orbit splitting. Particularly, the highest energy features of the L_2 and L_3 data exhibit an intensity ratio of about 2/3.

Figure 4.41 presents multiplet spectra calculated with a crystal field potential of the somewhat lower value of −0.889 eV, but with the same full inclusion of 2p and 3d spin-orbit effects. The topmost spectrum was calculated with the full Slater Integral, the intermediate with the Slater Integral reduced by 40%, and the bottom with a reduction of 60%. Thus, the crystal-field and Slater-integral parameters interact with the appropriate combinations to yield quality representations of the XAS spectra of $SrTiO_3$ and $BaTiO_4$.

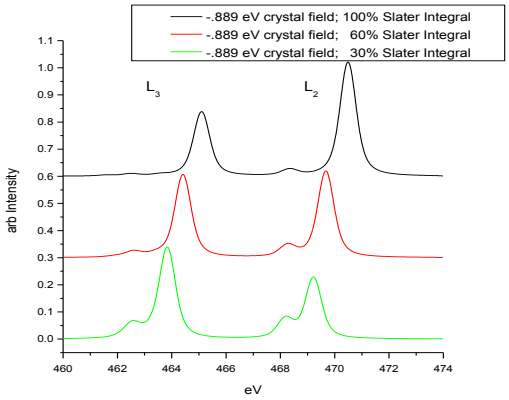

Figure 4.41 Multiplet spectra calculated with a crystal field potential.

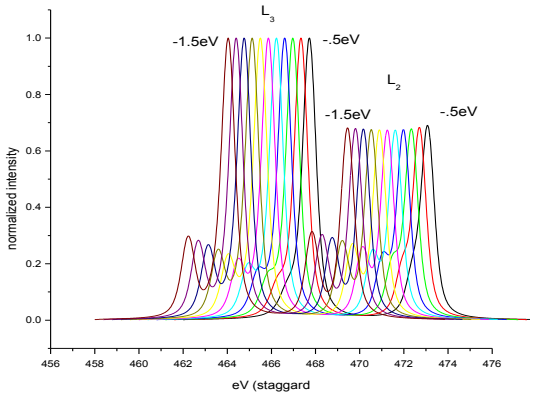

Figure 4.42 Staggered multiplet calculations for crystal-field potentials from -0.5 to -1.5 eV

To further isolate the effects of the crystal-field parameter on the relative intensities of the higher-lying features of the L_2 and L_3 sets, Fig. 4.42 presents a set of staggered multiplet calculations for crystal-field potentials from −0.5 to −1.5 eV in intervals of 0.1 eV. It is significant that the

intensities of the highest peaks of the L_3 and L_2 sets do not depend on the crystal-field potential.

4.17 Analysis of XAS O K_1 spectra

In this section we analyze the OK_1 XAS spectra, i.e., spectra of transitions from the O 1s core orbital to empty conduction orbitals for samples as-deposited and RTA at 900ºC for 90s. Numerically calculated second derivatives of the OK_1 edge XAS data for the complete sample set are shown in Fig. 4.44 for both as-deposited and annealed material. We focus on the edge features below 534 eV, which are indicative of O p character coupled with the Ti 3d orbitals. We are interested in what the data indicate about the Ti coordination for Ti concentrations greater than 36%. We already understand that at low Ti concentrations there are several types of distorted 4-fold coordinated sites. Both structures are basically maintained from 100% to about 36% TiO_2. This indicates that no coordination change occurs in these regimes that can be detected by OK_1 XAS measurements.

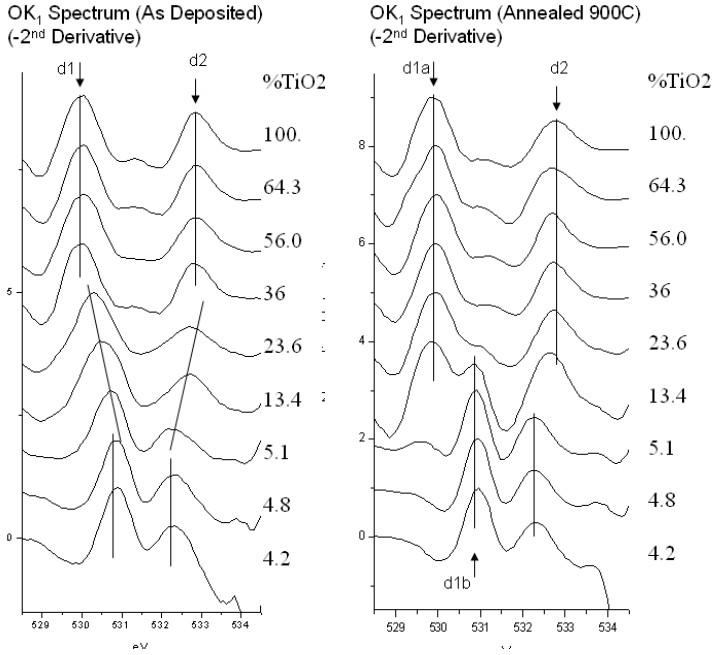

Figure 4.43 Numerically calculated second derivatives of the OK_1 edge XAS data

For the as-deposited samples we observe a change in the first peak from a position at ~530 eV for the 6-fold coordinated material to a peak at ~531 eV for anomalous coordination through a continuous transition region. From 100% to 36% TiO_2, we observe virtually no structural change. However, in the 23.6% and 13.4% range the first peak at ~530 eV gives a definite indication of a transition region. Later in this study, we will show how this demonstrates a transformation between 4- and 6-fold Ti driven by Ti-O-Ti bonding, as shown by the middle feature at 530.5 eV and discussed previously. Finally, the 5.1, 4.8, and 4.2% samples are all nearly the same, indicating that their electronic structures are similar. This is consistent with structural changes in the $TiL_{2,3}$ data owing to effects other than the presence of Ti-O-Ti bonds, which would not be revealed in such low concentrations.

For the annealed samples no such gradual change is apparent. Instead, there are two distinct peaks at ~530 eV and ~531 eV in the same transition region. For samples with compositions from 100% and 36.0% TiO_2 we again observe virtually no

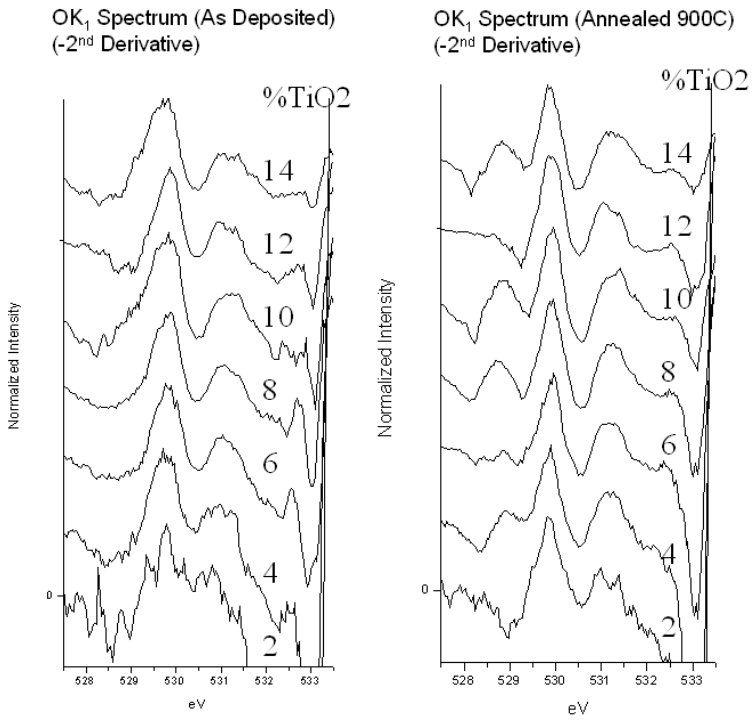

Figure 4.44 -2nd derivatives of the OK_1 edge XAS data

structural change. At 23.6% TiO_2 there is the slightest hint of a unique structure, indicating 4-fold material. For 13.4% TiO_2, we see peak strengths that appear to indicate substantial amounts of both compositions of TiO_2 (both 6-fold and anomalous) with both being completely phase segregated. At 5.1% TiO_2 we observe a slight off shifted "6-fold" peak, while at 4.8% and 4.2% TiO_2 we observe structures consistent with Si-O-Si bonds about 4-fold coordinated systems.

Figure 4.44 shows numerically calculated -2nd derivatives of the OK_1 edge XAS data for the samples from 2 to 14% Ti. Again, and in agreement with the 6-$TiL_{2,3}$ data, we observe features that are independent of composition and associated with 4-fold-coordinated Ti. In these transitions we observe a feature at about 528.7 eV that indicates the presence of 6-fold coordinated material in the annealed samples. This is not necessarily consistent along the alloy series, which may be due to uncertainty in alloy compositions.

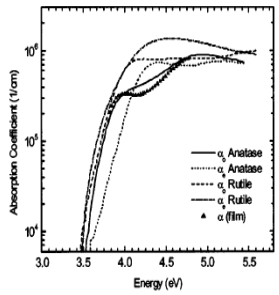

FIG. 5. The optical absorption coefficient for bulk anatase, rutile, and thin-film anatase, determined from the values shown in Fig. 3.

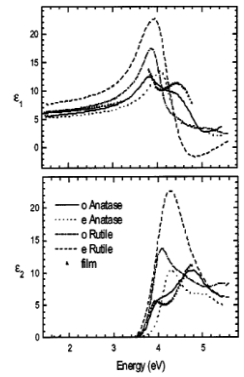

FIG. 4. The complex dielectric function for bulk anatase, rutile, and thin-film anatase, determined from the values shown in Fig. 3.

Figure 4.45 ε_1 and ε_2 for bulk anatase and rutile (from Jellison 2003)

4.18 SE data and comments

Additional insight from a different perspective is provided by SE spectra from 1.5 to 9 eV. To provide a reference for comparison for our extracted dielectric functions, Figs. 4.45 show ε_1 and ε_2 data from Jellison for bulk anatase and rutile as well as a thin film of

anatase. The bottom plot in the figure exhibits no birefringence for energies between1.4.0 and 5.8 eV, and shows the absorption coefficient calculated from these data.

Our dielectric functions $\varepsilon = \varepsilon_1 + i\varepsilon_2$ are extracted through a three-phase model consisting of a c-Si substrate, the overlayer of interest, and the ambient. The overlayer thickness is determined by requiring $\varepsilon_2 = 0$ in the transparent region. The dielectric function was extracted from the VUV data by matching to the bench data in the 4 to 6 eV range. Tables 4.5 and 4.6 list the overlayer thicknesses determined from the bench and VUV ellipsometers, respectively. Discrepancies may be attributed to the refinement of the bench system in providing more precise measurements than the VUV system, both with respect to the ease of measurement in a 1 atmosphere setting as well as its history as a multidecade research instrument.

Table 4.5 3-Phase Extracted Overlayer Thickness (Bench 1.5 - 6 eV)

	6% TiO^2	11% TiO^2	16% TiO^2	24% TiO^2
As-dep	60.0Å	45.5Å	42.0Å	48.0Å
500°C	55.0Å	43.6Å	42.5Å	48.5Å
700°C	56.0Å	39.6Å	37.0Å	49.0Å
900°C	56.0Å	42.0Å	38.0Å	40.5Å

Table 4.6 3-Phase Extracted Overlayer Thickness (VUV 4 – 9 eV)

	6% TiO^2	11% TiO^2	16% TiO^2	24% TiO^2
As-dep	50.5Å	47.0Å	52.0Å	40.0Å
500°C	55.0Å	46.0Å	34.0Å	52.0Å
700°C	68.0Å	39.0Å	40.4Å	34.0Å
900°C	69.0Å	42.0Å	38.0Å	39.0Å

In the following I concentrate specifically on ε_2 because of its energy-local character. The complete set of SE spectra for the 6, 11, 16, and 24% samples as-

deposited and annealed at 500°C, 700°C, and 900 °C are presented in Fig. 4.46. There are three structures we see. First, in comparison to the Jellison data, we attribute the strong feature at ~4.2 eV we see in the annealed spectra (especially the 24% data) as phase segregated 6-fold coordinated titanium. The second is the general manifold we easily see, at 6% TiO_2, at ~5 eV. Because of it general pervasiveness in all our as-deposited samples and its general reduction with respect to the 6-fold phase segregated peak at ~4.2 eV we attribute this manifold to 4-fold coordination. We attribute this to 4-fold Ti silicate coordination. Third, we tentatively describe the edge found at the as-deposited 6% sample at ~3.2 eV as being due to in-solution 6-fold coordinated titanium. It reduction to near removal with annealing belies its possible presence. In general, there is a significant increase in 6-fold phase-segregated,

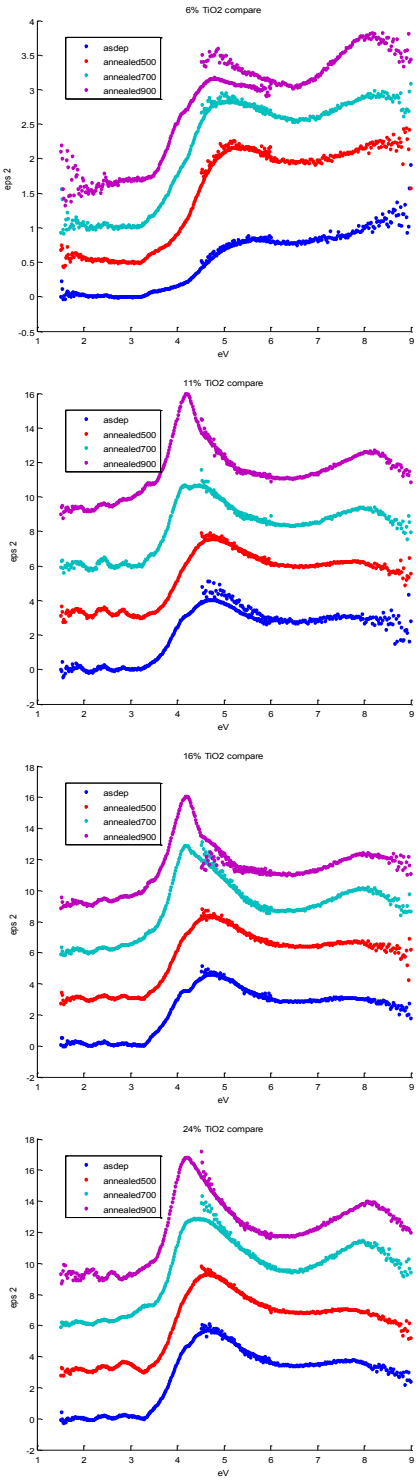

Figure 4.46 SE spectra for the 6%, 11%,16%, and 24% samples as-deposited and annealed at 500 °C 700 °C and 900 °C

coordination between the 500 and 700 ºC annealing temperatures for all compositions.

The complete set of spectra for the samples as-deposited and annealed at 900 °C is presented in Figure. 4.47. All as-deposited-samples show a weak absorption onset at ~3.2eV. For the 11% 16% and 24% Ti 900 °C annealed samples, a significant increase occurs in the peak feature at ~4.2eV. The 900 °C annealed 6% samples show a slight increase in the 6-fold signal about ~4.2 eV with annealing, but the dominant signal we see at ~5 eV in the as-deposited, which we attribute to 4-fold coordination, remains.

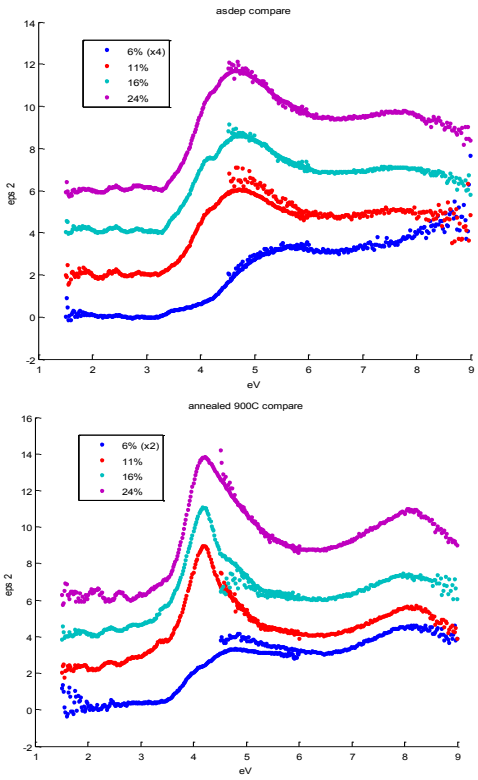

Figure 4.47 SE spectra for the samples as-deposited and annealed at 900 °C

The SE data show strong phase separation between 500 and 700 ºC. As a benchmark, we compare our results to those of Jellison to determine if we are obtaining 6-fold signatures.[9] Some formation of 6-fold coordination occurs in all annealed samples. However, no unambiguous evidence of 6-fold coordination appears in the data for the 6% sample.

4.19 References

1. T. Hoche, M. Grodzicki, F. Heyroth, and P. A. Van Aken, Phys. Rev. B 72 205111, 2005

2. G. S. Henderson, X. Liu, and M. E. Fleet, Phys. Chem. Miner. 29, 32 (2002).

3. R Brydson, L. A. Garvie, A. J. Craven, H. Sauer, F. Hofer, and G. Cressey, 1993 *J. Phys.: Condens. Matter* 5 9379

4. Abbate, M.; Goedkoop, J. B.; de Groot, F. M. F.; Grioni, M.; Fuggle, J. C.; Hofmann, S.; Petersen, H.; Sacchi, M. Surf. Interface Anal. 1992, *18*, 65.

5. Abbas Hodroj, Odette Chaix-Pluchery, Marc Audier, Ulrich Gottlieb, and Jean-Luc Deschanvres J. Mater. Res., Vol. 23, No. 3, Mar 2008

6. A.T. Wen and A.P. Hitchcock CAN. J. CHEM. VOL. 71, 1632, 1993

7. Frank de Groot AND Akio Kotani, *Core Level Spectroscopy of Solids* (CRC Press, Boca Raton FL, 2009).

8. F. M. F. de Groot, J. Electron Spectrosc. Relat. Phenomena 67 (1994) 529.

9. G. E. Jellison, L. A. Boatner, J. D. Bidao. B. S. Jeong, and D. P., Norton, J. Appl. Phys. 93, 9537 (2003)

10. R. Zallen, *The Physics of Amorphous Solids* (Wiley, New York, 1983).

11. S. O. Kucheyev, T. van Buuren, T. F. Baumann, J. H. Satcher, Jr., T. M. Willey, R. W. Meulenberg, T. E. Felter, J. F. Poco, S. A. Gammon, and L. J. Terminell, Phys. Rev. B 69, 245102, 2004!

5. SHALLOW Ga3d CORE-LEVEL TRANSITIONS

5.1 Introduction

We now turn to modeling a series that represents an intermediate case in spectroscopic theory: shallow Ga3d core-level to conduction-state transitions in some Ga III-V compounds. Specifically, we investigate reflectance data of the GaP, GaAs, the GaAsP alloy series, GaSb, and GaSe. These data were obtained in the early 1980's at the Wisconsin storage ring Tantalus 1 by Aspnes and co-workers. The data, many of which were never published, were acquired digitally and stored as separate files. The numerical analyses presented here were done directly from these files, rather than from digitized figures, and hence eliminate one level of inaccuracy. When originally obtained, the GaAsP data, shown in Fig. 5.1, appeared to indicate that the lowest indirect conduction-band minima of GaAs were located at the L symmetry points of the Brillouin zone. Conventional wisdom, based on an assignment made 15 years earlier and commonly accepted as proven, had assigned the lowest indirect conduction band minima to the X symmetry points. The reassignment resolved a longstanding dilemma concerning the operation of devices such as Gunn oscillators, which depend on electron transfer from the lowest minimum at Γ to the first indirect minima. With this revision device performance now

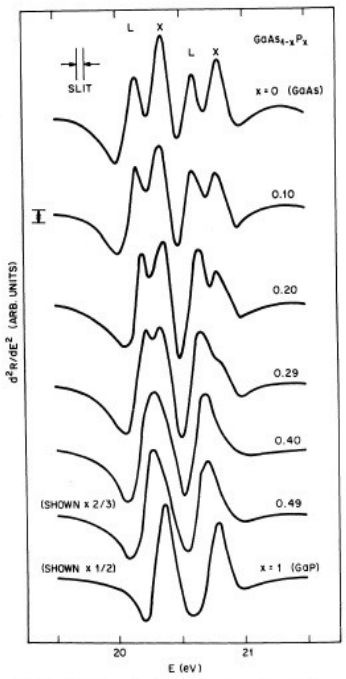

FIG. 1. 2EDR spectra for several samples in the pseudobinary-alloy series $GaAs_{1-x}P_x$. Transitions are identified from the $j = \frac{3}{2}$ and $\frac{1}{2}$ spin-orbit-split Ga 3*d* core levels to *L*-like and *X*-like conduction-band final states. Monochromator slit resolution (full width at half maximum) was 54 meV. Maximum noise is indicated on the second curve.

Figure 5.1 2EDR spectra for several $GaAs_{1-x}P_x$ alloys

agreed with prediction, so the engineers could move on. The issue was considered closed.[1-3]

The simple one-electron band picture appeared to work for the lowest conduction-band minima. However, it failed to describe higher-lying features in the reflectance spectra. This brings up the interesting possibility that the authors, one of whom is the present thesis advisor, could have been right for the wrong reasons. A re-examination appeared to be in order. In any case this is a physically interesting "mixed" situation. One "end point" in the interpretation of optical data concerns visible–near UV SE data on transitions from the highest valence to the lowest conduction band states. These data are conventionally (and well) described by traditional one electron band theory, with minor adjustments necessitated by the Coulomb interaction between the valence-band hole and the excited electron. The other "end point" is represented by deep core level transitions in essentially ionic materials, as discussed in the earlier sections of this thesis. These data are well modeled by multiplet theory. For shallow d-core-level transitions the materials are covalent, but the transitions originate from relatively well localized initial states. Thus it can be expected that neither band nor multiplet theory will be adequate. We investigate the shallow core-level situation from the multiplet perspective, modeling these spectra with a multiplet calculation that focuses on transitions from a closed-shell initial state to an electron-hole final state. The background for these calculations was discussed in Chapter 2 of this thesis. With this approach the important issue is the relative strengths of the individual terms of the Hamiltonian in

the final state. Our results show that the crystal field dominates the apparent splitting of the 3d core hole, in contrast to the accepted picture where the separation is attributed to its spin-orbit splitting.[4] We further examine the effect that the anion and to a lesser extent the symmetry plays on the 4p electron spin-orbit splitting of the Ga final states.

We analyze negative second energy derivatives of the $GaAs_{1-x}P_x$ reflectance data that are similar to those shown in Fig. 5.1. As noted above, these derivatives, from which the data were extracted from the given reference paper, were numerically calculated from the original data.[1] Because multiplet theory depends on the local environment of the initial and final states, analysis must proceed via a two-step process. The first step is to extract the lineshapes associated with each of the five local Ga environments in the $GaAs_{1-x}P_x$ alloys: one where Ga is completely surrounded by As, one where Ga is completely surrounded by P, and the other 3 mixed. While the endpoint situation is clear, to analyze the alloy data we must remove the GaP and GaAs contributions to obtain the spectra characteristic of the intermediate configurations. We do this by first normalizing the second-derivative reflectance spectra with second derivatives of Gaussian functions fitted though a least squares calculation. Doing so provides a normalized functional area to allow for mean square deviation comparisons between fittings. After the spectra are normalized we can then remove the GaP and GaAs contributions using fractions calculated by assuming a stochastic distribution of anions. The resultant spectra are

understood to be representative of the stochastically determined fractional mixtures of the remaining three mixed centers.

The five combinations are then fit by means of a custom multiplet program, which minimizes the mean-square deviation of a set of convoluted Lorentizians with consistent linewidths and amplitudes. Fitting is done by calculating dipole matrix elements with a Hamiltonian that includes 4 terms: the average energy, the spin-orbit splitting parameters of the 3d core hole and the 4p conduction electron, and the radial strength parameters of the cubic crystal field interaction.

We fit our data by least squares analysis that combines a transition rate with a Lorentzian. The explicit function is

$$f = -\frac{\partial^2}{\partial Energy^2}\left((\frac{1}{Energy}) * A1 * \left(\frac{1}{\pi} \frac{2*(DipoleMatrixElement)*\omega}{4*\left(Energy - AvgEnergy\right)^2 + \left(\omega\right)^2} \right) \right)$$

The Lorentzian lineshape is used because it is the most appropriate for individual atomic transitions. One Lorentzian is associated with each allowed transition. It is centered at the appropriate energy and scaled by the appropriate oscillator strength. The overall combination is then scaled together, by the given scaling factor A1, to best-match the data.

The modeling for GaSb uses the same function as that for GaP and GaAs, but we expect a far greater crystal field splitting due to the larger formal valence of the anion and a larger spin orbit splitting term for the electron to match the larger energy separation between features seen in its visible-UV optical spectrum.

The modeling of GaSe represents an interesting critical test of the local crystal field model. As an aside, a literature search revealed no optical data at energies higher than 12 eV for GaSe, so this may be the only shallow-core-level optical data ever taken for GaSe. Although Ga is also fourfold coordinated in GaSe, the Ga environment does not have tetrahedral symmetry. Each Ga has a single Ga-Ga bond and three Ga-Se bonds. The Ga-Se bonds are similar to the Ga-As bonds of GaAs except for the increase and decrease in formal valences of +1 and -1 going from As to Se and As to Ga, respectively.

$$F_2 = \alpha\left[\frac{14}{x^3} - e^{-2x}\left(\frac{14}{x^3} + \frac{28}{x^2} + \frac{28}{x} + \frac{56}{3} + \frac{28x}{3} + \frac{11x^2}{3} + \frac{10x^3}{9} + \frac{2x^4}{9}/\right)\right]$$

$$F_4 = \alpha\left[\frac{315}{x^5} - e^{-2x}\left(\frac{315}{x^5} + \frac{630}{x^4} + \frac{630}{x^3} + \frac{420}{x^2} + \frac{210}{x} + 84 + 28x + 8x^2 + 2x^3 + \frac{2x^4}{5}\right)\right]$$

We thus model GaSe with Ga in trigonal symettry with a separation angle of 118.27 from the +z axis for the three trigonal ligands instead of the 109.47 degrees for a perfect tetrahedral (reference as given below). This breaking of cubic symmetry requires us to include l = 2 spherical harmonics, that is the F_2 radial strength term. To reduce the number of free parameters in the fitting procedure, we set F_2 = 1.88 F_4, where 1.88 is the ratio of the average of the integrated F_2 radial strength term to integrated F_4 radial strength term for Slater-type radial distributions for integer n. The functional forms of F_2 and F_4 are given in Appendix 1 of Bersuker.[4] In addition to the set breaking of the tetrahedral symmetry in GeSe with inclusion of the deviation from the equal angles to those of trigonal symmetry we allow the

difference in the radial strength of the crystal field between the Ga-Ga bond and the three Ga-Se bonds. We fit this as a modification factor (FCFz) of the strength term for the charge site represented by the Ga-Ga ligand. In effect, instead of treating the collective system with a general radial strength term, we associate a strength term with each charge site with the lower 3 sites set equal to each other. We will find that the Ga site generates a distortion opposite to that of Se, a consequence of the different formal valences between Ga and Se.

5.2 General effects of the individual terms in the Hamiltonian

The general description of Ga core-level spectra in the multiplet picture is one of transitions from a closed shell $^1S_0$ state of the Ga ion to a series of $3d^9$- sp^3 states. Although the s and p states hybridize when the crystal field is present, with respect to sp^3 hybridization the s and p states remain distinct in the angular-momentum representation when coupled to the d hole states. Because there are no dipole-allowed d^9s states from the closed shell $^1S_0$ states, the final states essentially have d^9p symmetry.

Covalency minimizes the atomic direct and exchange Coulomb effects for states between the core hole and valence electron states. Inherently, this means that the direct and exchange terms are small relative to a pure atomic, or ionic-type calculation. Therefore, our calculation is essentially one that involves the electron and hole spin-orbit effects on the final states. The cubic crystal field created by tetrahedral bonding only splits the d hole orbitals, so our calculation will only involve the d orbitals of the uncoupled basis set. For GaSe, we will include two crystal field

terms, one for each of the three bottom trigonally symmetric ligands and one for the +z ligand.

Our first objective is to understand how the features in the data depend on the model parameters. Our approach and the terms that we consider important have already been discussed in Sec. 2.8. Briefly, we follow the amount and energy location of p-character in each possible final state, noting that in the dipole approximation the transitions terminate on p levels. In the following, the bottom halves of the figures give these energy locations and strengths. We associate with each transition a Lorentzian lineshape, then construct the final lineshape as a linear superposition of these contributions. The upper halves of the figures give the negative second derivatives of these superpositions.

Figure 5.2 shows the effect of varying the electron s-o splitting from 0.00 to 0.15 eV, assuming a constant cubic crystal field splitting of −0.30 eV and a core-hole s-o splitting of 0.15 eV. The cubic-crystal-field and core-hole values used here are those that give the best overall representation, as will be found in the following. The breaking of the degeneracy of the uppermost transition due to the s-o splitting of the electron is clearly seen. Another point to be made is that the broadening of the features is not a function of the Lorentzian

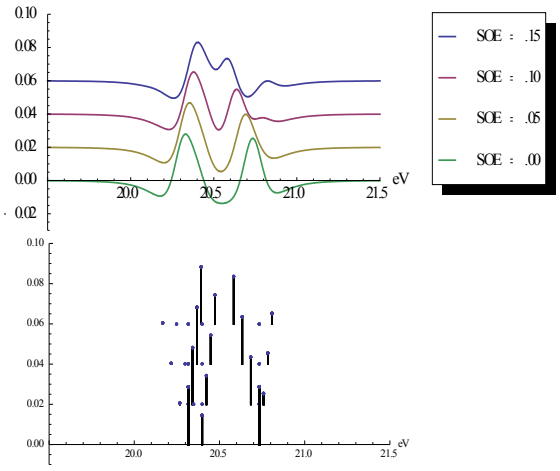

Figure 5.2 Dependences on electron spin-orbit splitting with crystal field splitting

lineshapes alone, but a consequence of the superposition of a number of final states at slightly different energies.

Figure 5.3 shows the dependences on the hole s-o splitting for the same range of relative splitting parameters, assuming a cubic crystal-field splitting of −0.30 eV and an electron s-o splitting of 0.15 eV. We see that a negative crystal field with no hole s-o interaction produces dipole-transition intensities that are completely inconsistent with the data. Therefore, and not surprisingly, a hole s-o splitting term is a necessity for a negative crystal-field parameter.

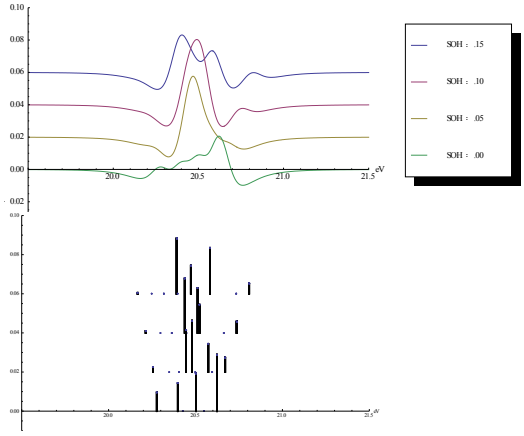

Figure 5.3 Hole Spin Orbit Splitting Series (Crystal Field Splitting)

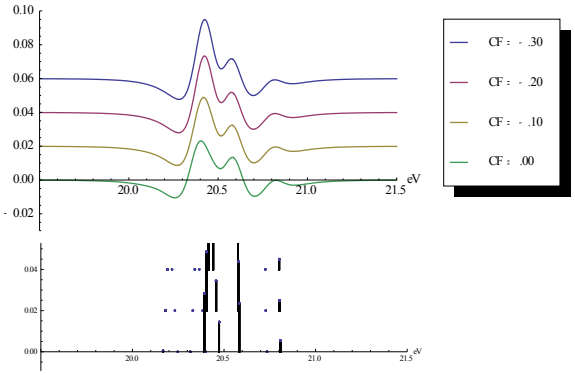

Figure 5.4 Crystal Field Splitting Series

Figure 5.4 shows the effect of varying the crystal-field splitting parameter from 0.00 to −0.30 eV with electron and hole s-o splittings held constant at 0.15 eV. A change in a negative crystal-field splitting for a relatively large hole s-o splitting is inconsequential.

The primary result derived from this section is that crystal-field effects mimic the hole spin-orbit interactions if crystal field splitting are comparable to the, in isolated atomic spin-orbit splitting. In addition, the spin-orbit splitting of the electron

is necessary to describe split structures which are evident in several of Ga semiconductor systems such as GaP and GaAs.

5.3 Removing the contributions of the GaP and GaAs centers in $GaAs_{1-x}P_x$ alloys

Because multiplet theory requires spectra to be interpreted in terms of localized interactions, we must extract the spectral properties of each of the five Ga configurations, as mentioned above. Assuming that the anions are distributed randomly, for a given composition x these can be calculated stochastically as $P(X=k) = (n\ k)p^k(1-p)^{n-k}$. We take x to be the fraction of P sites. Thus with tetrahedral bonding the probability of a Ga atom being surrounded by 4 P atoms is x^4, that for the first "trigonal" site with 3 P atoms and 1 As atom is $4x^3(1-x)$, that for the "tetragonal" site with 2 P and 2 As atoms is $6x^2(1-x)^2$, that for the second "trigonal" site with 1 P and 3 As atoms is $4x(1-x)^3$, and finally that for the second tetrahedrally symmetric site with 4 As is $(1-x)^4$.

Figure 5.5 shows the statistical weighting for the different $GaAs_{1-x}P_x$ alloy centers. For $GaAs_{.90}P_{.10}$, $GaAs_{.80}P_{.20}$, and $GaAs_{.71}P_{.29}$, the dominant contributions

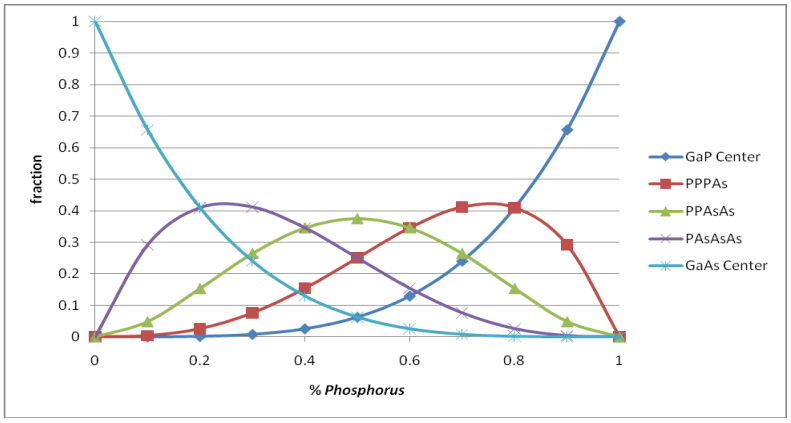

Figure 5.5 Statistical weighting for the different $GaAs_{1-x}P_x$ alloy centers

come from the trigonal PAsAsAs and the tetrahedral $GaAs_4$ center. For $GaAs_{.60}P_{.40}$ and $GaAs_{.51}P_{.49}$ the contributions are rather thoroughly mixed. In particular, there is a substantial increase in the influence of the trigonal PPPAs center as we go from 10% to 49% P.

To isolate the contributions of the various centers, we first normalize the data. The plots below illustrate the results of nonlinear least-squares fitting the data to the negative second derivatives of Gaussians. Two Gaussians are used for GaP, four for GaAs, $GaAs_{.90}P_{.10}$, $GaAs_{.80}P_{.20}$, and $GaAs_{.71}P_{.29}$, and three for $GaAs_{.60}P_{.40}$ and $GaAs_{.51}P_{.49}$. Given the multicomponent nature of the transitions, as indicated in Figs. 5.2 to 5.4, this is an approximation, but as the fits below show, the approximation is acceptable. Fitting parameters of the individual Gaussians to the data sets are the critical energies, amplitudes, and widths. Because second derivatives depend on lineshapes, and in particular on the widths of the features, we cannot achieve normalization simply by equating maxima. Rather, we normalize by requiring the area under the Gaussians used in the fitting to be equal to 1. The results for each data set are given in Figs. 5.6 to 5.12. The fits are shown on the left, and the superpositions of the contributing Gaussians are shown on the right. The fits are all very good allowing for reasonable normalization and comparisons between data sets. As a side note, the broadness of the spectra belies the usefulness of direct derivative methods such as electroreflectance to obtain the critical-point features.

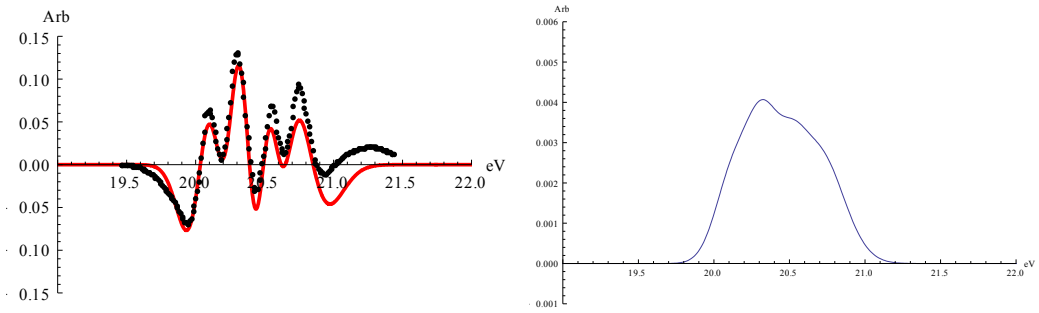

Figure 5.6 Normalized GaAs second-derivative reflectance spectrum

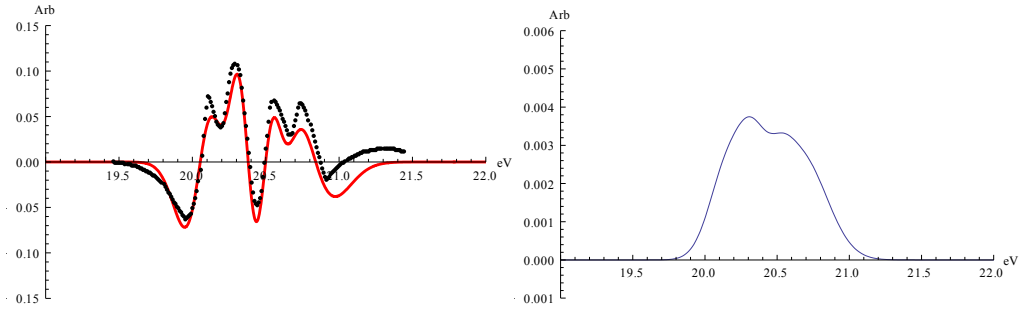

Figure 5.7 Normalized $GaAs_{.90}P_{.10}$ second-derivative reflectance spectrum

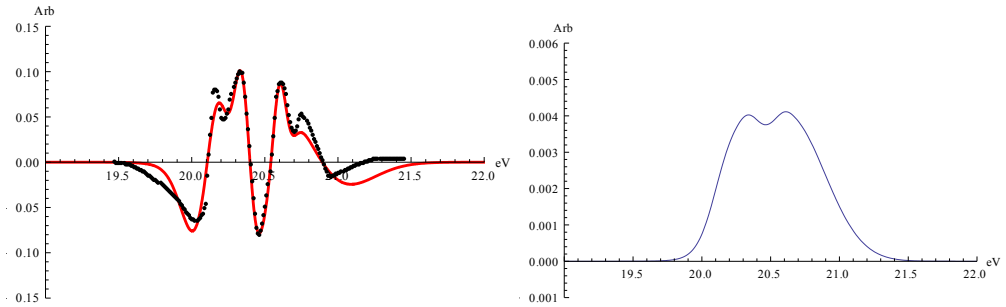

Figure 5.8 Normalized $GaAs_{.80}P_{.20}$ second-derivative reflectance spectrum

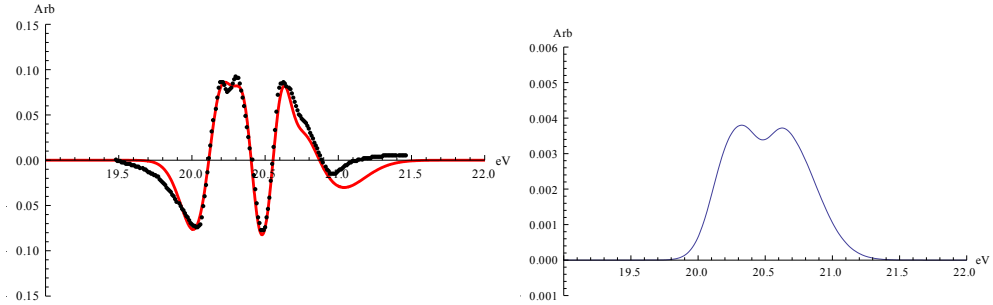

Figure 5.9 Normalized $GaAs_{.71}P_{.29}$ second-derivative reflectance spectrum

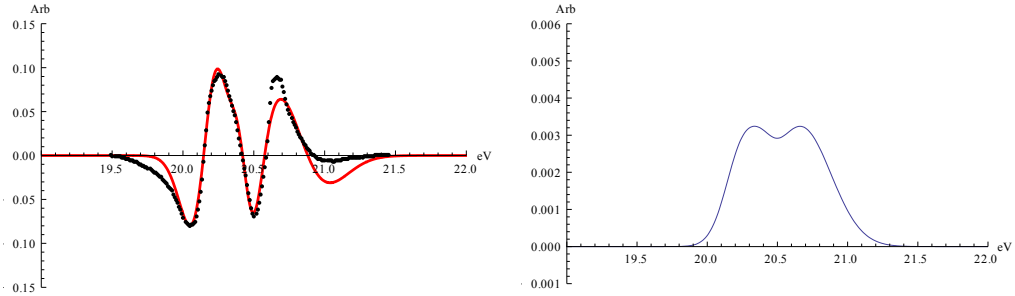

Figure 5.10 Normalized $GaAs_{.60}P_{.40}$ second-derivative reflectance spectrum

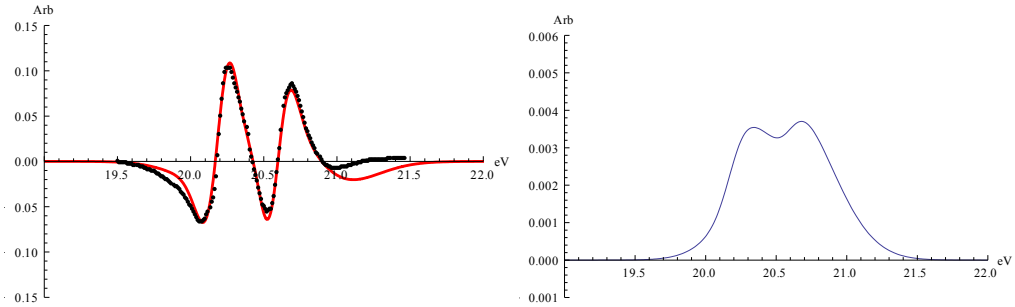

Figure 5.11 Normalized $GaAs_{.51}P_{.49}$ second-derivative reflectance spectrum

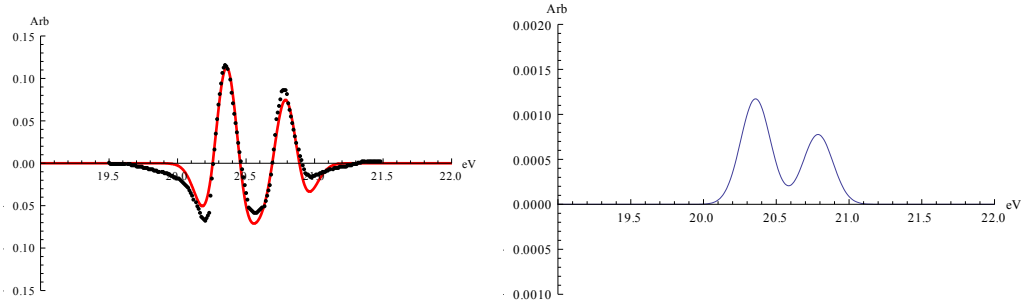

Figure 5.12 Normalized GaP second-derivative reflectance spectrum

5.4 Results

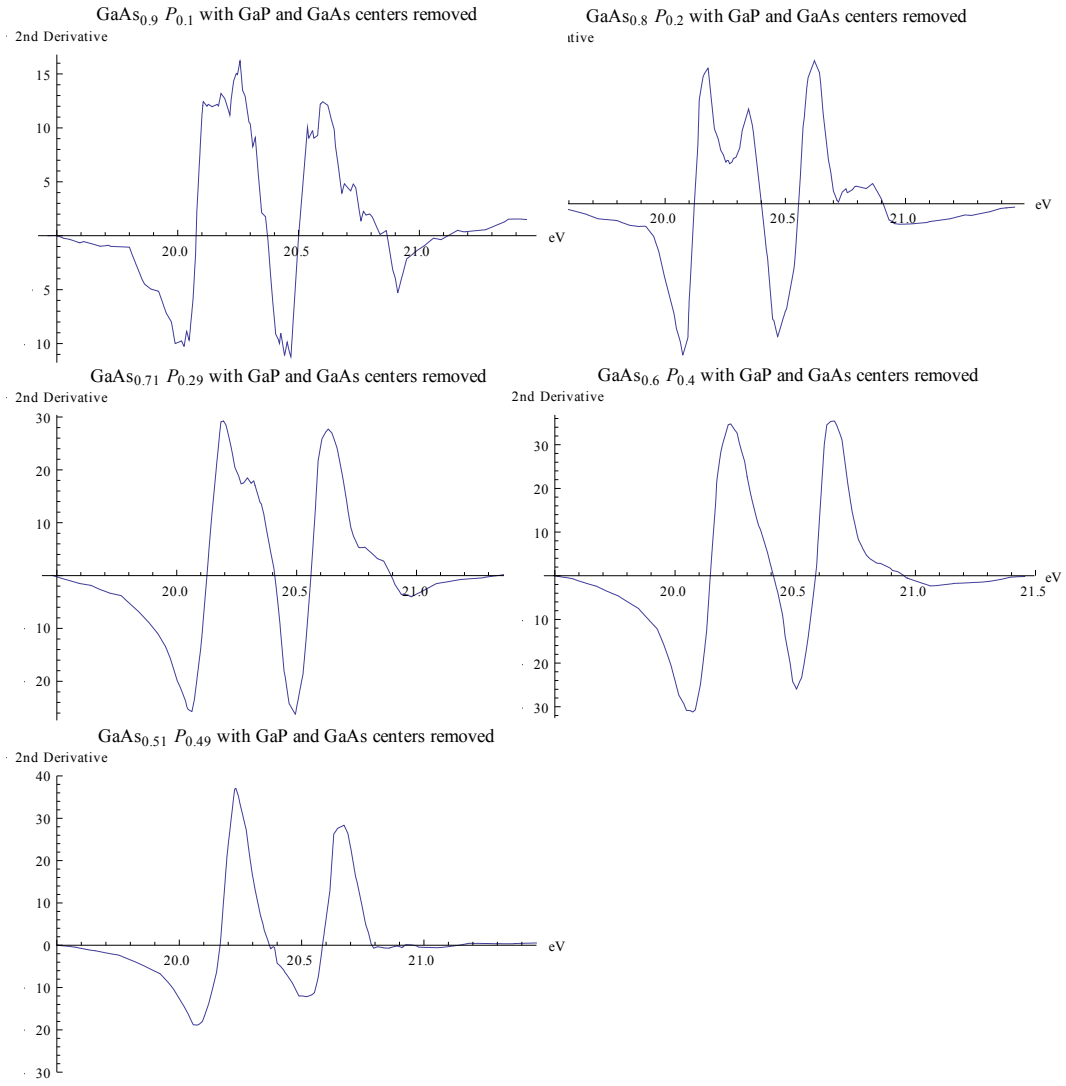

Figure 5.13 $GaAs_{1-x}P_x$ spectra after the GaP and GaAs contributions have been removed

Figure 5.13a-e show the alloy spectra after the GaP and GaAs contributions have been removed. According to our model, these represent the combined contributions of different fractional mixtures of the remaining three centers. As such, they are ready for further analysis, specifically for the extraction of crystal-field effects and spin-orbit splittings.

Figures 5.14 to 5.22 show the result of fitting the negative second derivative of the our model transition function with the second derivative of the negative reflectance for GaP in the energy range around 20.5 eV. The summed dipole coefficients are included, with arbitrary absolute amplitudes to assess the relative strengths of the transitions and their energies as predicted by theory.

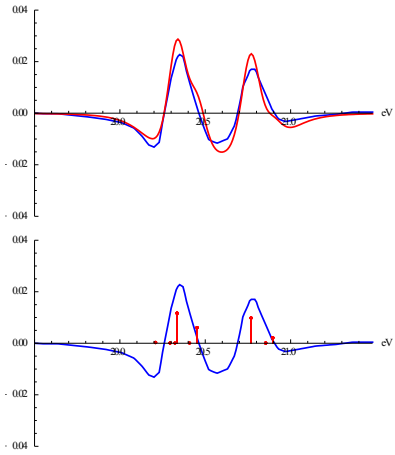

Figure 5.14 GaP fitting

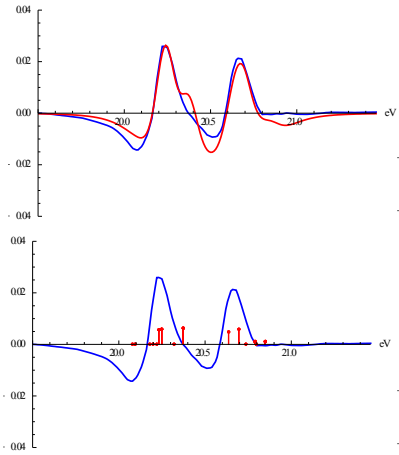

Figure 5.15 $GaAs_{.51}P_{.49}$ fitting

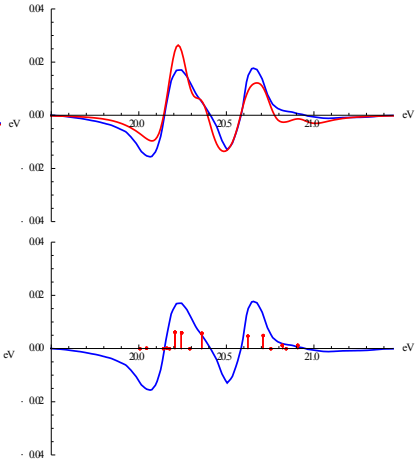

Figure 5.16 $GaAs_{.60}P_{.40}$ fitting

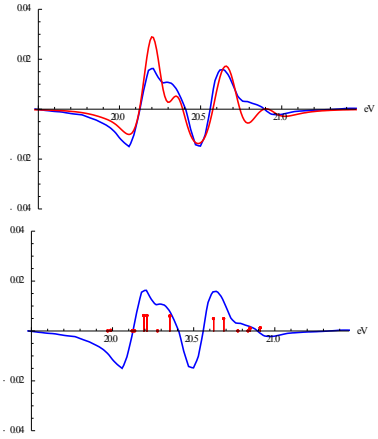

Figure 5.17 $GaAs_{.71}P_{.29}$ fitting

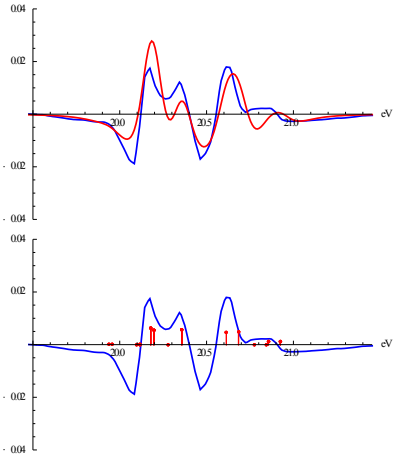

Figure 5.18 $GaAs_{.80}P_{.20}$ fitting

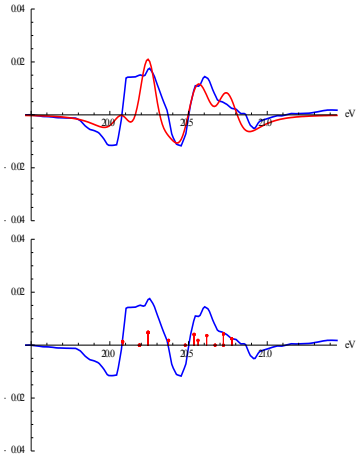

Figure 5.19 $GaAs_{.90}P_{.10}$ fitting

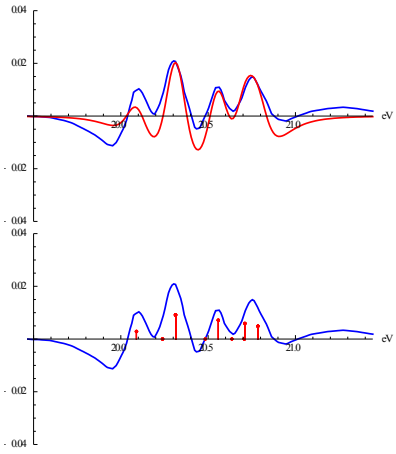

Figure 5.20 GaAs fitting

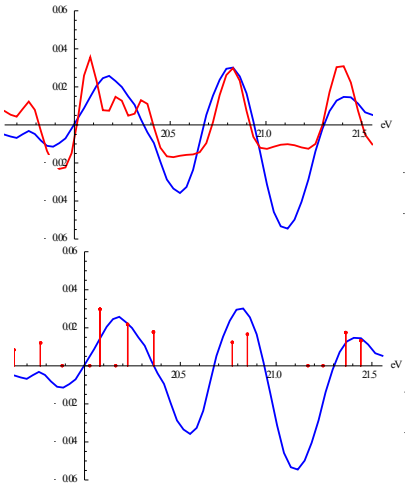

Figure 5.21 GaSe fitting

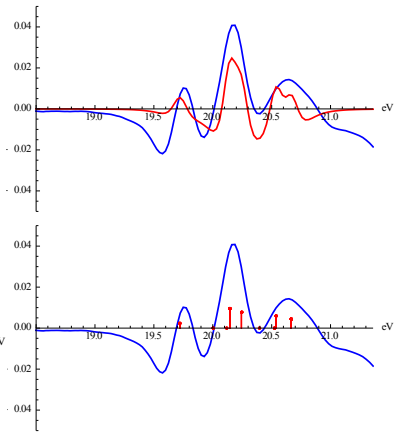

Figure 5.22 GaSb fitting

Table 5.1 Ga Compound Fitting Summary Part 1

	FCFz	error	CFMajor	error	AvgE	error
GaP	0.229874	0.015855	0.229874	0.0159	20.5398	0.0042
GaAs	0.585828	0.021871	0.585828	0.0219	20.5064	0.0039
GaSe	0.14227	0.225789	1.41635	0.192227	20.4969	0.021657
GaSb	0.609528	0.150289	0.609528	0.150289	20.2908	0.018754
fractionP						
1	0.229874	0.015855	0.229874	0.0159	20.5398	0.0042
0.49	0.124646	0.121445	0.287942	0.0119	20.4471	0.0047
0.4	0.037373	0.032355	0.285652	0.0272	20.4411	0.0095
0.29	0.152081	0.116033	0.324238	0.0306	20.4287	0.0104
0.2	0.177769	0.087286	0.366793	0.044	20.4222	0.0085
0.1	0.334066	0.139727	0.64087	0.0417	20.4497	0.0443
0	0.585828	0.021871	0.585828	0.0219	20.5064	0.0039

Table 5.2 Ga Compound Fitting Summary Part 2

	SOE	error	SOH	error	msd	A1	w1
GaP	0.08494	0.0265	0.199888	0.0202	0.001209	0.003	0.3
GaAs	0.150094	0.0078	0.044656	0.0065	0.004536	0.003	0.3
GaSe	0.393752	0.026664	0.168465	0.060671	0.014654	0.009	0.3
GaSb	0.281124	0.079034	0.074274	0.033106	0.010046	0.003	0.3
fractionP							
1	0.08494	0.0265	0.199888	0.0202	0.001209	0.003	0.3
0.49	0.102098	0.0523	0.202726	0.0362	0.001431	0.003	0.3
0.4	0.132254	0.0657	0.227833	0.0499	0.001859	0.003	0.3
0.29	0.14982	0.0893	0.238586	0.0628	0.002515	0.003	0.3
0.2	0.160786	0.084	0.243527	0.0472	0.003757	0.003	0.3
0.1	0.107507	0.0241	0.052476	0.0226	0.004391	0.003	0.3
0	0.150094	0.0078	0.044656	0.0065	0.004536	0.003	0.3

5.5 Discussion

The crystal field term is determined by the charge distribution surrounding the core. The crystal-field splitting of a d electron in a negative charge field is the same as that of a d hole in a positive charge field. The effect will be reduced in a covalent material because the negative electronic charge in the bonds will offset the adjacent positive atomic cores. For GaAs and GaP the crystal-field effects due to the four ligand charges are equal, but for the $GaPAs_3$, GaP_3As, and GaSe configurations there will be a crystal-field disparity between one of the ligands and the other three. For these fittings, the tetragonal distortions found in GaP_2As_2 are implicitly not included. Even an equal mix of GaAs and GaP maintains a majority fraction of trigonally distorted centers, so the tetragonal distortion can be thought of as a perturbation.

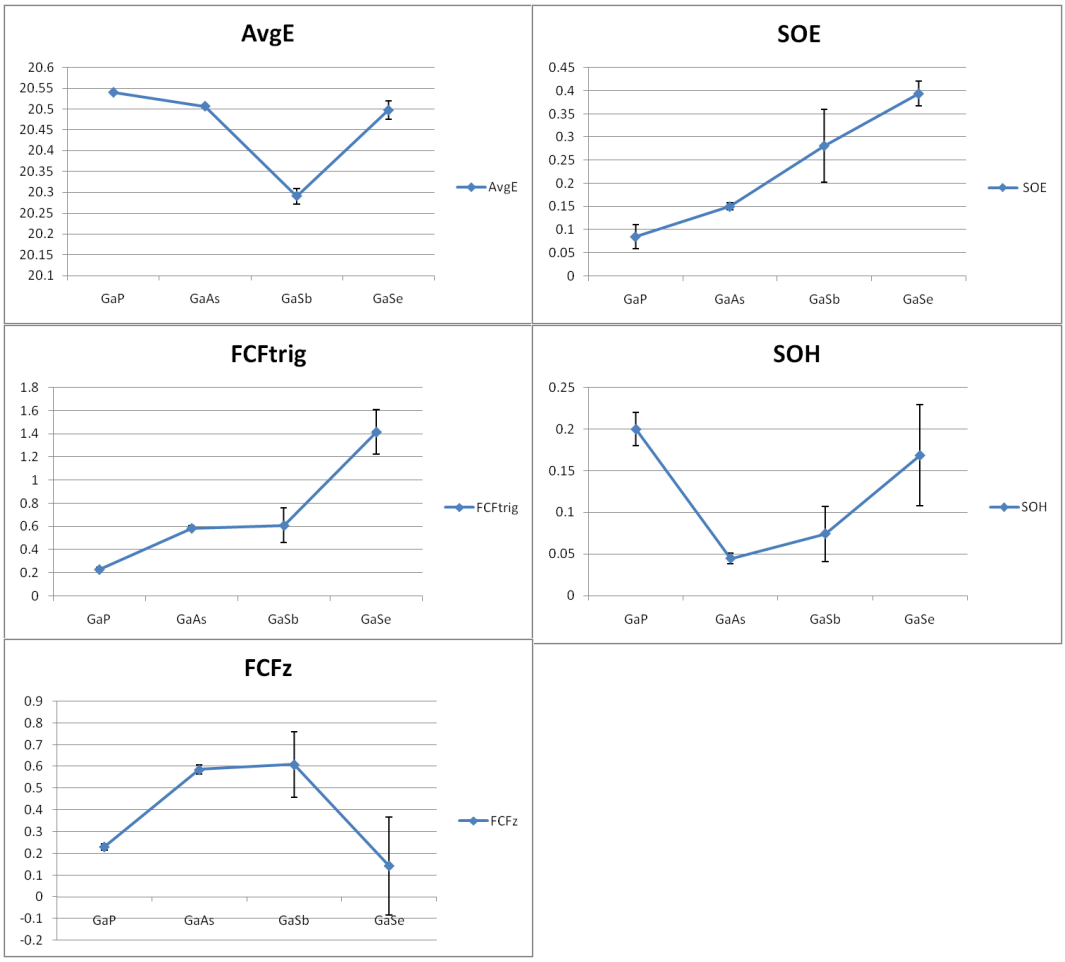

Figure 5.23 GaP GaAs GaSe GaSb comparison

The variation of the average-energy term is approximately consistent between GaAs and GaP but shows a reduction in overall average energy of transition in the alloy series. These values are still well above the average energy of transition found for GaSb. This is surprising but maybe attributed to effects due to the non-tetrahedral symmetry of these centers.

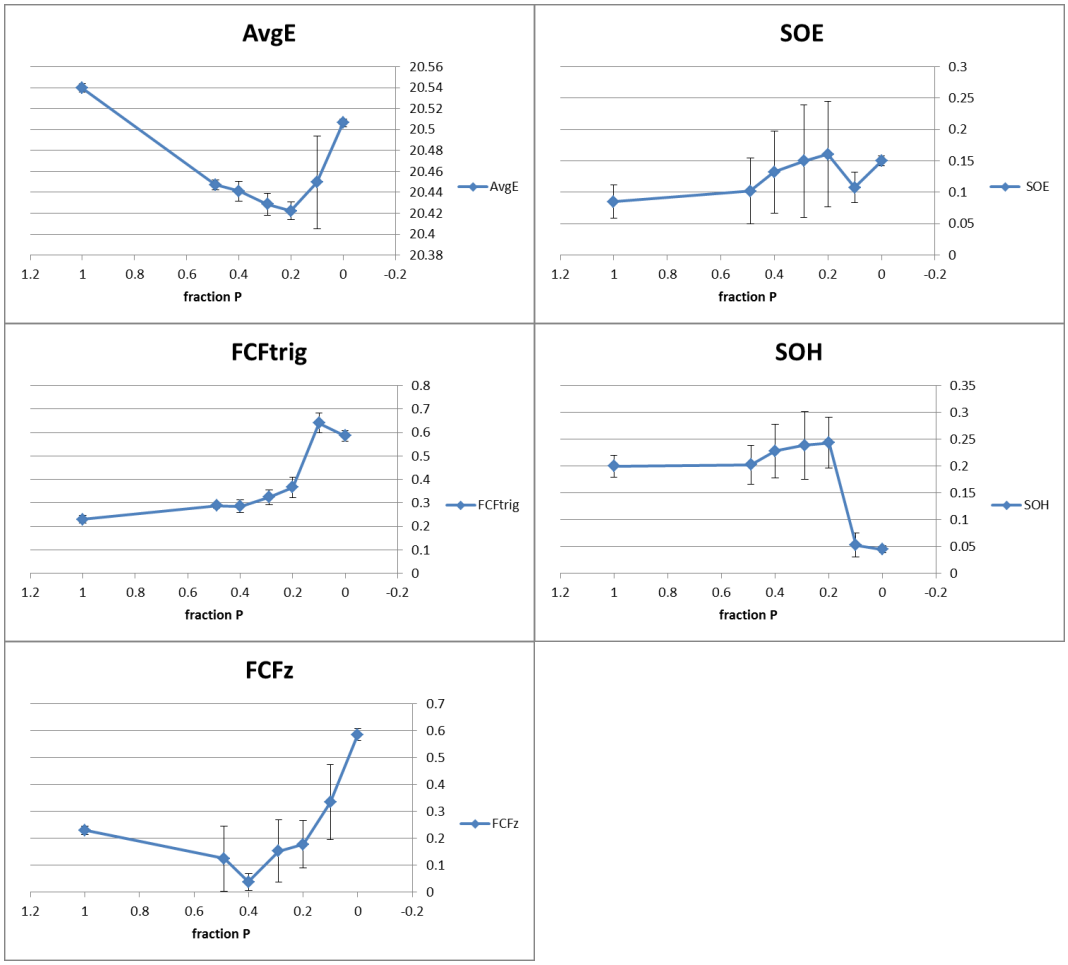

Figure 5.24 $GaAs_{x-1}P_x$ alloy series comparison

Within the multiplet model, the spin-orbit splitting obtained for the electron in the conducting state is found to be larger in GaAs than GaP by a factor of about 2 and then goes up nearly another factor of 2 between GaAs and GaSb. In The GaAsP alloy series, the "flat banding" at about 50% P is particularly interesting. Although it is not possible to be certain that this result is characteristic of P concentrations between x = 0.5 and x = 1, the original author confirms that the "doublet" like nature of the features persisted for larger values of x, indicating that the splitting should be at most no larger than indicated, and possibly less. Taking a

two-band model through a band theory type calculation shows that the peak structures do not flat band, but instead, maintain an anticrossing behavior (although the data for higher concentration GaAs alloys never shows this.)[1]. This range where the spin-orbit splitting is constant is interesting, because it indicates that the $GaAs_2P_2$ and the $GaAsP_3$ configurations are probably more like GaP in their bonding and antibonding character.

With respect to the crystal field the "trigonal" components maintain a reasonable trend from nominal GaP to GaAs. Going from the maximum GaAs to the GaP (backwards on the graph) there is a relatively abrupt transition to a GaP-type crystal-field interaction. This is expected because the dominant trigonal center is AsAsAsP.

We see a general decrease in the spin orbit splitting of the hole from GaP to GaAs and GaSb. We make some comments on the origin of the primary and secondary splittings of the structures, specifically the apparent doublet (actually a doublet of doublets) for GaP and the obvious doublet of doublets for GaAs. It has always been assumed that the dominant ~ 0.5 eV splitting in these spectra was due to the s-o splitting of the 3d electrons, described in this study as the splitting of the core hole, and typified as the $3d^9$ part of the final state. However, the fittings clearly show that the assumption of a constant spin-orbit splitting of the core hole throughout the $GaAs_{1-x}P_x$ system is not valid. Thus the authors of the 1980 work may well have been right for the wrong reasons.

The analysis of GaSb shows a continuation of the trends found with GaP and GaAs. It is interesting that GaSb exhibits a crystal-field splitting that is similar to that of GaAs but that the average energy is significantly reduced. The complicated interaction between the bonding-electron distribution and overall bond length can possibly provide an explanation for this relatively unexpected result. The consistency between the hole spin-orbit splitting and the crystal-field effect for GaSb shows that the modeling is reasonable. The crystal-field splitting and hole spin-orbit splitting is consistent between GaAs and GaSb even though the electronegativities of As and Sb are different. This means that some other term must compensate. The modeling results indicate that this compensation comes via the average energy of the transition, which is a measure of the overall effective binding energy about the Ga ion.

Finally, we consider the fitting of the GaSe data. There is a dramatic increase in the crystal-field terms for the Ga-Se bonds but a decrease to near zero for the Ga-Ga bonds. These values are consistent with the increase in formal valence for Se and the near-neutral nature of the Ga-Ga bond.

This work has been extremely useful in characterizing the shallow d-core transitions of the Ga semiconductor systems. A deeper understanding of the nature of the primary splitting, with respect to the anion-created ligand field, is obtained by focusing on the interplay between the crystal-field effect and the spin-orbit effect of the hole. Interplay between the d-orbital crystal field and the 3d spin-orbit effect has also been noted by Shirley and co-workers.[6]

The crystal-field terms found here achieve their strength from the positive anions. For a nominal Slater-type 3d orbital this is impossible because the radial distribution does not extend far enough to interact with the anion core. However, the Ga 3d orbitals relevant here are those of the 3d hole, which is repelled by the effectively average positive charge about the cation.

In addition to crystal-field effects, the extended radial distribution of the 3d core hole also acts to reduce spin-orbit splitting effect, as the hole wavefunction can interact with the charge distribution of the bonding electrons, specifically with the charge gradient opposite to that of the core hole. The Ga environment becomes more electropositive through the sequence P to As to Sb. This trend causes a corresponding increased localization of the 3d hole, effectively increasing the p-electron density about the Ga core and hence increasing the spin-orbit splitting of the electron, as seen in the data. It would appear that this should affect the distribution of the d holes in a similar manner. However electropositivity is a measure of electron removal in a chemical setting. Once the bonding charge distribution is in balance, the d-hole crystal field is probably dependent on a host of complex interactions which, on net, affects the crystal-field and spin-orbit splittings of the hole as indicated through the fittings. With respect to the spin-orbit and crystal-field interactions of the d hole, though it slightly begs the question due to both terms both presenting splitting interactions. It is interesting and understandable that the fittings for GaP GaAs and GaSb show opposite radial strength interactions for the two terms. This makes sense as the anions increase electropositivity as we proceed

from P to As to Sb. There will thus be an increase in the crystal-field term, but this will push bonding electrons towards the cation disrupting the d-hole spin-orbit interaction by providing a larger set of negative gradients to counteract the gradient due to the core hole. Interestingly, there is an increase in bond length from the GaP to GaAs to GaSb which explains the possibility for a simultaneous lack change in effects from GaAs to GaSb.

The present approach may be useful for explaining shallow d-core level spectra of other semiconductors, for example those containing In.

5.6 References

1. S. M. Kelso, D. E. Aspnes, C. G. Olson, D. W. Lynch, and D. Finn, Phys. Rev. Lett. 45, 1032 (1980)

2. D. E. Aspnes, and C. G. Olson, Phys. Rev. Lett. 33, 1605 (1974)

3. D. E. Aspnes, C. G. Olson and D. W. Lynch, Phys. Rev. B 12, 2527 (1975)

4. I. B. Bersuker, *Electronic Structure and Properties of Transition Metal Compounds* (John Wily & Sons, Inc., 1996).

6. Khu N A, Chevy A and Chevalier J 1975 *Phys. Stat. Solidi* (a) **31** 469

6. L. Ley, S.P. Kowalczyk, F. R. McFeely, and D. A. Shirley, Phys. Rev. B 10, 4881 (1974)

6. SUMMARY AND FUTURE WORK

6.1 Summary

In this work we investigated local atomic affects on the cations of Ti silicate alloys and Ga-containing semiconductors as well as using spectroscopic ellipsometry to provide secondary verification and elucidate effects on the Ti silicate system. Investigation of the core-level spectra of Ti silicate alloys involved analyzing and interpreting data acquired by X-ray photoemission spectroscopy (XPS) of Ti $L_{2,3}$, O K_1, and Si $L_{2,3}$ transitions, X-ray absorption spectroscopy (XAS) of Ti $L_{2,3}$ and O K_1 transitions, and spectroscopic ellipsometry (SE) on O 2p to conduction-state transitions.

Definitive verification of 4-fold coordination in the Ti silicate alloys was obtained by combining results from analyzing Ti $L_{2,3}$ XAS data with those from XAS O K_1, Ti $L_{2,3}$, and SE data. The analysis showed for the first time that it is possible to distinguish two separate 4-fold coordination centers, on that maintains tetrahedral symmetry and one that is trigonally distorted. It is also possible to distinguish sixfold rutile-and anatase-like structures, that is, XAS signals in thin film material that is consistent with octahedral XAS signals from rutile and anatase over the full composition and annealing range. Sixfold-coordinated “in-solution” Ti was postulated at low Ti concentration ranges. The comparison of O K_1 and Ti L_3 data of samples with low Ti concentrations verified the presence of the separate symmetry sites of four fold coordination in both as-deposited and annealed material. Further distinct coordination separations occurred upon annealing at 900ºC, as also shown

by analysis of O K_1 XAS spectra. The SE data demonstrate that this separation occurs between 500 and 700 ºC. The O K_1 data and the plateau in the Ti $L_{2,3}$ data indicate near-complete sixfold coordination in samples with Ti concentrations of 36% or greater. Comparison with previous studies shows that this near-complete sixfold conversion can be explained by the segregation of the Ti phase into striations, which from the absence of any SiO_2 signal suggests the formation of a laminar capping layer.

The atomic-like nature of the Ti $L_{2,3}$ spectra was verified by interpreting multiplet structures, and demonstrated theoretically that the $2p^5 3d^1$ final states of the Ti $L_{2,3}$ spectra do not maintain any significant degeneracy even in the absence of a crystal field. The degeneracy is broken by the direct and exchange Coulomb interactions, as demonstrated in the calculations of LS coupling. The 2p spin-orbit interaction provides additional splitting before the crystal field is introduced. Significant mixing, which allows breaking of the dipole selection rule, occurs when crystal-field effects are added. The states still exist in the absence of a crystal field, but they are “pure” states with no mixing and therefore are generally dipole-forbidden.

Simple combinations of endpoint spectra were used to obtain coordination concentrations, and then a stochastic model was applied to the results. The primary conclusion is any 4-fold sites with Ti-O-Ti bridging O bonds have a strong tendency to drive to Ti 6-fold coordination. This is a purely probabilistic result that does not take specific bonding sites into consideration. SE studies of the Ti silicates provide

dielectric functions for a set of alloy compositions and annealing temperatures. In addition, these data verified that significant changes occurred between the annealing temperatures of 500 and 700º C.

To investigate the applicability of a multiplet description for shallow core levels, we investigated reflectance spectra containing structure associated with Ga3d shallow core levels, which occurs near 20 eV. Data were studied for GaP, GaAs, GaSb, GaSe and the alloy series GaAsP. With the Ga semiconductor materials the atomic-multiplet calculations are a very good first start in determining eigenvalues and dipole-allowed transition matrix elements of the shallow core level transitions. Reasonable representations of the structures observed in the negative second derivative of the reflectance spectra were obtained by including in the calculations crystal-field splitting and the spin-orbit interactions of the 3d core hole and the 4p excited electron. A crystal-field model was required, with contributions from both the bonding electrons as well as the positive anion cores.

6.2 Future Work

Despite the progress made here, work still needs to be done on Ti silicates. Obvious remaining questions include determining more precisely the annealing temperature as a function of alloy composition for phase segregation in the low Ti composition range. With respect to multiplet calculations, further work is necessary to determine the impact on the lineshapes of a non-cubic crystal field on the p-orbital-hole part of the p^5d^1 final states.

With respect to the shallow core levels, the types of calculations done here for the Ga-containing semiconductors may be useful in explaining the shallow d-core level spectra other materials, for example In-containing semiconductors. Implicit in the present approach is the idea that some critical-point transitions can be interpreted as transitions between “localized” atomic-like states. This means that angular momentum is the significant variable. It should be noted that the final states in these transitions all lie in the continuum of the electronic structure of these materials, and hence are more properly considered as resonances. Further work needs to take the associated complications into account. This means that the overall goal of finding the correct understanding of how multiplet and band theory relate must continue to be pursued.